A search for Lepton Flavour Number Violation in Z^0 decays using the DELPHI detector at LEP

Cand. Scient. Thesis in Experimental Particle Physics

Jørgen Hansen

Department of Physics
University of Oslo
Norway

June 18, 1996

Abstract

A search for the three lepton flavour number violating decays of the Z^0, $Z^0 \rightarrow \mu\tau$, $Z^0 \rightarrow e\tau$, and $Z^0 \rightarrow e\mu$, using the DELPHI detector at LEP with the data from LEP runs 1991–1994, is described. No signal was found, and 95% CL upper limits on the branching fractions were determined to 0.85×10^{-5}, 1.7×10^{-5}, and 0.25×10^{-5}, respectively.

Acknowledgements

I would like to thank first of all my supervisor, Lars Bugge, for his support and hard co-work on the analyses which is described in this thesis, and for providing inspiration and enthusiasm throughout the period in which the work was done. Thanks also go to Bjarne Stugu, University of Bergen, for his help in getting me started at the central UNIX computer cluster at CERN, and to Trond Myklebust, for always helping out with local computer problems. I would also like to mention my fellow students here at the EPF group in Oslo; Ole Røhne, Sindre Rødseth Hansen, Esben Lund, Vidar Lund, Bernt Olav Rostad, Håkon Sundsvold Fløystad, Anne-Kari Ytrestøl, Harald Meland, and Yngve Kvinnsland (whith whom I have shared an office for the last 5 months without having driven him insane, an admirable feat on his part) for providing interesting discussions and a lively and inspirational atmosphere in the group.

Contents

List of Figures

List of Tables

Chapter 1

Introduction

The Standard Model (SM) describes all our known physical processes, and predicts numerical quantities which are in agreement with all experimentally obtained results, even though this can be questioned in a few rare cases, most notably for the branching ratio of the Z^0 into the two quark pairs $b\overline{b}$ and $c\overline{c}$, where the experimental results are a few standard deviations away from the prediction from SM. Even so, there is a general feeling within the scientific community that SM is not the final theory; this is motivated by, among other things, the large number of free parameters in SM (approximately 20), and the lack of connection between the electrical charges of the quark sector and the lepton sector, even though the quarks all have integer multiples of *exactly* 1/3 of the charge of the charged leptons (electron, muon and tau lepton), within extremely small experimental errors. Several extensions to SM, some of which will be treated in chapter 2, have been proposed, which, in many cases, predict new phenomena and physical processes not allowed by SM. The search for these new processes is a naturally important task for physicists in high energy physics, as the discovery, or absence, of such processes might point out feasible directions for the extensions of SM.

An example of such a process is the lepton flavour number violating (LFV) decays of the Z^0, that is the three decays

$$Z^0 \rightarrow \mu^\pm + \tau^\mp \qquad Z^0 \rightarrow e^\pm + \tau^\mp \qquad \text{and} \qquad Z^0 \rightarrow e^\pm + \mu^\mp$$

which can be summarized as

$$Z^0 \rightarrow l_i \overline{l_j}, i \neq j$$

where the subscripts i and j denote an electron, a muon or a tau lepton ($i, j = e, \mu$ or τ, which is a notation that will be sustained throughout the paper). These decay processes have several features which make them attractive for study:

1. They are absolutely forbidden by SM to all orders of coupling constants, so that any trace of such decays will be a clear sign of new physics outside of SM.

2. The topologies are simple, with only two particles resulting from the processes, where in two out of the three LFV decays, the decays contains a stable particle, the electron. (As will be explained in section 4.1, the muon can also be regarded as stable with respect to detection in the DELPHI detector, making the situation even nicer).

3. Since the decay processes are leptonic, and not hadronic, they are favourable from an experimentalist's point of view, since, at LEP energies, the detection of leptons is

an easier task than detection of hadrons, given that hadronic events will shower into many particles.

In this thesis, a search for the three LFV decay channels of the Z^0 is presented. The search has been performed with the DELPHI detector at LEP (Large Electron Positron collider), situated at CERN, the European Laboratory for Particle Physics (The acronym CERN comes from the earlier French title: "Conseil Europeen pour la Recherche Nucleaire"). Data from the 1991–1994 LEP runs have been used, and no signal was found in any channels. Upper limits on the branching ratios of the three LFV decays, $Z^0 \to \mu\tau$, $Z^0 \to e\tau$, and $Z^0 \to e\mu$, were set at 0.85×10^{-5}, 1.7×10^{-5}, and 0.25×10^{-5}, respectively.

Chapter 2

Theoretical motivation

The Standard Model [1] builds the world from particles that can essentially be divided into two main classes: the gauge bosons, which are the spin-1 particles that propagate forces between particles, and the spin-$\frac{1}{2}$ fermions, which build matter. These fermions can again be divided into two new main classes, which are the quarks and the leptons, with their corresponding antiparticles, the anti-quarks and the anti-leptons. The quarks and leptons are grouped into 3 generations, where the first generation consists of the u quark, the d quark, the electron and the electron neutrino (together with their antiparticles). These particles are the ones that build all the matter that one encounters in the normal, physical world, together with the γ, the gauge boson for the electromagnetic force (and the graviton, G, which propagates the gravitational forces, but is so weakly interacting that it has yet to be detected). Some of the properties of the 3 generations of quarks and leptons are listed in table 2.1, where the values of the 3 Lepton Flavour Numbers are listed in the last 3 columns.

In the Minimal Standard Model (MSM), there is an absolute requirement that all reactions conserve all 3 Lepton Flavour Numbers individually. In this model, one assumes that all 3 neutrinos, and of course their corresponding anti-neutrinos, have zero rest mass, such that mixing between the weak eigenstates and the mass eigenstates cannot occur, as will be explained later. This is in sharp contrast to the quark sector, where the weak eigenstates of the quarks are *not* equal to the mass eigenstates, such that transitions between generations can occur in weak decays; this is what is known as flavour changing charged currents. Thus, if one assigns a specific "Quark Flavour Number" to the quarks of each generation, similar to the Lepton Flavour Number (see table 2.1), this would not be conserved in weak interactions.

The mixing between different generations of quarks is generated by the famous Cabbibo-Kobayashi-Maskawa (CKM) matrix [1, page 286], and is generally written, before any parametrization of the specific mixings is introduced, as:

$$\begin{pmatrix} d' \\ s' \\ b' \end{pmatrix} = U \begin{pmatrix} d \\ s \\ b \end{pmatrix} \Rightarrow \begin{pmatrix} d' \\ s' \\ b' \end{pmatrix} = \begin{bmatrix} U_{ud} & U_{us} & U_{ub} \\ U_{cd} & U_{cs} & U_{cb} \\ U_{td} & U_{ts} & U_{tb} \end{bmatrix} \begin{pmatrix} d \\ s \\ b \end{pmatrix}$$

where the primed quarks (d', s' and b') denote the weak eigenstates, whereas the unprimed quarks denote the mass eigenstates. The mixing matrix U, the CKM matrix, contains 4 free parameters, often denoted θ_1, θ_2, θ_3, and δ, and yields, as originally chosen by Kobayashi

Generation	Particle	Particle type	Charge	Lepton number		
				e	μ	τ
1	electron (e)	Lepton	-1	1	0	0
	anti electron (positron, $\overline{e}$)	Lepton	1	-1	0	0
	electron neutrino (ν_e)	Lepton	0	1	0	0
	anti electron neutrino ($\overline{\nu_e}$)	Lepton	0	-1	0	0
	up quark (u)	Quark	2/3	0	0	0
	anti up quark ($\overline{u}$)	Quark	-2/3	0	0	0
	down quark (d)	Quark	-1/3	0	0	0
	anti down quark ($\overline{d}$)	Quark	1/3	0	0	0
2	muon (μ)	Lepton	-1	0	1	0
	anti muon ($\overline{\mu}$)	Lepton	1	0	-1	0
	muon neutrino (ν_μ)	Lepton	0	0	1	0
	anti muon neutrino ($\overline{\nu_\mu}$)	Lepton	0	0	-1	0
	charm quark (c)	Quark	2/3	0	0	0
	anti charm quark ($\overline{c}$)	Quark	-2/3	0	0	0
	strange quark (s)	Quark	-1/3	0	0	0
	anti strange quark ($\overline{s}$)	Quark	1/3	0	0	0
3	tau (τ)	Lepton	-1	0	0	1
	anti tau ($\overline{\tau}$)	Lepton	1	0	0	-1
	tau neutrino (ν_τ)	Lepton	0	0	0	1
	anti tau neutrino ($\overline{\nu_\tau}$)	Lepton	0	0	0	-1
	top quark (t)	Quark	2/3	0	0	0
	anti top quark ($\overline{t}$)	Quark	-2/3	0	0	0
	bottom quark (b)	Quark	-1/3	0	0	0
	anti bottom quark ($\overline{b}$)	Quark	1/3	0	0	0

Table 2.1: The properties of the 3 generations of leptons and quarks, together with their antiparticles. All the particles are spin-$\frac{1}{2}$ fermions, and the lepton flavour numbers are listed in the three last columns.

and Maskawa, the parametrization for the mixing matrix which looks like this:

$$U_{ckm} = \begin{bmatrix} c_1 & -s_1c_3 & -s_1s_3 \\ s_1c_2 & c_1c_2c_3 - s_2s_3e^{i\delta} & c_1c_2s_3 + s_2c_3e^{i\delta} \\ s_1s_2 & c_1s_2c_3 + c_2s_3e^{i\delta} & c_1s_2s_3 - c_2c_3e^{i\delta} \end{bmatrix}$$

where $c_i = \cos\theta_i$ and $s_i = \sin\theta_i$. The CKM matrix can also be approximated by another well-known parametrization, the so-called Wolfenstein parametrization, which looks like this [2, page 345]:

$$U_W = \begin{bmatrix} 1 & \lambda & \lambda^3(\rho - i\eta) \\ -\lambda & 1 & \lambda^2 \\ \lambda^3(1-\rho-i\eta) & -\lambda^2 & 1 \end{bmatrix}$$

where the number $\lambda \simeq 0.22$. Here one can see that the different mixings become weaker as one gets furter away from the diagonal, that is, as one mixes over more generations. This means that the preferred reactions are the ones that create quark pairs within the same generation, and that the probability for creating quark pairs where the two quarks are of adjacent generations is more likely than the creation of quark pair consisting of a quark/anti-quark of generation 1 and a quark/anti-quark of generation 3.

The reason why the Cabbibo-Kobayashi-Maskawa mechanism does not work in the lepton sector, is that such a mixing is unobservable in MSM. This is because of the fact that any rotation will, as long as the neutrino masses are zero, still lead to zero mass eigenstates for the neutrinos. But if one allow for neutrinos with non-zero masses, such a mixing can occur, which in turn would generate LFV decays. This is one way of inducing these decays in models beyond MSM.

The next question is then of course how to bring about such massive neutrinos. The massless neutrinos are in MSM guaranteed by the fact that they are purely left-handed, that rigt handed neutrinos do not exist. This requirement can be lifted, and the absence of detection of right-handed neutrinos can be accounted for by a large mass for these right-handed neutrinos; this approach is investigated in reference [6], which uses a superstring inspired standard model, in which new neutral fermions are introduced. The branching ratios predicted by this model are in the range 10^{-6}–10^{-7} for both the $\mu\tau$ and $e\tau$ decay modes (but could be as large as 2×10^{-4}).

Another way of constructing LFV processes is by introducing new, so-called exotic particles which allow for LFV couplings. This is maybe a more populare method, as it allows for specific extentions to MSM. One of the more investigated models is the supersymmetric model, in which each particle in MSM acquires a supersymmetric partner, which has the same quantum numbers except for a change of the spin quantum number in this way: The supersymmetric particles of the spin-$\frac{1}{2}$ fermions (leptons and quarks) have spin=0, whereas the spin-1 gauge bosons have supersymmetric partners with spin=$\frac{1}{2}$. The explicit mixing can then occur in the supersymmetric sector, and reference [3] investigates this possibility, with the constraint that only the two heaviest generations (generations 2 and 3 in table 2.1) mix significantly, and that there is negligible left-right mixing. This leads to branching ratios on the $\mu\tau$ decay of $\lesssim 10^{-7}$, which will be the dominant LFV mode with such a mixing. If one, on the other hand, takes the significant mixing to be in the two first generations, the dominant LFV mode will be the $e\mu$ channel; this has been done in reference [4] with the predicted branching ratio of the Z^0 decay into $e\mu$ of $\lesssim 10^{-9}$.

Another model that predicts LFV decays, is the scalar triplet model [8], where seven new physical scalars remain after the Higgs mechanism. The LFV decays of the Z^0 from this model is investigated in reference [9], and have branching ratios of $\leq 5.9 \times 10^{-6}$ for the $\mu\tau$ channel and $\leq 7.9 \times 10^{-6}$ for the $e\tau$ channel.

Superstring theories, which are theories that aim at unifying all the forces of nature, are often constructed in such a way that they manifest themselves as en E_6 grand unified theory at energies below the Planck scale. In this theory, at lower energies, one or more Z bosons will emerge, as well as exotic fermions, and the LFV terms can now occur by the mixing of these new fermions and the usual fermions of SM. Reference [7] investigates this, and finds branching ratio upper limits of $\leq 4.2 \times 10^{-4}$ for the $\mu\tau$ decay, and $\leq 3.4 \times 10^{-4}$ for the $e\tau$ decay.

There exists another, fundamentally different, way of inducing LFV by introducing new particles, than what has been the case so for the models described so far. While all the models that have been treated so far all have used these new particles to introduce mixing in the leptonic section, following the success of the scheme used in the quark sector, it is also possible to explicitly violate lepton flavour conservation, and let the exotic particle(s) couple to LFV directly. Such a model is treated in reference [5], where a new exotic heavy neutral gauge field, Z', which couples to LFV, is introduced. This leads to branching ratios of the order $(4\text{–}6) \times 10^{-7}$ for the $\mu\tau$ mode.

Chapter 3

The DELPHI detector

3.1 General layout

DELPHI [19] (DEtector with Lepton, Photon and Hadron Identification) is one of four detectors operating at the LEP e^+e^- collider (the other three being ALEPH, L3 and OPAL). The detector is installed in a cavern 100 meters below ground level, with the main computer and control center located at the surface. DELPHI is divided into a barrel, covering approximately the polar angle region from 45° to 135°, and two endcaps, covering approximately the polar angle regions from 40° (140°) to 10° (170°). The luminosity monitors, the Small Angle Tagger (SAT), which was replaced prior to the 1994 LEP runs by the Small angle TIle Calorimeter (STIC), and the Very Small Angle Tagger (VSAT), cover the very forward direction, in polar angles from about 10° (170°) and downward (upward). Here, as well as in the rest of the paper, the coordinate system used has the z-aksis parallel to the beam, radius R and azimuth ϕ in the plane perpendicular to it and polar angle θ, with $\theta = 0$ along the beam axis, that is the z-axis, alternatively a y direction pointing upwards and an x direction pointing towards the centre of the LEP ring. Thus the xy plane denotes a plane in which the z coordinate is constant (though not necessarily zero), and similarly for the xz (constant y) and yz (constant x) planes. The plane at z=0 divides the barrel into two hemibarrels; Hemibarrel A along negative z, and hemibarrel C along positive z.

In the barrel region, most of the sub-detectors have geometrical structures which constitute planes with constant R (that is, cylinders concentric around the beam pipe), whereas most of the forward sub-detectors constitute planes with constant z (xy-planes). In the intermediate region between the barrel and endcaps around polar angles of 40°–50° (130°–140°), there is a generally more incomplete detector coverage, for which reason there has been installed new subdetectors in this polar angle range. The two most important ones of these are the Surround Muon Chambers (SMC), which were installed during the summer of 1994, and the 40 degree counters, installed during spring/summer of 1995. Of these only the SMC will be used in the analyses presented in this paper.

The detector consists of 16 different individual subdetectors, where small subdetectors of similar characteristics are added to form one partition, while large subdetectors are divided into two partitions. An overwiev of the general layout of DELPHI is found in figure 3.1, where all of the important subdetectors, including all the ones used for the three analyses, are shown. Below some of the subdetector is presented in a little more detail; not all the subdetectors will be treated, only the ones most important for the analyses, which, since the analyses is done only in the barrel, will be the barrel subdetectors.

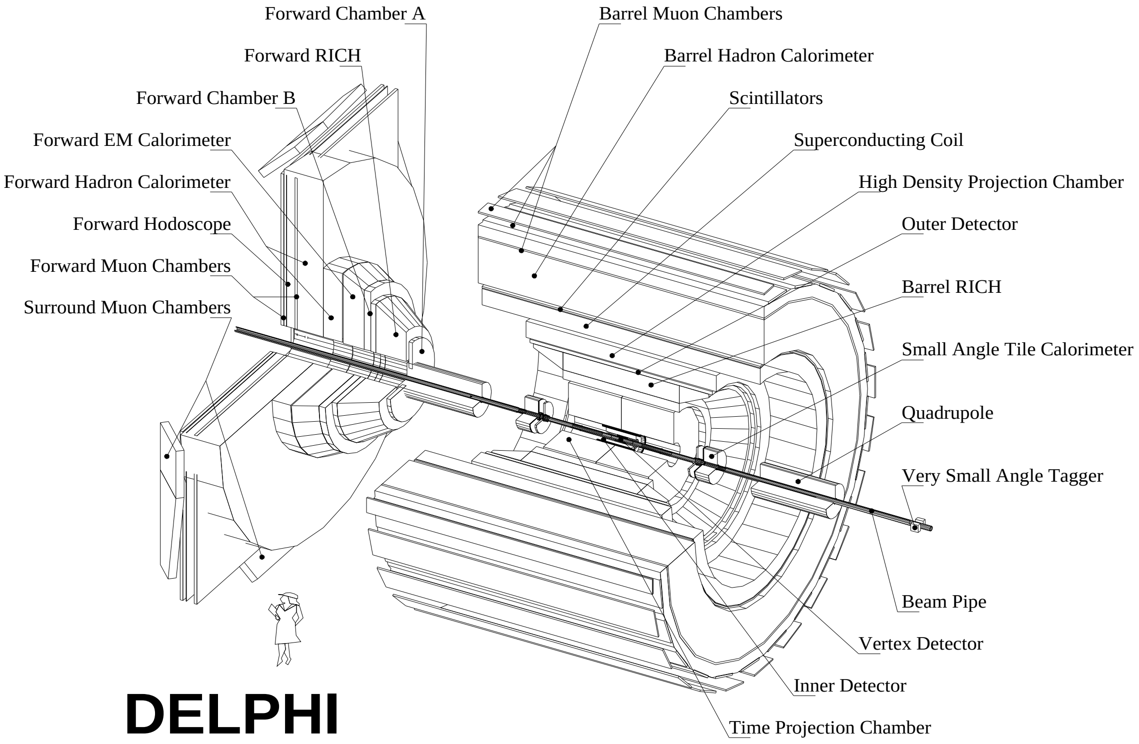

Figure 3.1: General layout of the DELPHI detector

3.2 Solenoid

The superconducting solenoid has a length of 7.4 m and an inner diameter of 5.2 m (dimensions of the cryostat). The single conductor layer (5000 A), with two 35 cm long end sections containing a second layer to improve field homogeneity creates a magnetic field of 1.2 T. Very good field homogeneity is required for the long-drift detectors, and the longitudinal component of the field lies well within 12334+1/-10 G (indicating a weak axial asymmetry) with negligible azimuthal variation: the radial component is < 5 G. The aluminium support cylinder is cooled from the outside by forced flow of liquid helium at 4.5 K.

3.3 Trigger system

The main purpose of the trigger [12] is to select, with the highest possible efficiency, all physics events originating from real electron-positron interactions, being sensitive to any sort of interesting physics channel, while, at the same time, keeping the background event rate reasonably low. The trigger system is designed to fire on *single* charged or neutral particles, covering as wide an angular region as possible. In addition to the decision logic, the DELPHI trigger system also has the important task of controlling and synchronizing the digitization of the data for the entire experiment.

The trigger system is currently structured into 4 successive levels of increasing selectivity; T1, T2, T3 and T4. T1 and T2 are hardware triggers and synchronous with respect to the beam cross over (BCO), and have been active since the start of DELPHI in August 1989. T3 was implemented in 1992 with the aim of maintaining the data logging rate close to 2 Hz, and T4 since 1993.

T1 behaves as a pre-trigger and only very loose requirements, such as simple patterns in track chambers, scintillation counter hits or low energy single clusters in calorimeters, are considered in the decision. No correlation between different subdetectors is introduced. In T2, signals from different subdetectors are considered together, and subdetectors with long drift times, not available at T1, are taken into account. In order to have a high efficiency for physics events, T2 is organizen in different θ regions; the barrel, the endcaps and the intermediate region.

One of the problems with the high redundancy of T2, is the high contamination from events not originating from electron-positron interactions. In fact, only ~20% of the T2 triggers contain real physics events. For this reason, the T3 is introduced as a software filter in order to enrich the data events written to tape. The cuts in T3 are essentially the same as in T2, but with the added advantage that T3, being a software trigger, makes use of the digitized data comming from the subdetectors. Thus, calibration constants can be applied, allowing to set sharper thresholds in the energy showers and/or tighter cuts on the pointing of tracks towards the primary vertes.

The original object for T4 was to tag, in real time, all Z^0 decays produced in the detector. Nonetheless, after T3, the event rates are sufficiently low to envisage a more complete processing of the data. Thus this last trigger level is also used for quality checking of the data, and performing the decoding necessary to display the data.

3.4 Tracking detectors

3.4.1 Vertex Detector (VD)

The VD consists of three concentric shells of Si-strip detectors at average radii of 6.3 cm (closer shell), 9.0 cm (inner shell) and 11.0 cm (outer shell), covering the central region over a length of 23.6 cm (20.8 cm for the closer shell), corresponding to a polar angle coverage in the range 25°–155°, 36°–144° and 43°–137°, respectively (see figure 3.2). The main goal of the VD is to provide maximum $R\phi$-resolution; 5 μm single track resolution and ≤ 100 μm double track separation. The Closer and Outer layer consists of double sided double metal strip detectors providing both $R\phi$ and z coordinates, whereas the Inner layer gives $R\phi$ points only.

Each shell consists of 24 modules with ~10% overlap in ϕ between the modules. Each module contains 4 detectors along z, with the detector strips parallell to the beam axis, and each detector in turn has a sensitive length of 59 mm and a width of 25.6 mm, (for 512 readout channels) or 32 mm (for 640 readout channels) for the Inner and Outer shell, respectively. The number of readout strips in the Inner and Outer shell totals 54254. Laboratory measurements have given a signal/noise ratio of 15/1 for a minimum ionizing particle (mip) for the Inner and Outer shell combined.

The mechanical structure of the VD is water cooled to guarantee good thermal stability, and the thickness of the VD is only ≈1.1% of a radiation length, thus retaining high efficiency and low energy loss. The relative alignment of the modules is monitored in two different ways:

- Light spots focused to 12 of the outer modules, giving a sensitivity of ~10 μm in R and < 5 μm in ϕ.
- 18 Capasitive displacement probes, giving a sensitivity of < 1 μm in R and ~6 μm in ϕ.

Stability at LEP is found to be < 1 μm radially over 10 days.

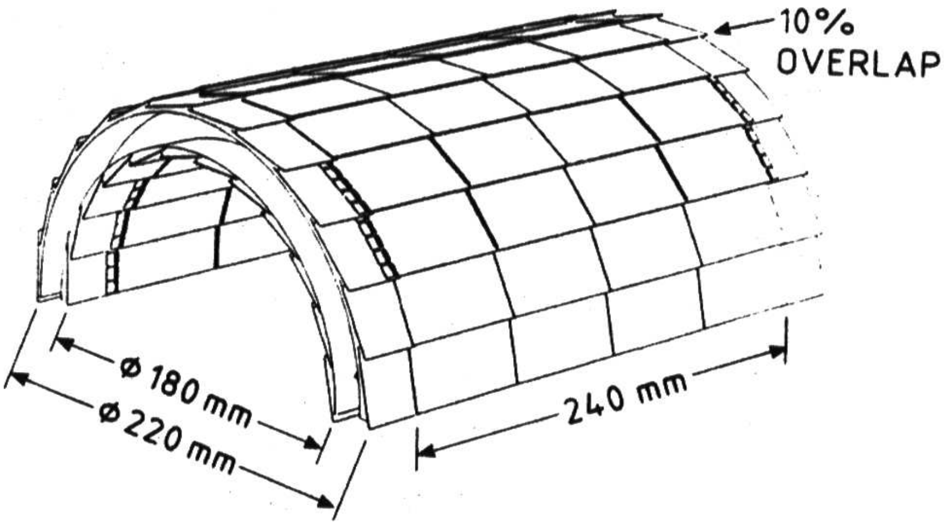

Figure 3.2: The geometrical structure of the VD. Only the inner and outer shells are shown (the closer shell has a $\emptyset$ of 126 mm).

3.4.2 Inner Detector (ID)

The ID is a cylindrical tracking and triggering detector made up of two parts:

- An inner drift chamber with jet-chamber geometry, providing up to 24 points in $R\phi$. The chamber is divided into 24 azimuthal sectors.
- 5 cylindrical Multi Wire Proportional Chambers (MWPCs) each layer consisting of 192 wires and 192 circular cathode strips with about 5 mm pitch, proportional to R. The wires provide fast trigger information and dissolve left/right ambiguities from the jet chamber, whereas the strips give z information.

This structure covers an region of 116 to 280 mm in R (the jet chamber from 116 to 223 mm and the MWPCs from 230 to 280 mm) and out to a value of $|z|$=40 cm for the jet chamber, $|z| \leq$50 cm for the MWPCs, giving a polar angle coverage of approximately 17° to 163° for the jet chamber, and 30° to 150° for the MWPCs. See figure 3.3 for an azimuthal view of the ID.

The gas of the jet chamber is a ($CO_2/C_4H_{10}/$ C_3H_7OH) mixture of 94.85%/4.5%/0.65% respectively. This, together with the configuration of the field wire grids, gives a drift velocity proportional to R, leading to a very narrow time window ($\sim$100 ns) for the trigger information for radial tracks. For the MWPCs, the gas mixture is (Ar/CO_2) in a 70%/30% mixture. The sense wires are spaced about 8 mm apart and interleaved with field wires.

The resolution of the ID has been measured to 90 μm in the $R\phi$ direction (jet chamber), and to $<$ 1 mm in the z direction (MWPCs). Efficiencies of typically 20 points/track in the jet chamber and 95% per layer in the MWPCs have also been measured, while trigger efficiencies have found to be about 90% for the jet chamber, and above 95% for single tracks for the MWPCs.

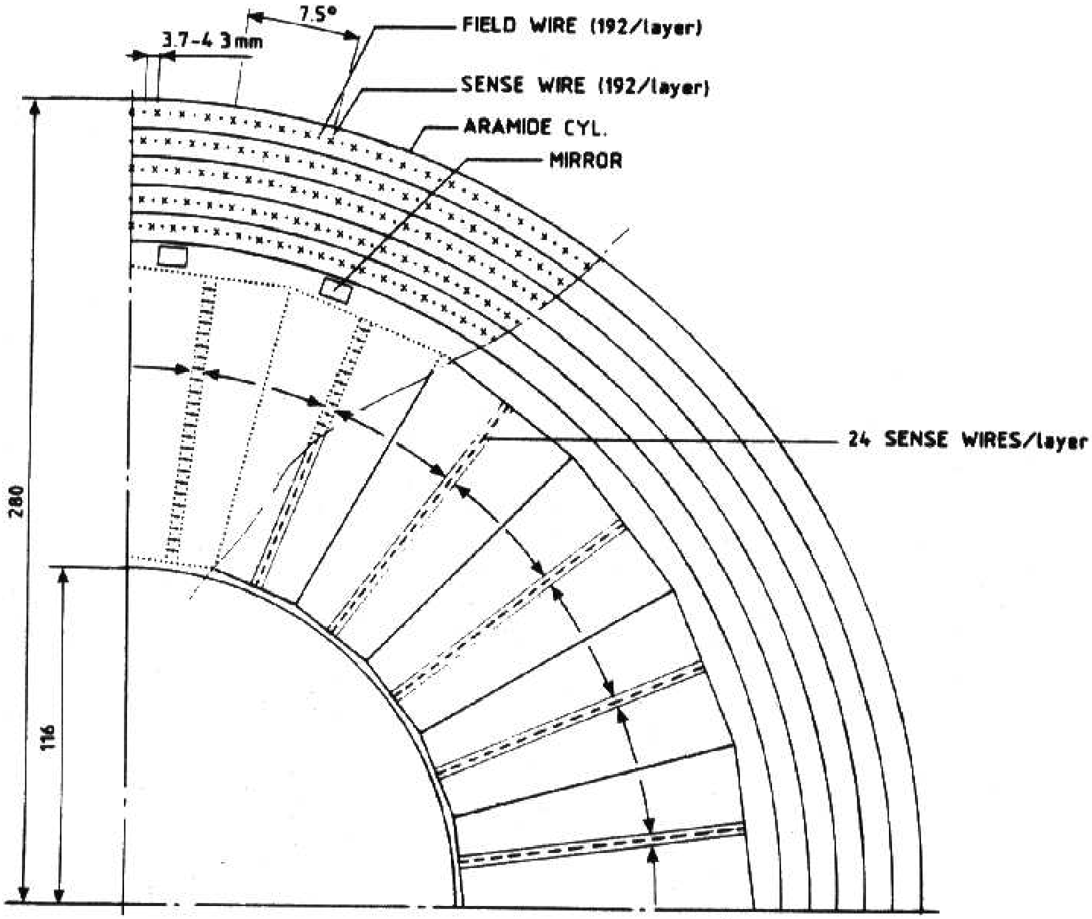

Figure 3.3: An azimuthal view of an 90 degree (in ϕ) cut out, showing the structure of the ID.

3.4.3 Time Projection Chamber (TPC)

The TPC is the principal tracking device of DELPHI. Because of the Barrel Ring Imaging Cherenkov Counter (Barrel-RICH), situated from R=123 cm to R=197 cm, which is the principal particle identification element in DELPHI, the operation of the TPC is specified at 1 atm. This gives a reduced $\mathrm{d}E/\mathrm{d}x$ response, which will nevertheless be usefull, in particular for the separation between electrons and pions below an energy of 8 GeV.

The TCP extends radially from 35 cm to 111 cm, and in z up to $|z|$=134 cm, yielding a polar angle acceptance of approximately 20° to 160°. The endcaps are divided into 6 sector plates with 192 sense wires (spacing=4 mm; gap=2 × 4 mm) and 16 circular pad rows of constant spacing arranged in MWPC structure. Se figure 3.4 for a view of the geometry of the TPC. The TPC is divided in two by a high voltage plane at z=0, splitting it into two drift volumes, and creating a drift field of 150 V/cm. A particle traversing the TPC drift volume creates about 70 ionized atoms/electrons per cm of gas, which is an 80%/40% mixture of Ar and CH_4 respectively. The drift velocity is 66.94 ± 0.07 mm/μs at T=22° Celsius. The $\mathrm{d}E/\mathrm{d}x$ measurement is done by the 192 sense wires at the endcaps.

The MWPCs at the endcaps provide up to 16 space points for a non-looping particle. The resolution for these space points si in $R\phi$ in the range 180–280 μm (depending on ϕ and z), while approximately 900 μm in the z direction. The $\mathrm{d}E/\mathrm{d}x$ resolution is σ=5.8% for muons at 45 GeV and 7.5% for pions between 280 and 400 MeV.

3.4.4 Outer Detector (OD)

The OD was introduced into DELPHI in order to provide good momentum resolution in $R\phi$, improving on the constraints that the Barrel-RICH imposes on the geometry of the TPC. It also provides fast trigger information in both $R\phi$ and z.

Having as its goal full azimuthal coverage, the OD is composed of 24 modules, structured as 15 degree partitions in ϕ, each consisting of 145 drift tubes in 5 layers. It is situated outside the Barrel-RICH, extending radially from R=198 cm to R=206 cm, and in z up to $|z|$=232 cm, giving a polar acceptance of 43° to 137°. This structure provides 3 space points in the z direction, and 5 in the $R\phi$ direction. The particle detection is done by the drift tubes operating in the limited streamer mode, giving a signal with short raise time and high amplitude (typically 3 ns and 80 mV). The resolution is 110 μm in $R\phi$ and 4.4 cm in z.

3.4.5 The muon chambers

The muon chambers are structured as the outer layer of the DELPHI detector, utilizing the unique ability of muons to penetrate the iron of the HCAL, making (ideally) muons the only particles able to reach the muon chambers. The muon chambers are divided into three sections; the barrel muon chambers, covering a polar angle of 52° to 128°, the forward muon chambers, covering a polar angle of approximately 10° to 43° (137° to 170°), and the surround muon chambers, covering the polar angle region around 40°–50° (130°–140°). The surround muon chambers were installed during 1994, and were operational from the period end of August/beginning of September the same year. Only the barrel and surround muon chambers are used in the analyses, and the description of the forward muon chambers will therefore be omitted.

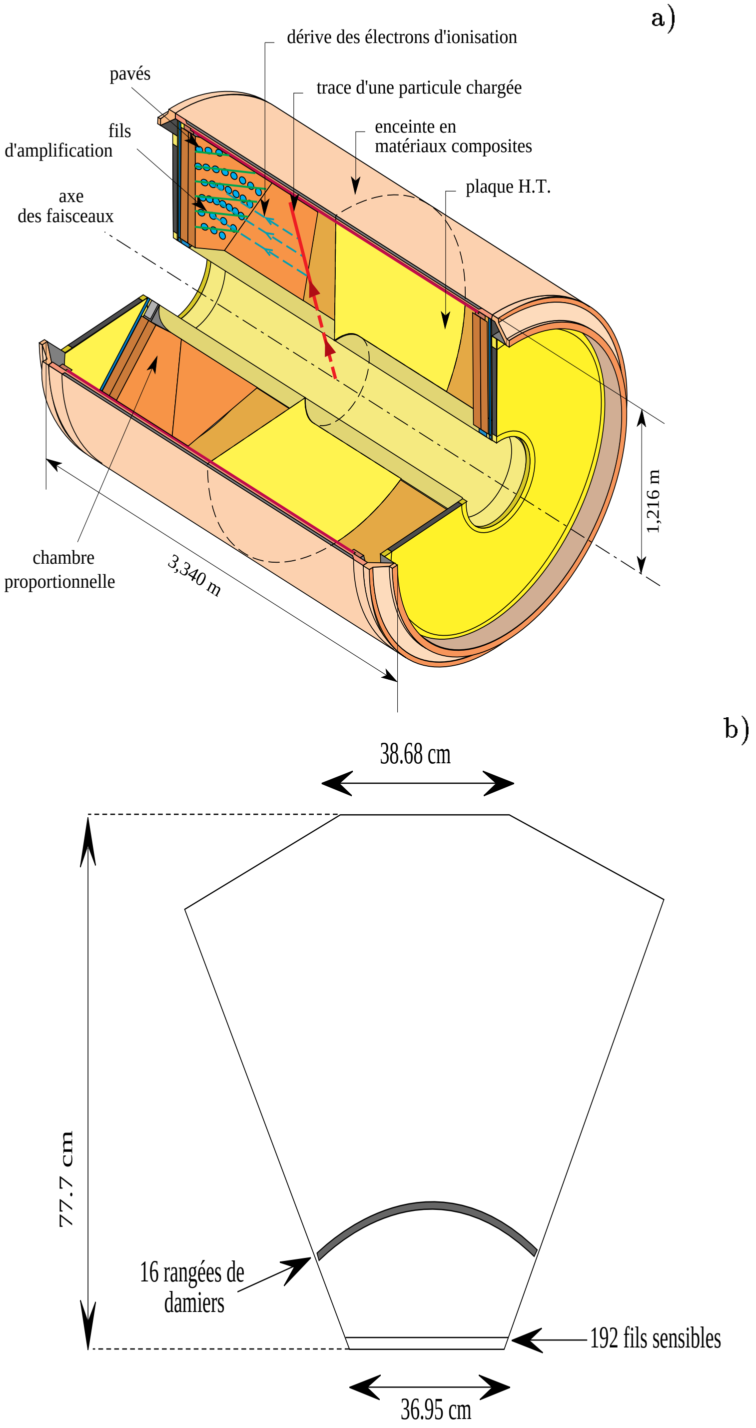

Figure 3.4: A schematic view of the TPC subdetector. **a)** shows the overall geometrical properties and the most important parts, while **b)** shows one of the six sectors of the endcap.

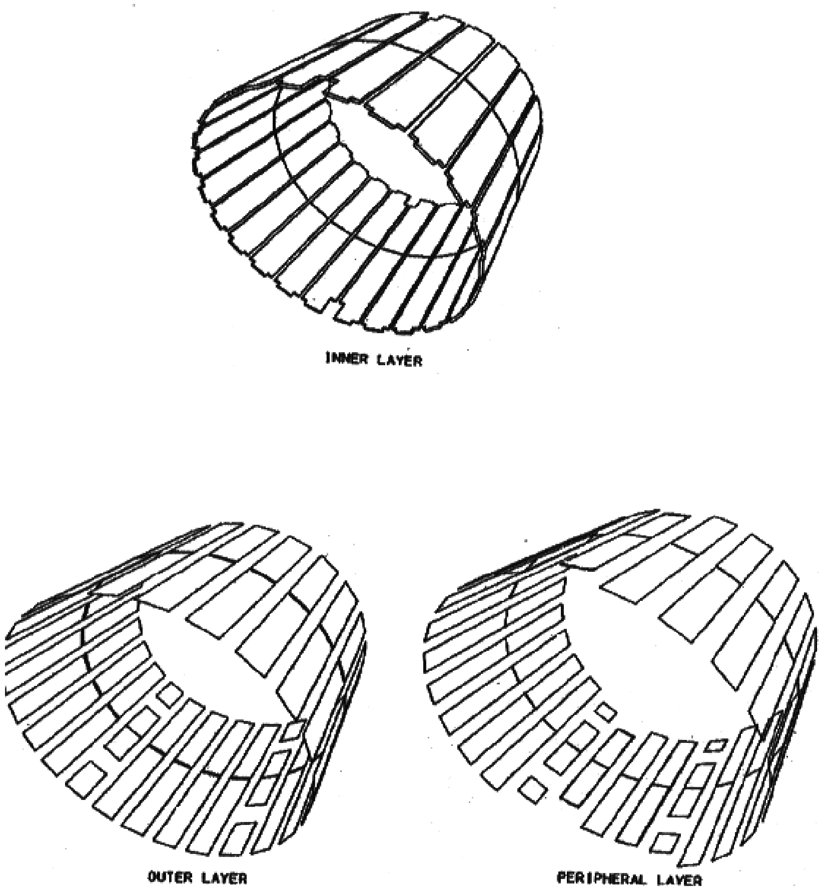

Figure 3.5: The three layers of the MUB; the inner, outer and peripheral layers. The structure of 2×24 planks is appearent.

The Barrel MUon chambers (MUB)

The main purpose of the MUB is to measure space points for particles traversing past the HCAL, which ideally should be only muons. The MUB consist of 1372 drift chambers, and is arranged into three concentric layers; the inner, outer and peripheral layers. Each layer is a structure of 2×24 planks, 24 in the A hemibarrel and 24 in the C hemibarrel, with 2 additional sectors between the legs of the detector; se figure 3.5.

The inner layer is inserted into the return yoke after 90 cm of iron, and consists of three staggered drift chamber planes, where the third plane normally is used only as a backup for the two first. The outer layer is mounted on the outside of the yoke, behind a further 20 cm of iron, and consists of two overlapping planes of staggered drift chambers. The peripheral layer is placed even furter out, and ofset in ϕ by 7.5° in comparison to the inner and outer layers, in order to cover the regions in ϕ where there is a gap in the inner and outer layers. See figure 3.6.

A typical chamber is 20.8 cm wide, 2.6 cm high and 365 cm along the z-axis. The anode wire is held at a potential of 6150 V, while the cathode, which has the form of two series of 12 grading strips, is hald at a potential of 4000 V in the central strip. The potential then

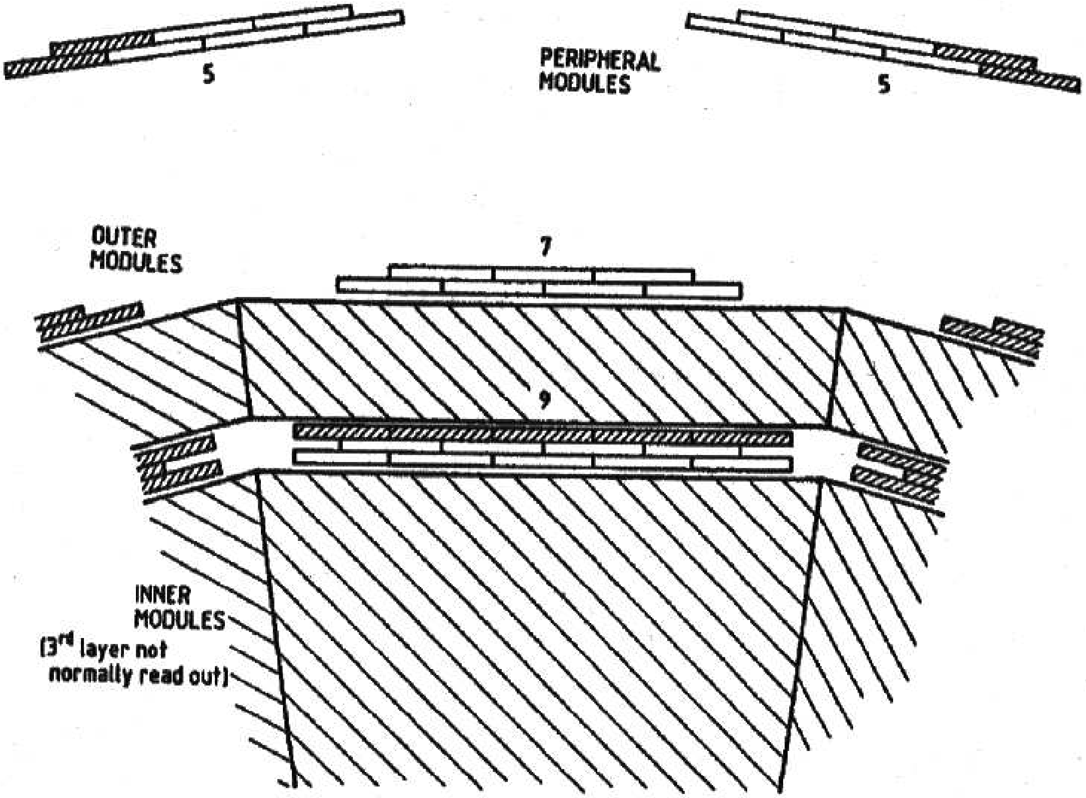

Figure 3.6: A cut in the xy plane, showing the placement of the MUB inner, outer and peripheral modules. Note the structure of the 14 chambers in three planes in the inner layer (structured as 5, 4, and 5 chambers, respectively), and the 7 chambers in two planes in the outer and peripheral layers (structured as 4, and 3 chambers, respectively).

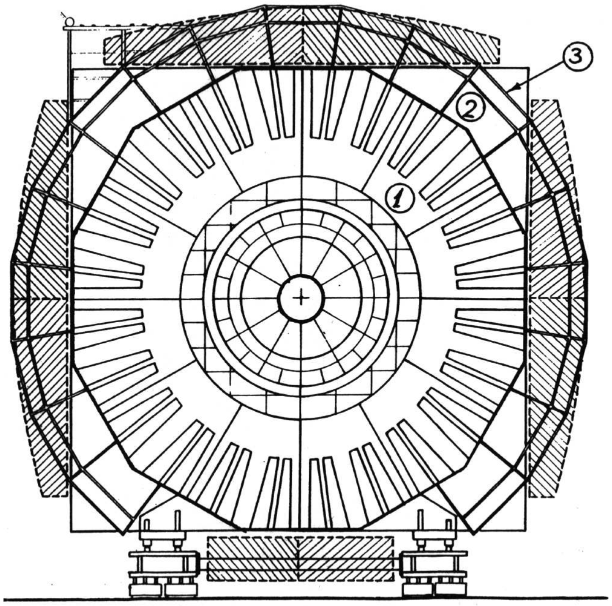

① – Endcap iron.

② – Forward Muon Chambers

③ – cable trays mounted on the iron

Figure 3.7: A cut in the xy plane, showing the placement of the SMC (shaded region). The endcap is shown from the inside of DELPHI.

drops uniformly from strip to strip until the edge of the chamber, which is earthed. The gas of the drift chambers, which operate in the proportional mode, is a ($Ar/CH_4/CO_2$) mixture of 85.5%/8.5%/6.0% respectively. An individual chamber efficiency of 95% provides a very high total efficiency for muon tracks with typically 4 hits per track. The resolution on extrapolated tracks is measured to be 2 mm in the $R\phi$ direction, and ~80 mm in the z direction for muon pair events.

The Surround Muon Chambers (SMC)

The SMC [14, 15] has as its main task to cover the holes in the polar angle acceptance between the MUB and the MUF (Forward MUon chambers), which corresponds to the polar angle region of approximately $45°–50°(130°–135°)$ in θ. The detector consists of 8 parts mounted at the top, sides and bottom of both endcaps, as shown in figure 3.7, where 4 of the 8 parts, corresponding to one of two endcaps, are shown. Each part consists of 2 modules, and each module of 2 planes. The size of the modules is approximately 4×1.5 m^2.

The support for the modules is mounted on the endcap as shown in figure 3.8, in a structure that can be rotated, and thus provide the SMC with two positions: the *working* mode, in which the SMC is inclined to give the maximum coverage for muon detection, and the *open* mode, achieved by a rotation of about 45°, which allows movement of the endcaps and access to the barrel sub-detectors. This structure is used for the parts mounted on the top and sides of the endcap, whereas the ones mounted on the bottom of the endcap are not required to move. See figure 3.9, which also illustrates the polar angle acceptance of the SMC.

The detectors are plastic streamer tubes of the same design as those of the HCAL. Each tube contains 8 chambers (cells of 9$\times$9 mm^2), with 70 μm anode wires and high resistive graphite painting as a cathode. The tubes in the two planes are staggered by a distance equal to half a tube plus half a chamber size to overcome the deadspace arising from the 1 mm walls between chambers. The space resolution is approximately 1 cm and single hit efficiency close to 100% both for anodes and strips.

3.5 Scintillator counters

3.5.1 Time Of Flight (TOF)

The main purpose of the TOF is to provide accurate timing of the particles traversing DELPHI, serving as a fast trigger, which can be used to veto cosmic muons during the Beam Cross Over (BCO).

The TOF consists of a single layer of 172 counters with dimensions of $355 \times 19 \times 2$ cm^3. The detector is placed at a radial distance of 310 cm, outside of the solenoide, and mounted on the inside of the return yoke. It covers an angular region of θ=41° to 139°, with a dead zone 6 cm wide around θ=90°, and at the support legs of the cryostat.

Time resolution has been measured from cosmics to be σ_t=1.2 ns, corresponding to σ_z=20 cm. Very high efficiency has been achieved, and set to 99.9% for minimum ionizing particles (mips).

3.6 Calorimetry

The calorimetry is divided into three parts; the electromagnetic calorimetry, treated in subsection 3.6.1, the hadronic calorimetry, treated in subsection 3.6.2 and the calorimetry for Bhabha events in the very forward direction, used for the luminosity measurements, treated in subsection 3.6.3. Each of these three tasks have their own specific subdetector, with the luminosity calorimetry having two different and independent subdetectors, one of which was replaced before the start of the 1994 runs.

3.6.1 High density Projection Chamber (HPC)

The HPC is the main electromagnetic calorimeter in DELPHI. It utilizes the time-projection principle for measuring energy, and is one of the first large-scale detectors to do so. Attention has been paid to secure very high granularity in all coordinates, in order to separate electromagnetic showers from close tracks. The dynamic range of the HPC allows for electromagnetic showers with full sensitivity from mip range up to 50 GeV showers.

The HPC is situated right inside the solenoid, but outside of the OD, covering the radial region of 208 to 260 cm. The length of the HPC is $|z| \leq 254$ cm, giving an polar angle acceptance of 43° to 137°. The subdetector is segmented into 24 parts in the $R\phi$ direction, and 6 in the z direction, giving a total of 144 modules. The geometry of a module is a trapezoid box with a width (distance along ϕ) at smallest R (208 cm) of 519 mm, and largest R (260 cm) of 638 mm. Height (in R) and length (in z) of each module is

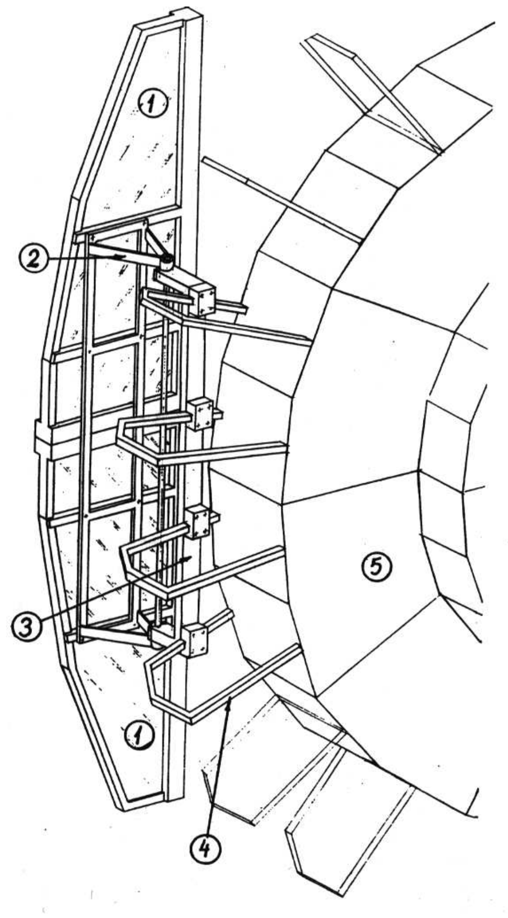

① – SMC modules

② – rotating part of the support

③ – fixed part of the support

④ – existing cable trays

⑤ – endcap iron

Figure 3.8: Design of the support for the sides and top parts of the SMC modules.

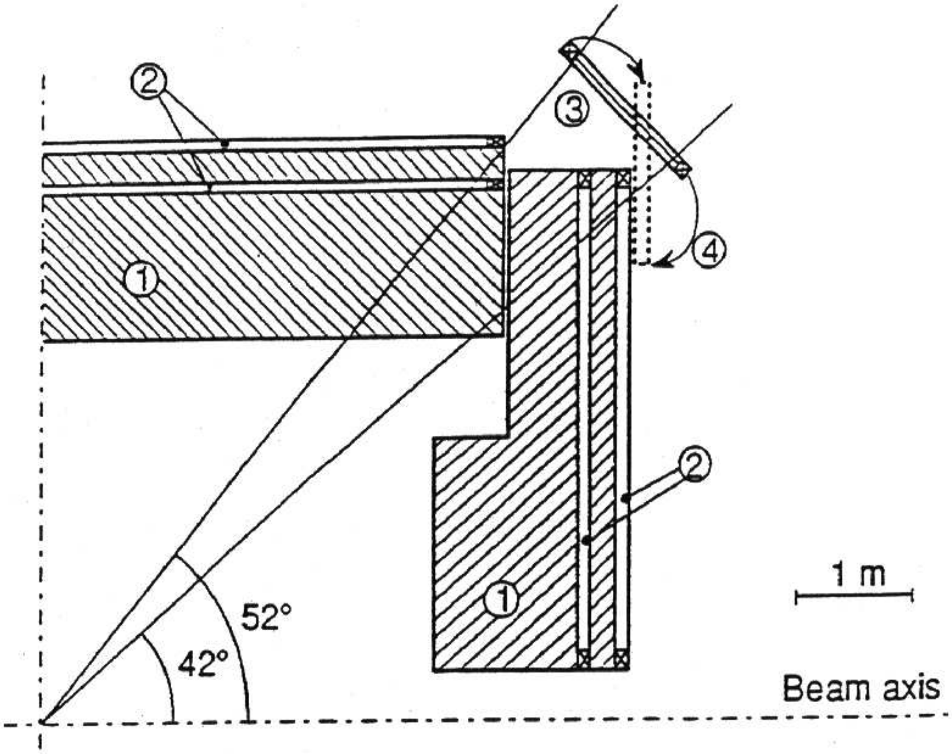

① – Hadron Calorimeter.

② – Muon Chambers: the peripheral MUB chambers are not shown

③ – "working" position of the SMC

④ – "open" position of the SMC

Figure 3.9: A cut in the yz plane, showing the geometrical acceptance of the SMC in the θ is shown, in the range 42°–52°.

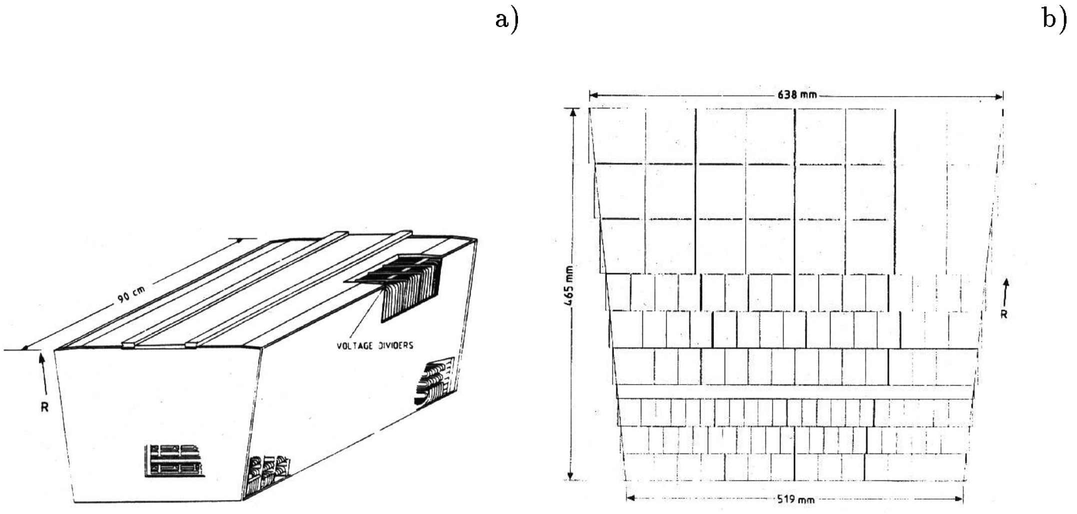

Figure 3.10: The geometrical shape of a typical HPC module. **a)** shows a 3D view of the module (length in the z direction 90 cm), while **b)** shows a cut through the xy plane which reveals the pad-structure and the 9 radial layers.

465 mm and 900 mm, respectively, except for modules in the first and last rings, which are somewhat shorter in z. Se figure 3.10 for a view of a single HPC module. The modules are offset by 7.5° in ϕ with respect to the HCAL to achieve optimal azimuthal angle coverage. Gaps between modules are 1 cm in z and ϕ, except for a gap of 7.5 cm at z=0.

The time-projection principle is realized by using the lead converter as electric field cage, projecting the ionization charge onto a single MWPC plane at one end of each HPC module. The converter consists of 41 lead walls spaced by 8 mm gas gaps. Each layer is formed by thin trapezoidal lead wires glued to both sides of a fiberglass-epoxy support. A longitudinal drift field (along z) of approximately 100 V/cm is set up by a voltage gradient between neighbouring lead wires. A particle traversing an HPC module, will then shower in the lead walls, with the ionization electrons drifting in the gas gaps to the MWPC at the end of the module. The gas is a mixture of 80% Ar and 20% CH_4. This structure has an attenuation length of 3–4 meters, while the mazimum drift distance is only 85 cm.

The aim of few electronics subparts was achieved, with the readout being performed by as few as 18432 channels (128 pads in each of the 144 modules), giving a granularity of 4 mm along z, 1 degree in azimuth (ϕ) and nine samplings in the R direction.

3.6.2 Hadron CALorimeter (HCAL)

The HCAL is a sampling gas detector incorporated in the magnet yoke. It covers polar angles from 42.6° to 137.4° in the barrel, and from 11.2° (168.8°) to 48.5° (131.5°) in the two end-caps. Only the barrel part of the HCAL will be described here, and thus the term HCAL will refer to the barrel part of the Hadron CALorimeter.

The HCAL is divided into 24 sectors in ϕ, in the same manner as the HPC modules, and offset by 7.5° with respect to these (as mentioned earlier). The detector itself consists of 20 layers of limited streamer mode detectors inserted into 2 cm slots between the 5 cm iron plates in each sector. The detectors are wire chambers which consist of a plastic cathode

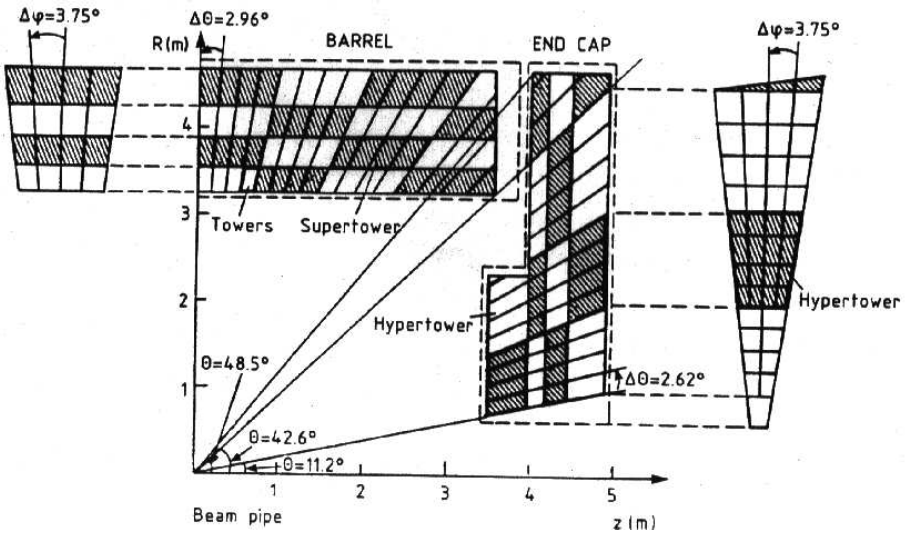

Figure 3.11: A cut in the yz plane, showing the polar angle acceptance of the HCAL, barrel and forward. The structure of towers, suypertowers and hypertowers is also shown.

forming 8 cells of 0.9×0.9 cm with one 80 μm anode wire in each. The inner surface of the cathode cells is coated with a poorly conductive graphite varnish.

The gas of the HCAL is a (AR/CO_2/i-butane) mixture of 10%/60%/30% respectively, which gives an average induced charge of 10 pC on the external readout boards, which is placed at a potential of 3.92 kV relative. These readout boards are combined into pads which pick up the streamer charges, and the pads of four adjacent layers are again combined into a tower, which is shaped to point to the interaction point. Each tower covers an angular region of $\Delta\phi$=3.75°, and $\Delta\theta$=2.96°, and has typically dimensions of 25×25×35 cm^3 Se figure 3.11 for a view of the layer, tower and supertower structure of the HCAL.

By combining the HCAL energy measurements with the momentum measurements from the TPC, good linearity has been found in the HCAL for energies up to 10 GeV, and in fact linearity up to 60 GeV has been found for a single sector in a beam test. The energy resolutions has been measured to about $120\%/\sqrt{E}$.

3.6.3 The luminosity monitors

Accurate measurements of the luminosity has proven to be an important task for the LEP experiments, as it is crucial in the determination of the electroweak parameters from the line shape of the Z^0 cross section. Thus the original luminosity monitor of DELPHI, the SAT, was, prior to the 1994 LEP run, replaced by the STIC, which has improved resolution and accuracy compared to the former. The VSAT is used as an independent and fast luminosity monitor, and also in the monitoring of machine operation. It operates in the very forward arm.

The luminosity measurement is obtained from the equation

$$N = \sigma \cdot \mathcal{L} \qquad \Rightarrow \qquad \mathcal{L} = \frac{N}{\sigma}$$

where the quantities N and σ refer to the process $e^+e^- \rightarrow e^+e^-$. The cross section for this process is well known and calculable from theory, and it has its largest values in the forward direction, that is for polar angles close to 0° (or 180°). Thus the luminosity is essentially obtained by counting the number of Bhabha events, and divide that number by the cross section corresponding to the luminosity monitor in use.

The Small Angle Tagger (SAT)

The SAT is divided into two arms, both arms consisting of a calorimeter and a tracker in front. The tracker covers a sensitive region of 43.5 to 120 mrad, and is designed to give a precision of σ_θ=1.5 mrad and to define the acceptance radius to about 40 μm. The calorimeter of the SAT covers an area in R from 10–36 cm at a z distance of 233–285 cm, giving a polar angle acceptance of 43–135 mrad (corresponding to 2.5°-7.7° in θ). It consists of alternating layers of lead sheets (0.9 mm thick) and plastic scintillating fibres ($\emptyset$=1 mm), alligned parallel to the beam, giving a total thickness of 28 radiation lengths. The exact acceptance of the SAT is defined by a lead mask with a thickness of 10 radiation lengths, where the conocal outer surface defines the acceptance radius to < 100 μm.

Behind the calorimeter, the fibres are collected in 144 bundles per arm, with the number of fibres in each bundle ranging from 450–800. The efficiency for light collection is $\approx$70%, and the diode quantum efficiency $\approx$90% at the peak. An energy resolution of $\sigma_E/E = ((1.2^2 + 11.4^2/E)^{1/2} + 2.3)\%$, where the 2.3% term comes from response variations across the module, has been measured on a 45° prototype.

The readout is performed in 8 radially concentric rings, giving a radial segmentation of 3 cm (3.2 cm for the outer 2 rings). The inner 4 rings have a segmentation of 15° in ϕ, while the outer 4 rings have a segmentation of 7.5° in ϕ. There is a 2 cm wide dead-zone in the vertical plane, due to the separation between the two arms.

The Small angle TIle Calorimeter (STIC)

The STIC [16, 17] is composed of two sylinders, placed at a distance of z=$\pm$220 cm, which covers, at the front, a range of R from 65 to 420 mm, giving a polar angle coverage of 29–180 mrad. The exact acceptance of the detector is defined by a tungsten mask, machined with a precision of 10 μm, in front of the STIC.

The STIC is a sampling calorimeter, composed of 49 layers of 3.4 mm steel laminated lead plates and 3 mm scintillator tiles, giving a total thickness of approximately 27 radiation lengths. Layers 8 and 15 are substituted by planes of silicon detectors with strips of width 1.7 mm in azimuthal, in order to provide good measurements of the θ position of the showers, thus giving a total of 47 active lead/scintillator layers. See figure 3.12 for a view of one of the 47 scintillator planes.

After scintillation in the scintillator planes, the light from the tiles is read by wavelength shifter fibres with a diameter of 1 mm, with a density of fibres of approximately 1 fibre per cm^2. The scintillator planes are mounted on each lead plate, and are optically isolated from each other. The tiles of one half-cylindre are arranged in 8 azimuthal sectors 22.5° in ϕ and 10 radial sectors, giving a total of 320 towers for all four half-cylinders (two at positive and two at negative z). The number of fibres per tower varies from 9 in the inner radial ring, and up to 34 at the outer. All fibres in a tower is bundled together at the back of the calorimeter. The systematical errors are minimized by requiring a precission accuracy of 50 μm for the calorimeter mechanics, giving a 0.2% systematic error.

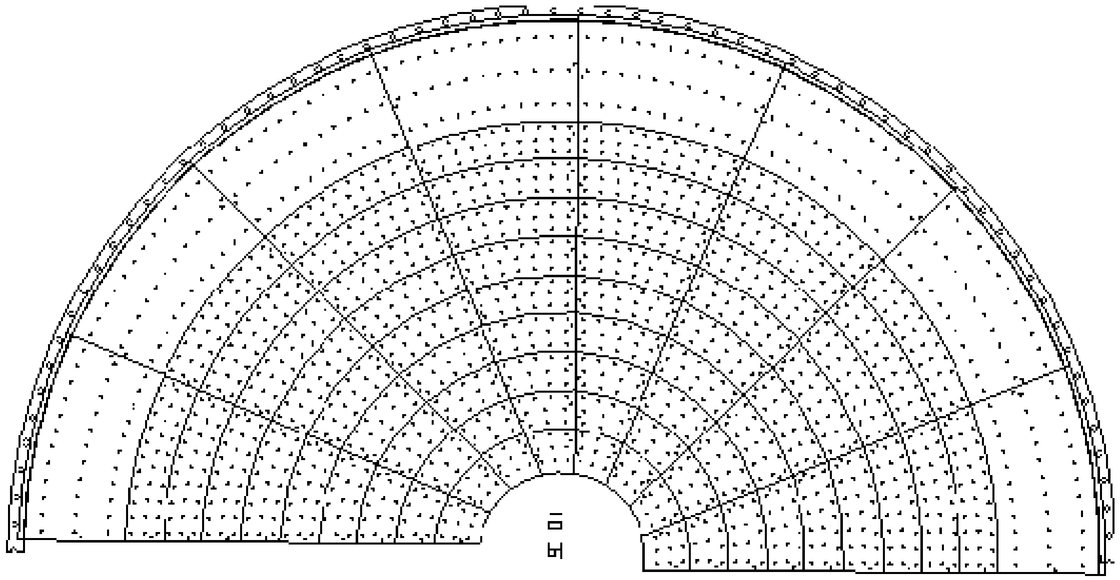

Figure 3.12: A cut out in the xy plane, showing the upper half of one of the 47 layers of lead/scintillator of the STIC. Note the 1600 holes for the wavelength shifters to go through, as well as the 10 radial and 8 azimutal sectors.

This detector structure gives an energy resolution at 45 GeV of approximately 3%, and spacial uniformity better than 2%. The spacial resolution of the STIC alone is 1.5° in ϕ and 0.3–1 mm in R. For each event, the energy of each of the 320 towers, the silicon detector information from 3840 silicon strips and information from the veto counters, the 64 scintillator wedges in front of the STIC, used to separate charged showers from neutral ones, is recorded.

The Very Small Angle Tagger (VSAT)

The VSAT operates in the very forward arm, as it is placed in a distance of 770 cm in the z direction from the interaction point, covering a polar angle range of 5–7 mrad (6 to 8 cm from the beam axis). It provides an independent luminosity measurement with very high statistics, due to the peak of the Bhabha cross section in the very forward direction, and is also monitoring the machine operation. The detector in each arm consists of two rectangular W-Si calorimeter stacks, 24 radiation lengths deep, with a geometrical size 5 cm high, 3 cm wide, and 10 cm long. The 4 blocks, 2 on positive and 2 on negative z, are mounted to both horizontal sides of the elliptic beam pipe and fixed to the support of the superconducting quadrupoles, covering a azimuth of $\pm 45^\circ$ around the horizontal axis.

Each block consists of 12 W-plates, 2 radiation lengths thick, interleaved with full area Si-detectors, 3×5 cm^2. Two Si-plates with 32 vertical strips (1 mm pitch) are inserted behind 5 and 9 radiation lengths, and another plane with 48 horizontal strips is inserted behind 7 radiation lengths. An energy resolution of 5% with 45 GeV Bhabha events has been measured for fully contained showers ($35\%/\sqrt{E}$).

Chapter 4

The signature of the $Z^0 \rightarrow l_i\overline{l_j}, i \neq j$ events

4.1 Signal

The signal in the three channels all have similarities, and features that separate them clearly, with respect to the distribution of certain variables, from other decays of the Z^0. But in all three analyses there are, to a certain degree, backgrounds which have tails into the signal area (see subsection 4.2), which is important, due to the fact that the lepton flavour violating decays of the Z^0 are rare, if not absent.

Of the three lepton flavours, the tau lepton is the only one which will decay before it has traversed the DELPHI detector; the mean life τ of the three particles are: $\tau_\tau \approx 2.96\times10^{-13}$s, $\tau_\mu \approx 2.20\times10^{-6}$s, $\tau_e \geq 2.7\times10^{23}$yr (at 68% CL). The decay products of a lepton of flavour i will always, or at least almost always, since the LFV decays are known to be small, contain at least one neutrino of the same flavour, ν_i, and even two neutrinos, if the decay is leptonic, and this (these) neutrino(s) will, since they only interact through the weak force, not be stopped by the detector. This in turn means that a certain amount of energy is carried away undetected whenever a tau is produced, which is generally not the case for a muon or an electron. For this reason the signal in the $e\mu$ channel has a slightly different signature than that of the $\mu\tau$ and $e\tau$ channels.

4.1.1 The $e\mu$ channel

The signal in the $e\mu$ channel is characterized by a simple topology of a single beam energy track in each hemisphere, one track being an electron and the other a muon. This signal is the one most clearly separated from the backgrounds, as will be explained in section 4.2, and therefore the analysis in this channel has the least tight cuts, resulting in an efficiency of approximately twice that of the $\mu\tau$ and $e\tau$ channels.

4.1.2 The $\mu\tau$ and $e\tau$ channel

The signal in the $\mu\tau$ and $e\tau$ channel is characterized by a topology of one hemisphere consisting of a single beam energy track (a muon in the $\mu\tau$ case and an electron in the $e\tau$ case) opposite a hemisphere with one, three of five tracks and missing energy. The amount of missing energy will vary according to how much energy is carried away by the neutrino(s), but one should note that this missing energy has a spectrum which goes all the way down to zero. This creates a much more severe background problem in the $\mu\tau$ and $e\tau$ analyses than what is the case in the $e\mu$ analysis; this will be treated more thoroughly in subsection 4.2.

Because the tau in the one hemisphere can, and often does (in approximately 17.5% of the cases), decay into muons (electrons), there is in the $\mu\tau$ ($e\tau$) signal events a significant probability that the final state will contain two muons (electrons) in opposite hemispheres. This is of course the topology of the muon (electron) pair events, and one must therefore, in order not to be totally overshadowed by background from these channels, incorporate in the analysis strong muon (electron) vetoes in the hemisphere which is to contain the tau lepton.

4.2 Background

The most important background for these signals is the decay

$$Z^0 \rightarrow \tau^\pm + \tau^\mp$$

with the subsequent decays in at least one of the hemispheres

$$\tau \rightarrow \mu + \nu_\tau + \nu_\mu \qquad \text{or} \qquad \tau \rightarrow e + \nu_\tau + \nu_e$$

The first case will then look just like the $\mu\tau$ signal, whereas the second one will look just like the $e\tau$ signal, with the only distinction that these tau pair background events involve neutrinos beside those from the decay of the tau in the hemisphere opposite of the muon (electron), which is not present in the $\mu\tau$ ($e\tau$) signals. These neutrinos will "escape" the detector and carry away certain, often large, amounts of energy undetected. This in turn leads to lower muon momentum (electron electromagnetic energy) in the $\mu\tau$ ($e\tau$) topology, and a higher degree of acolinearity. It is also noteworthy that for the $e\mu$ analysis, two coinciding tau decays, one to an electron and the other to a muon, is required. Since the signal in this case does not contain a tau lepton, there is no energy loss due to neutrinos in any arm, thus making the $e\mu$ signal more different from the $Z^0 \rightarrow \tau^\pm + \tau^\mp$ background than the $\mu\tau$ and $e\tau$ signals.

Even if the tau pair background generally gives smaller energies and momenta for the muon (electron) in the $\mu\tau$ ($e\tau$) background events, it is important to notice that the energy carried away by the neutrinos has a distribution which goes all the way down to zero, resulting in a tail in the tau pair background stretching all the way up and into the expected signal area. See figure 4.1 for the distributions of the momentum (normalized electromagnetic energy) of the muon (electron) normalized to the beam energy in the $\mu\tau$ ($e\tau$) signal events for tau pair background and real signal events.

In addition to this background, there is also a smaller background from the two channels

$$Z^0 \rightarrow \mu^\pm + \mu^\mp \qquad \text{and} \qquad Z^0 \rightarrow e^\pm + e^\mp$$

where one of the two particles (e or μ) is "misinterpreted". Although this background is negligible in number compared to the background from $Z^0 \rightarrow \tau^\pm + \tau^\mp$, it is in some cases equally important, since there in this background are no neutrinos carrying away energy undetected, and the background from these two channels will therefore often lie in the expected signal region. This will typically be the case for muon pair background in the $\mu\tau$ analysis, where one muon is misidentified as a tau, passing the muon veto in the

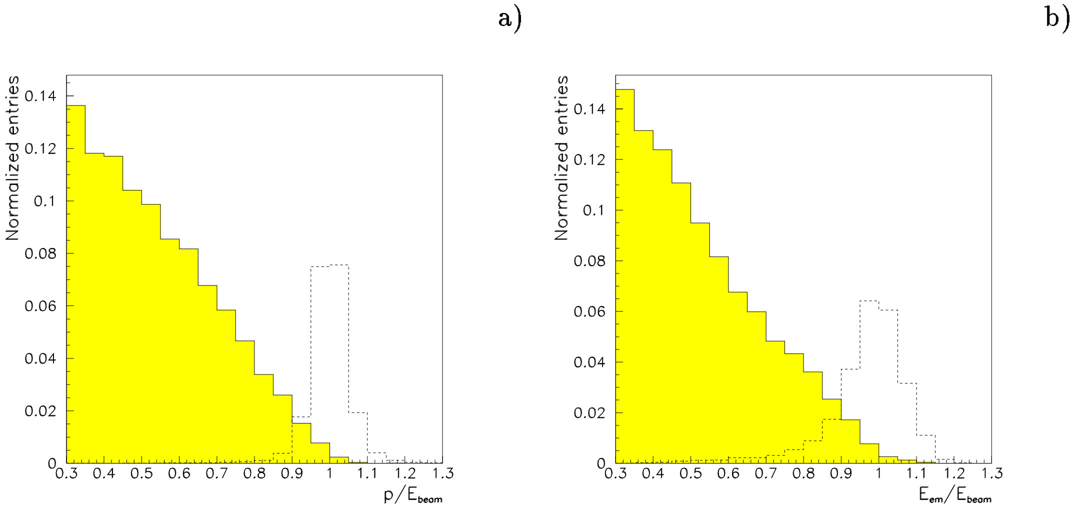

Figure 4.1: The shape of the tau pair background spectrum compared to the signal spectrum for $\mu\tau$ and $e\tau$ signal events. Shaded histogram is Monte Carlo simulated tau pair background, and dashed histogram is Monte Carlo simulated signal. **a)** shows the normalized momentum spectrum for muons in $\mu\tau$ candidate events, while **b)** shows the normalized electromagnetic energy spectrum for electrons in $e\tau$ candidateevents.

tau selection, and the other muon then is a beam energy muon, as is expected from the signal. In the same manner, the same effect will occur for electron pair background in the $e\tau$ analysis.

The Monte Carlo simulated samples of tau pairs, muon pairs, and electron pairs were generated with the simulation programs BABAMC [23], DYMU3 [24], and KORALZ [25], respectively, with detector response simulated by the DELSIM simulation package [27]. These samples were used for simulation of the background (see section 6.3 for the treatment of the background in the procedure to calculate a 95% CL upper limit), but also in part to determine the efficiency of the three analyses (see sections 5.3.6, A.1 and A.2). The low statistics Monte Carlo simulated samples of signal events were generated with modified versions of the KORALZ [25] program, and used for efficiency calculations (see section 5.3.6). All Monte Carlo samples, with the exception of Monte Carlo signal samples for 91F, were generated for each year version (91F, 92D, 93C, and 94B) with the DELSIM simulation package [27] tuned to the detector configuration for that specific year version. For the 91F signal Monte Carlo samples, the 93C signal Monte Carlo samples, specially smeared to fit the 91F data, were used.

The size of the different samples varies from year to year and from channel to channel, according to availability and need. The total number of events, both generated Monte Carlo and data samples, are listed in table 4.1. The most significant difference between the years, beside the steady increase of the data samples, is the notably larger signal Monte Carlo generated samples for the 92D year version. This is due to the fact that the event generator computer power was not as hard pressed when these samples were made, as was the case when the 93C and 94B samples were made.

Year	Real data	Monte Carlo generated samples					
		e^+e^-	$\mu^+\mu^-$	$\tau^+\tau^-$	$\mu\tau$	$e\tau$	$e\mu$
91F	38002	23008	43791	66740	—	—	—
92D	100833	61185	105243	187971	18742	8834	19897
93C	108450	69473	151680	122572	3169	3153	3386
94B	201649	32532	87856	105918	3200	3308	3606

Table 4.1: The sizes of the different data and Monte Carlo generated samples for the 4 years the analyses are performed. For the real data samples, the number cited corresponds to the number of events written to the ntuple, while for the Monte Carlo generated samples, the number refers to the number of generated events.

Chapter 5

The analyses

5.1 The overall structure of the analyses

All three analyses are performed in a similar fashion, which can be summarized up in the following:

Introductory selection cuts: These cuts are:

- Cuts to select leptonic events from hadronics and cosmics
- Detector quality cuts
- Cuts to define the acceptance of the analysis
- Cuts to reduce cosmics

These cuts are all treated in section 5.3, subsections 5.3.1, 5.3.2, 5.3.3, and 5.3.4.

Search for a high energy lepton: All three analyses search for topologies with at least one high energy lepton. In the $\mu\tau$ ($e\tau$) analysis, the high energy lepton is a muon (an electron), whereas the $e\mu$ analysis searches for two high energy particles. A high energy lepton of the correct flavour was to be found in one and only one of the hemispheres in order to fulfill the requirements in the analyses. The cuts to select such high energy leptons were all performed on variables specific to one hemisphere, and will be treated in subsections 5.4.1, 5.5.1, and 5.6.1 and 5.6.2.

Search in the hemisphere opposite of the high energy lepton: After a high energy lepton of the right flavour was found in one and only one hemisphere, the analyses proceeded by searching in the other hemisphere. For the $\mu\tau$ ($e\tau$) analysis, this hemisphere was to contain the decay product(s) from a tau. If one in the $\mu\tau$ ($e\tau$) analysis allowed for the tau decaying to a muon (an electron), the signal would be totally swamped by the muon (electron) pair background. Therefore, the analysis could not allow tau decays to muons (electrons); thus this hemisphere contained strong veto cuts against muons (electrons). The decay product(s) need not necessarily be high energetic, as the one or, in the case where the τ lepton decays to a muon or an electron, two neutrinos, ν_τ and possibly ν_e or ν_μ, may carry away large energies undetected, as previously explained in section 4.1. In the $e\mu$ analysis, both tracks were to be high energetic, and the search proceeded by searching for the other high energy lepton. All three analyses required this particle, the particle in the hemisphere opposite of the first high energy lepton, to be detected in this hemisphere only. The specific cuts to search for τ lepton decay product(s) are treated in subsections 5.4.2, and 5.5.2.

Cuts common to both hemispheres: After the two correct leptons were identified, the event was subjected to a few cuts on global variables, not assigned to a specific hemisphere. For these cuts, the variables used were such as the radial momentum and the radial electromagnetic energy (defined in section 5.3.1, under "cuts to define good events"), and the acolinearity of the event, where the signal is distinctly different from both the τ lepton pair background, and the μ and e lepton pair background. The actual cuts are treated in subsections 5.4.3, and 5.5.3.

5.2 Smearing and other corrections to specific variables

Since the background for the analysis was computed from Monte Carlo simulated events, and the signal is at best an extremely small one, it is vital that the Monte Carlo distributions agree well with the ones from real data. For this reason, several adjustments were made to some of the variables in the Monte Carlo samples. The different year versions (91F, 92D, 93C, and 94B) needed different smearings, and the corrections were performed for three different variables:

5.2.1 Smearing of normalized momentum (p/E_{beam})

This variable was smeared differently for electrons and other particles (smeared from the spectrum of muon pairs), and also differently according to whether or not the OD had detected the particle. The smearing consisted of a multiplicative shift of the peak, with a subsequent gaussian smearing, or, in some rare cases, an "anti-smearing" performed in order to squeeze the distribution into a tighter peak with smaller spread. Examples of smearings are shown in figures 5.1 (muon pairs) and 5.2 (electron pairs).

5.2.2 Smearing of electromagnetic energy response (E_{em}/E_{beam})

This variable was smeared for electrons only, and consisted of a multiplicative shift with a subsequent gaussian smearing, and an additional correction of the shape by an appropriate function. An example of smearing for electron pairs is found in figure 5.3.

When the momentum and electromagnetic energy had been smeared individually for electrons, no further smearing of the variable E_{em}/p (electromagnetic energy divided by momentum), an important variable in the identification of electrons, was needed. See figure 5.4.

5.2.3 Hadronic energy response

The hadron calorimeter response has a rather severe dependence on the polar angle θ (see figure 5.5), and this creates an angular distribution in the HCAL that one would like to avoid. There is also a slight dependence on the azimuth ϕ, but no corrections were applied for this. The HCAL response was therefore multiplied by a function that approximated the inverse of the angular dependence of the response in the calorimeter; this function is simply $\sin^2(\theta)$ in the barrel (θ between 45° and 135°) and $\cos^2(\theta)$ in the forward direction. This was done for all 4 layers of the HCAL, thus giving a relatively flat response as a function of θ in all layers. The final fixing of the HCAL response consisted of mutliplying

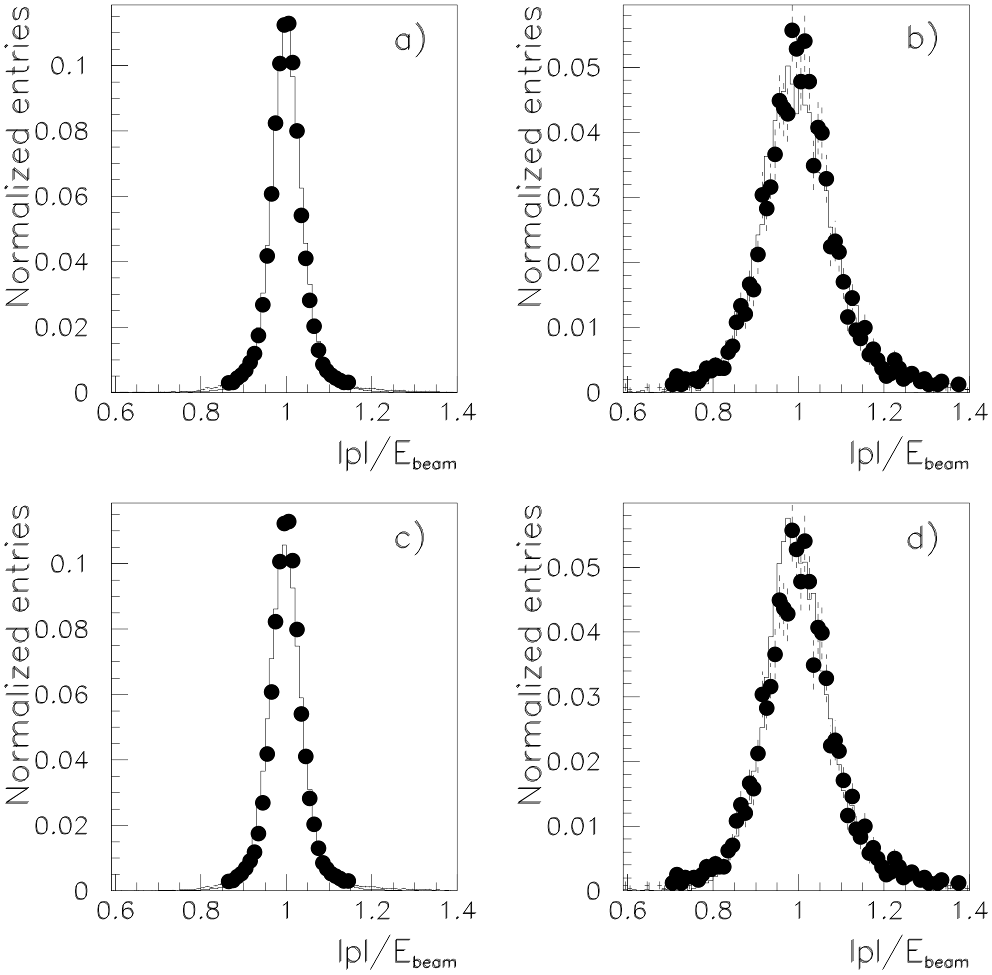

Figure 5.1: Momentum for single muons in tagged muon pairs, normalized to the beam energy; histogram is Monte Carlo muon pairs, and black dots are data. Figures **a)** and **c)** show the normalized momentum distribution when the OD has detected the muon, whereas figures **b)** and **d)** show the case where the OD did not detect the particle. In figures **c)** and **d)**, the unsmeared Monte Carlo is shown.

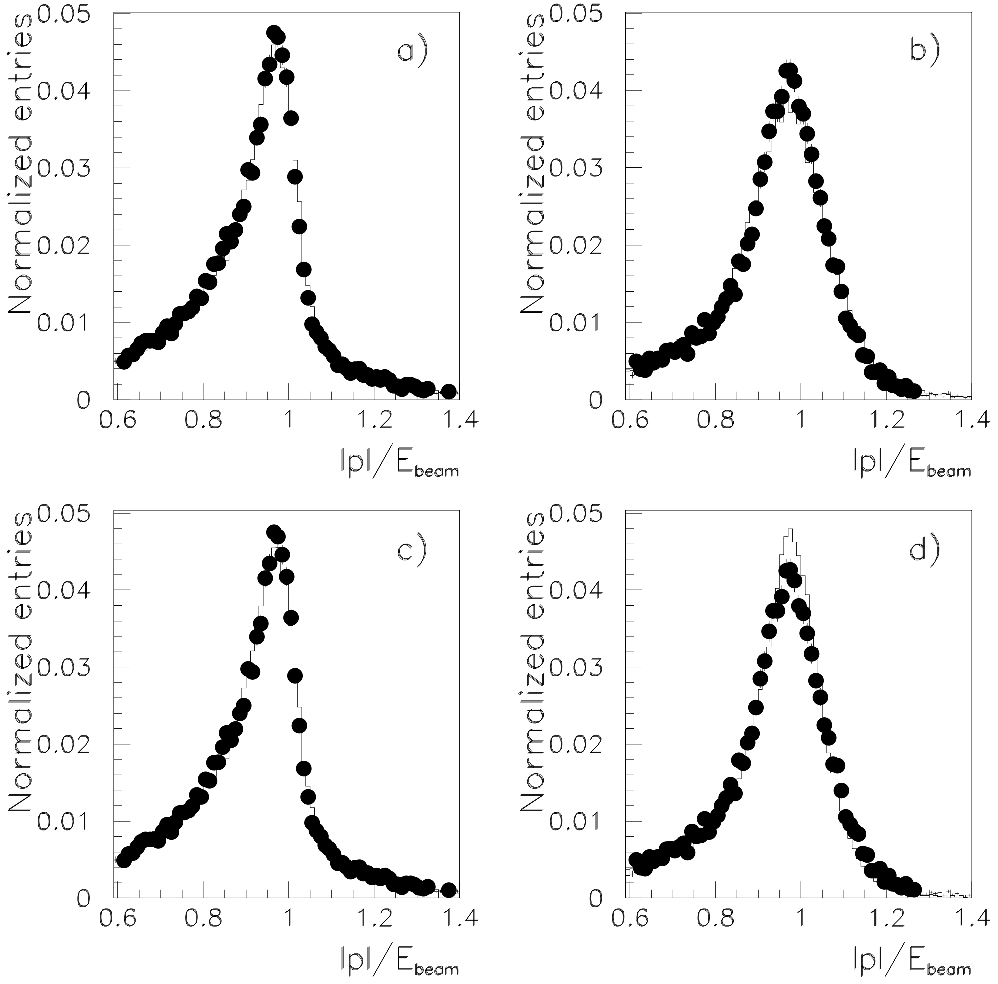

Figure 5.2: Momentum for single electrons in tagged electron pairs, normalized to the beam energy; histogram is Monte Carlo electron pairs, and black dots are data. Figures **a)** and **c)** show the normalized momentum distribution when the OD has detected the electron, whereas figures b) and d) show the case where the OD did not detect the particle. In figures c) and d), the unsmeared Monte Carlo is shown.

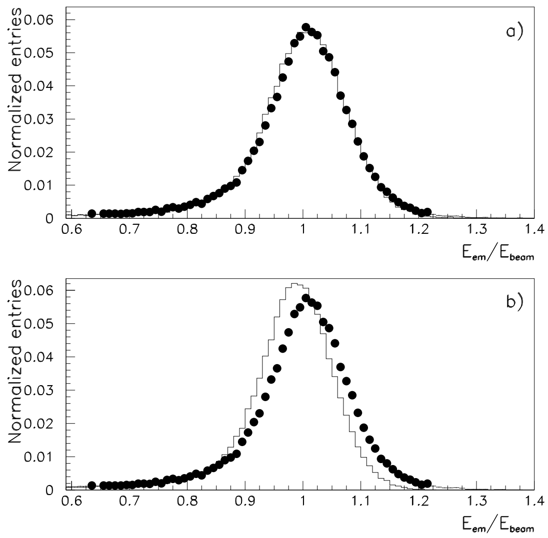

Figure 5.3: Electromagnetic energy associated to the track for single electrons in tagged electron pairs, normalized to the beam energy; histogram is Monte Carlo electron pairs, and black dots are data. Figure **a)** shows the normalized electromagnetic energy distribution after smearing, whereas figure **b)** shows the unsmeared Monte Carlo.

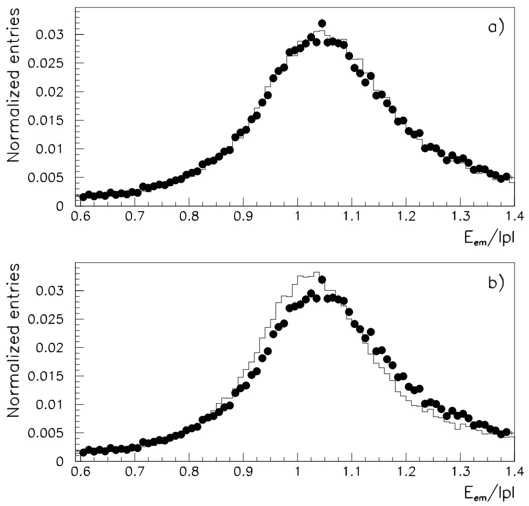

Figure 5.4: Electromagnetic energy associated to the track divided by the momentum for single electrons in tagged electron pairs; histogram is Monte Carlo electron pairs, and black dots are data. Figure **a)** shows the distribution after smearing of both normalized momentum (p/E_{beam}) and normalized electromagnetic energy (E_{em}/E_{beam}), whereas figure **b)** shows the unsmeared Monte Carlo.

the response of each layer with a constant factor (which was different for each layer, for each year versions, and also differed for Monte Carlo and data), calibrated such that muons would have an average response in each layer of 1.

Since the hadronic energy for *all* particles were corrected in this manner (not just muons), this operation changed the hadronic energy unit from GeV to mip, Minimum Ionizing Particle (i.e. muon response). When this correction was applied to all 4 layers of the hadron calorimeter, a new variable was created: EHL (Energy par Hcal Layer). This variable is the sum of the energies of the hcal layers (in mip) divided by the number of layers with energy deposited. This EHL variable is a very useful variable in isolating muons from other particles; see figure 5.6

5.3 Features common to the three analyses

5.3.1 Leptonic preselection

The leptonic preselection consisted of a set of common cuts on the topology of the event. Leptonic events are topologically "simpler" than hadronic events, with fewer tracks. There is also a larger degree of colinearity in leptonic events. These cuts also aim at removing cosmic events in the sample, thus creating an event sample that, after the cuts have been performed, has a negligibly low background from other channels than $Z^0 \rightarrow l_i l_j$, where $i, j = e, \mu, \tau$.

Cuts to define good tracks

The cuts to define good tracks were the following:

- Maximum impact parameter in the R-direction at 1.5 cm
- Maximum impact parameter in the z-direction at 4.5 cm

  Here impact parameter denotes the absolute value of the distance of closest approach to the nominal vertex.

These cuts select tracks from real e^+e^- collisions, removing cosmics, and beam gas and beam wall events.

Cuts to define good events

The cuts to define good events were the following:

- Maximum number of prongs: 12
- Minimum number of prongs: 0
- Maximum number of tracks: 6
- Minimum number of tracks: 2

  The information on prongs and tracks are read from the LongDST [30] data tapes on which the analyses are run, which in turn comes from the DELANA [28] and TANAGRA [29] analysis packages used for track extrapolation and coordination of information from the different subdetectors.

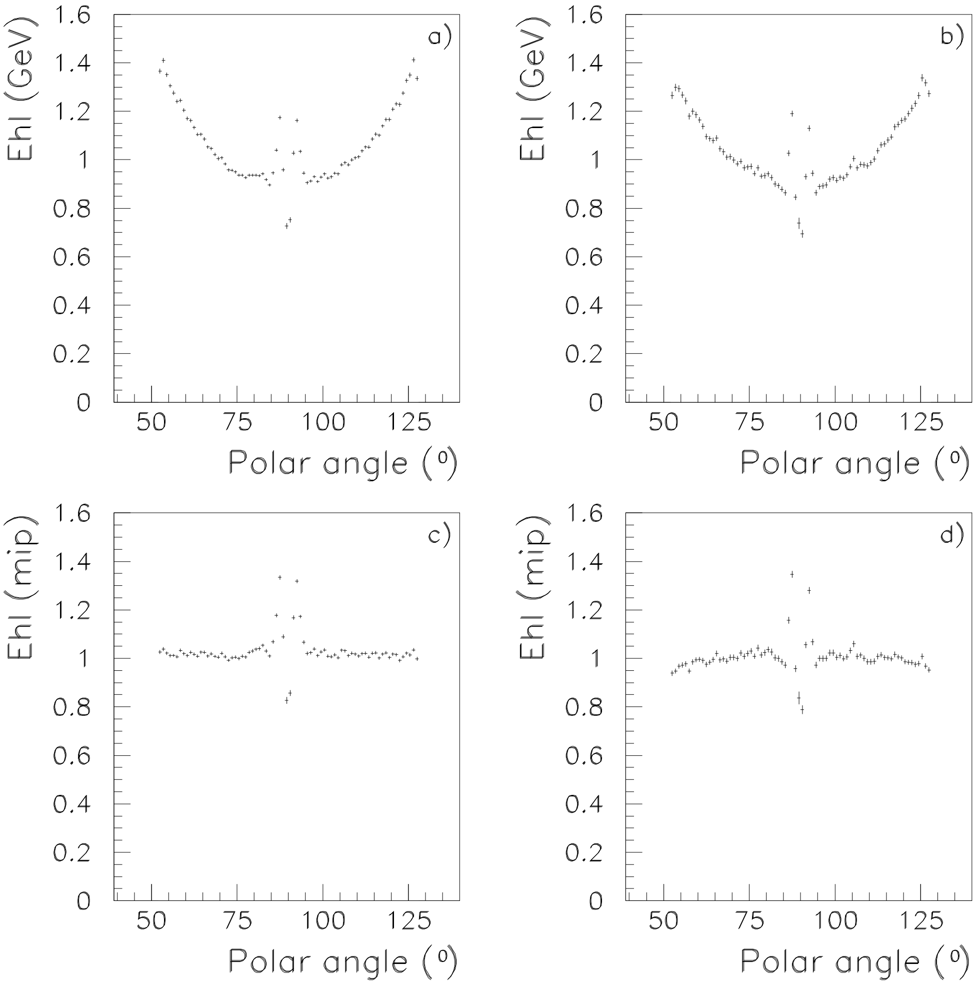

Figure 5.5: Plots showing the EHL variable (hadronic energy per layer) for muons selected by the muon selection routine of the $\mu\tau$ analysis, before and after the fixing described in section 5.2.3. Plots **a)** and **b)** show the unfixed variable (energy units GeV), and plots **c)** and **d)** show the variable after fixing (energy unit mip). Plots **a)** and **c)** are Monte Carlo muon pairs, whereas plots **b)** and **d)** are data.

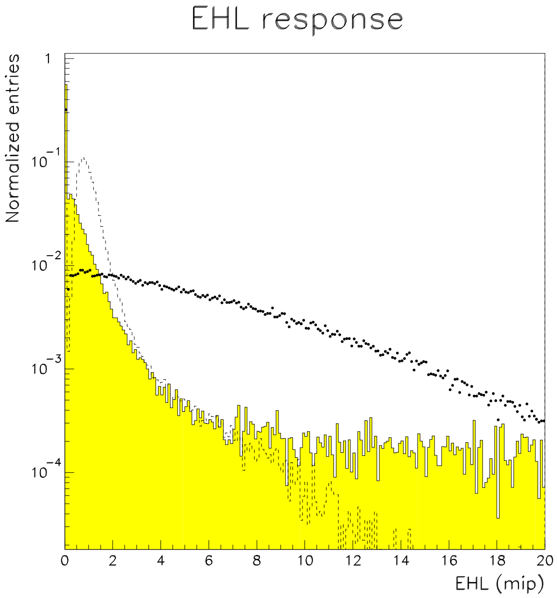

Figure 5.6: Plots showing the EHL variable (hadronic energy per layer) for different Monte Carlo generated particles. The shaded hitogram shows the electron response, the dashed shows muon response and the band of black dots shows the response from hadronic decay products from taus.

- At least 1 track in each hemisphere

  The two hemispheres are found by first defining the thrust axis $\vec{n}$ as the vector of a specific length (normally set to 1) which maximizes the sum

  $$\sum_{i=1}^{n_{track}} |\vec{p_i} \cdot \vec{n}|$$

  which is a sum over all tracks (n_{track} is the number of tracks in the event). The plane perpendicular to the thrust axis $\vec{n}$ then defines the two hemispheres.

These cuts on tracks and prongs have as their primary goal the removal of hadronic events, that is $Z^0 \rightarrow q_i\overline{q_i}$, where q_i denotes a quark of type i, $i = u, d, c, s, b$ (the t quark is too heavy to be produced at LEP). Hadronic events generally have many more tracks, and these cuts therefore enrich the leptonic content in the sample, while maintaining a relatively high efficiency. Studies on Monte Carlo simulated events show that these cuts remove approximately 12% of the mupair sample, from 6 to 7% of the electron pair sample and 18 to 20% of the tau pair sample, the exact numbers depending on the different year samples.

- Maximum radial momentum: 2000 GeV

  Here the variable "radial momentum" is defined as:

  $$p_{rad} = \sqrt{(p_1)^2 + (p_2)^2}$$

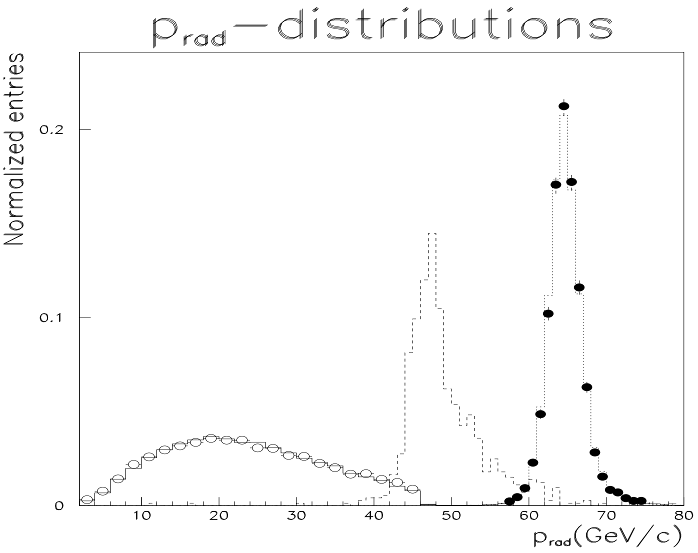

Figure 5.7: Radial momentum distribitions. Solid histogram is Monte Carlo tau pairs, open circles are tagged tau pairs in data. The dashed histogram is Monte Carlo muon pairs, black dots are tagged muon pairs in data. The dotted histogram in the center is the Monte Carlo generated $\mu\tau$ signal.

where p_1 (p_2) is the momentum of the leading charged track in hemisphere 1 (2). Thus a beam energy (i.e. 45 GeV) mupair would have a radial momentum of $\sqrt{2}\times 45$ GeV$\simeq$ 63.6 GeV.

- Maximum radial electromagnetic energy: 2000 GeV

  Here the variable "radial electromagnetic energy" is defined as:

$$E_{rad} = \sqrt{(E^1_{em,30^\circ})^2 + (E^2_{em,30^\circ})^2}$$

  where $E^1_{em,30^\circ}$ ($E^2_{em,30^\circ}$) is the electromagnetic energy inside a 30 degree cone around the leading charged track in hemisphere 1 (2). Thus a beam energy (i.e. 45 GeV) electron pair would have a radial momentum of $\sqrt{2}\times 45$ GeV$\simeq$ 63.6 GeV.

These two cuts on $p_{rad}$and $E_{rad}$are cuts mostly to remove events with obvious reconstruction problems. These two variables are also used in the $\mu\tau$ and $e\tau$ analyses themselves, as the signal is clearly different from the background both from tau pairs and from muon (electron) pairs in the p_{rad} (E_{rad}) distributions for the $\mu\tau$ ($e\tau$) signal events; see figures 5.7 and 5.8.

- Minimum visible energy: 8 GeV

  The variable "visible energy" is calculated as a sum over momenta for all the tracks plus the unassociated electromagnetic energy in the event.

This cut is introduced with the intention of removing events not originating from real e^+e^- collisions, but rather from unphysical events like beam gas events, beam wall events

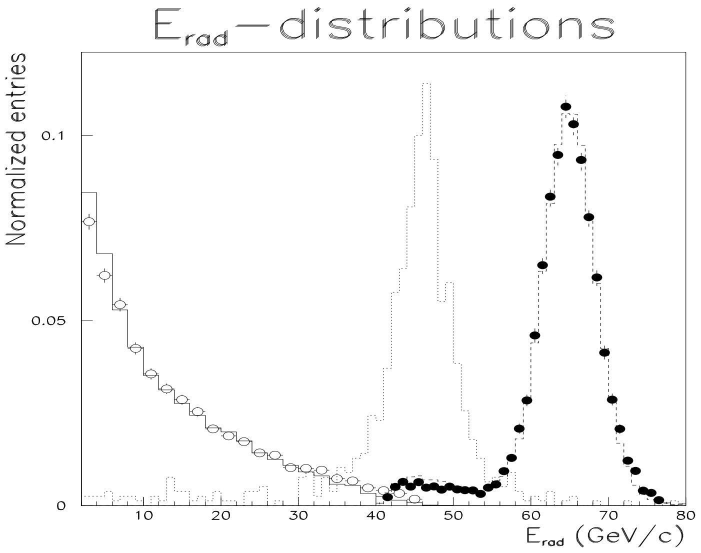

Figure 5.8: Radial electromagnetic energy distribitions. Solid histogram is Monte Carlo tau pairs, open circles are tagged tau pairs in data. The dashed histogram is Monte Carlo electron pairs, black dots are tagged electron pairs in data. The dotted histogram in the center is the Monte Carlo generated $e\tau$ signal.

and cosmics. In addition to this, the cut will remove some of the $Z^0 \rightarrow \tau^+\tau^-$ events, that is those events where the neutrinos from the decaying τs, the $\overline{\nu_\tau}$ from the τ^+ and the ν_τ from the τ^- (and possibly one or two more neutrinos if one or both of the taus decay hadronically), have very large momenta, transporting most of the energy from the reaction away undetected. These $Z^0 \rightarrow \tau^+\tau^-$ events will in any case be clearly different from the signal in all three analyses, since we in each analysis require at least one high energy particle, having energy above 0.3 times the beam energy. Thus the removal of this background should not affect the results. The cut will also remove real $e^+e^- \rightarrow Z^0$ events where the decay products go in the very forward direction or in cracks, thus depositing very little energy in the detector, but also these events will be unusable in the analyses.

- Minimum isolation angle: 160°

  The isolation angle is defined as the smallest angle between any two tracks in different hemispheres.

This cut is, together with the cuts on tracks and prongs, the primary cut against hadronic events, as leptonic events are generally consentrated in tighter jets (where the jets often consists of only one particle), whereas the hadronic jets are much more spread, that is they cover a wider angle. Thus the isolation angle tends to be further away from 180°, which is the angle for totally back-to-back events.

5.3.2 Detector quality cuts

In a search for rare of absent processes, one is sensitive to detector malfunctions, which may lead to anomalies and events not looking like what one would expect from the Standard

Model. For this reason, strict detector quality cuts were made on the most important subdetectors for each analysis, where both the subdetectors and the detector quality cut values were different in the three analyses.

The detector quality value is a number ranging from 0 to 9, where each subdetector gets assigned one detector quality value for each run and fill. The 10 different values have the following meaning:

0 Unusable data

1 Less than 50% of the detector is nominal

2 50–65% of the detector is nominal

3 65–80% of the detector is nominal

4 80–90% of the detector is nominal

5 90–95% of the detector is nominal

6 95–99% of the detector is nominal

7 More than 99% of the detector is nominal

8 Detector efficiency varies during run

9 Status of detector is unknown

Since the three analysis all were performed only in the barrel part of DELPHI, the detector quality cuts only depended on the quality of the barrel subdetectors.

The $\mu\tau$ analysis

The detector quality cuts for the $\mu\tau$ analysis were the following:

- The status of the HCAL, S_{HAB}, was required to be $4 \leq S_{HAB} \leq 7$
- The status of the MUB, S_{MUB}, was required to be $5 \leq S_{MUB} \leq 7$

The $e\tau$ analysis

The detector quality cuts for the $e\tau$ analysis were the following:

- The status of the HCAL, S_{HAB}, was required to be $4 \leq S_{HAB} \leq 7$
- The status of the MUB, S_{MUB}, was required to be $5 \leq S_{MUB} \leq 7$
- The status of the HPC was required to be 7.

The $e\mu$ analysis

The detector quality cuts for the $\mu\tau$ analysis were the following:

- The status of the HCAL, S_{HAB}, was required to be $5 \leq S_{HAB} \leq 7$
- The status of the MUB, S_{MUB}, was required to be $5 \leq S_{MUB} \leq 7$
- The status of the TPC, S_{TPC}, was required to be $5 \leq S_{TPC} \leq 7$

5.3.3 Cuts on polar angle

Only the barrel part of the DELPHI detector was used in all three analyses, which was transformed into a cut on the polar angle θ, with the requirement that the leading charged track in both hemispheres should be inside the cut, that is

$$\theta_{min} \overset{!}{\leq} \theta_{1(2)} \overset{!}{\leq} \theta_{max}$$

where $\theta_{1(2)}$ is the polar angle of the leading charged track in hemisphere 1(2), and θ_{min} and θ_{max} are two values fulfilling the simple relation

$$\theta_{min} + \theta_{max} = 180^\circ$$

giving a polar angle acceptance for the analyses symmetric about 90°. For the $e\tau$ and $e\mu$ analyses, the values of θ_{min} and θ_{max} were 45° and 135°, respectively, yielding the normal barrel definition of DELPHI. In the $\mu\tau$ analysis, good muon chamber coverage is absolutely essential (more so than in the $e\mu$ analysis, since there is no specific muon veto in the hemisphere opposite of the muon in this analysis), and the values of θ_{min} and θ_{max} were therefore determined from the polar angle coverage of the MUB, which is 52° and 128°, respectively.

5.3.4 Cuts to reduce remaining cosmic events

The cuts to reduce cosmics described in the leptonic preselection cuts, are all rather loose, and only intended as a first step in this procedure. Since the three analyses are sensible to contamination from cosmic to a different degree, each analysis has its own set of cuts to reduce cosmic events furter.

The $\mu\tau$ and $e\tau$ analyses

Due to the fact that both the $\mu\tau$ analysis and the $e\tau$ analysis search for a τ lepton (which may be a low energy track due to energy loss from the ν_τ in the subsequent decay of the τ) in addition to a high energy electron of muon, these two analyses are more sensitive to cosmic background than the $e\mu$ analysis. Therefore, the cuts to reduce cosmics for the two analyses were chosen to be the same:

- Maximum impact parameter in the R direction for the leading charged track in both hemispheres: 1 cm
- Maximum impact parameter in the z direction for the leading charged track in both hemispheres: 4 cm
- The maximum absolute value of the difference between impact parameters in the z direction for the leading charged track in both hemispheres: 1 cm

The $e\mu$ analysis

Since, as already mentioned, this analysis is not as sensitive to cosmic bacground (searching for two high energy particles), no further cuts to reduce cosmics were introduced.

5.3.5 Number of Z^0; total and effective

The number of Z^0 which have been subject to a specific analysis, $N_{Z^0}^{ij}$ for the general "i lepton j lepton" analysis, is found from the following equation:

$$N_{Z^0}^{ij} = \sum_{y=1991}^{1994} N_{Z^0}^{ij,y} \qquad \text{where} \qquad N_{Z^0}^{ij,y} \stackrel{\text{def}}{=} \sum_{i_y=1}^{n_y} \left(\frac{\mathcal{L}^{ij,i_y} \cdot \sigma_h^{i_y}}{B_h} \right) \tag{5.1}$$

The sum is then a sum over the four years 1991–1994 and over the LEP energy points, i.e. the centre of mass energy of the two beams. Here $\mathcal{L}^{ij,i_y}$ denotes the integrated luminosity of energy point i_y in year y for the ij analysis, while $\sigma_h^{i_y}$ denotes the hadronic cross section, that is, the cross section $\sigma_{Z^0 \to q_i \overline{q_i}}$, of energy point i_y in year y, which is independent of the analyses. The constant factor B_h denotes the branching fraction of $Z^0 \to q_i \overline{q_i}$, which is equal to the fraction of the hadronic width to the total width, that is:

$$B_h = \frac{\Gamma_{Z^0 \to q_i \overline{q_i}}}{\Gamma_{Z^0 \to X}}$$

The hadronic cross sections, $\sigma_h^{i_y}$, were generated with the ZFITTER [26] program, whereas the hadronic branching ratio, B_h, was found in the Review of Particle Properties (or the Particle Data Book), reference [31]. The energies and coresponding luminosities and hadronic branching fractions are summarized in table 5.1. Note that since LEP in 1991 and 1993 was operated in a "scanning" mode around the Z^0 peak, there are several entries in the table for these two years, while LEP in 1992 and 1994 was run in an "on peak" mode, for which reason only one entry is presented in the table for these two years.

As is apparent, the luminosity numbers in table 5.1 differ between different analyses. This is due to the fact that the three analyses use different detector quality cuts, thus making three different data samples with different corresponding luminosities. The luminosities and detector quality values were all found in the references [32] and [33].

The effective number of Z^0 for the general ij analysis, ξ^{ij}, is defined as the sum over the four years of data taking of the efficiency of the analysis on the LFV signal in question times the total number of Z^0 for that year, that is

$$\xi^{ij} = \sum_{y=1991}^{1994} \left(\varepsilon_i^{ij} \cdot N_{Z^0}^{ij,y} \right) \tag{5.2}$$

and $N_{Z^0}^{ij,y}$ as previously defined in equation 5.1. The factor ξ^{ij} is the sensitivity factor of the statistical method used to determine 95% CL limits on the branching ratios of the three LFV Z^0 decays; this will be furter discussed in chapter 6.1, where also uncertainties of the sensitivity factor ξ^{ij}, both statistical and systematic, will be treated.

5.3.6 Efficiencies

The efficiency of the analyses was determined as the product of 4 factors, where the three first are pure efficiencies, whereas the last factor is the product of an efficiency and a correction factor. These 4 factors are, for the general "i lepton j lepton" analysis, where $i, j = e, \mu, \tau$:

- The preselection efficiency, ε_{pre}^{ij}

Year	Energy (GeV)	Integrated luminosity (nb^{-1})			σ_h(nb)	σ_l(nb)	σ_e(nb)
		$\mu\tau$	$e\tau$	$e\mu$			
1991	88.466	639.279	636.973	639.279	5.155	0.264	0.538
	89.439	571.804	505.098	549.165	9.964	0.497	0.725
	90.214	651.038	559.771	593.216	18.008	0.887	0.995
	91.230	6015.318	5060.861	5233.300	30.303	1.483	1.270
	91.953	638.154	631.665	625.033	24.884	1.220	1.000
	92.952	536.625	516.190	550.181	14.302	0.706	0.603
	93.701	584.981	572.452	580.675	9.926	0.494	0.444
1992	91.346	22123.494	21275.061	21496.367	30.286	1.482	1.250
1993	89.485	8912.026	8882.425	8905.127	10.343	0.511	0.736
	91.249	9118.688	9108.017	9499.236	30.611	1.485	1.267
	91.364	4215.747	4124.591	4566.830	30.518	1.481	1.247
	93.076	9171.269	9093.230	9096.850	13.590	0.666	0.568
1994	91.268	39374.238	38610.480	40444.215	30.624	1.486	1.263

Table 5.1: Energy points for the 91–94 runs. The luminosities and hadronic and leptonic cross sections are listed for each energy point and for each analysis. σ_h denotes the hadronic cross section, σ_l denotes the common cross section for $Z^0 \to \mu\bar{\mu}$ and $Z^0 \to \tau\bar{\tau}$, whereas σ_e denotes the cross section for $Z^0 \to e\bar{e}$. This last cross section differs from σ_l because of the smaller polar angle range with which the Monte Carlo Bhabha samples were generated, and the contribution from the t-channel. See section 6.3.

This efficiency consists of the leptonic preselection cuts, detector quality cuts, cuts on polar angle θ to include only the barrel region, and the cuts to reduce cosmics, described in the previous subsections 5.3.1, 5.3.2, 5.3.3, and 5.3.4. These three last cuts are different for each of the three analyses, making the preselection efficiency slightly different for the three analyses. The preselection efficiency had to be determined from low statistics signal Monte Carlo.

- The efficiency of the i lepton selection routine, ε_i^{ij}
- The efficiency of the j lepton selection routine, ε_j^{ij}

These efficiencies one would ideally like to determine from data, which has been done. In doing this, one has to tag lepton pairs of all three types (e, μ and τ) in data by using cuts only in one hemisphere and on global variables, and then check the efficiency of the lepton selection routines on the other hemisphere. These tagging cuts for selection of lepton pairs are:

Muon pair tagging routine: Muon pairs were tagged by the following cuts.

— A muon found by the muon selection routine (this routine is different in the $\mu\tau$ and $e\mu$ analyses) in one of the hemispheres. In addition, this selected muon was required to be flagged *both* as a tight muon *and* a standard muon by the official muon tagging of DELPHI [36], and to have normalized momentum > 0.9.

— Acolinearity of the event was required to be $< 0.1^\circ$.

— The visible energy of the event was required to be $> 1.4 \cdot E_{beam}$.

With these cuts the total number of tagged muon pairs were 34384 in the $\mu\tau$ analysis, and 37342 in the $e\mu$ analysis.

Electron pair tagging routine: Electron pairs were tagged by the following cuts.

— An electron found by the electron selection routine (this routine is different in the $e\tau$ and $e\mu$ analyses) in one of the hemispheres. In addition, this selected electron was required to have normalized electromagnetic energy > 0.9.

— Acolinearity of the event was required to be $< 0.2°$.

— The visible energy of the event was required to be $> 1.4 \cdot E_{beam}$.

With these cuts the total number of tagged electron pairs were 51507 in the $e\tau$ analysis, and 61848 in the $e\mu$ analysis.

Tau pair tagging routine: Tau pairs were tagged by the following cuts.

— E_{rad} was required to be $< E_{beam}$.

— p_{rad} was required to be $< E_{beam}$.

If the event was a topology of a single track recoiling against a single track, additional cuts were added:

— Acolinearity of the event was required to be $> 0.5°$.

— Missing transverse momentum of the event was required to be > 0.4 GeV.

With these cuts the total number of tagged tau pairs were 110018 in the $\mu\tau$ analysis, and 128038 in the $e\tau$ analysis.

This procedure of tagging lepton pairs and determining the efficiency of the lepton selection routines, turns out to give a too high efficiency. The reason for this, is that lepton pairs, and in particular muon and electron pairs, tend to have a large degree of colinearity, that is a small acolinearity angle, typically less than 0.5°. When considering the geometry of the DELPHI detector, one notices that many of the sub-detectors are divided into an even number of modules in the azimuth direction (for instance the 24 modules of both the HPC and the HCAL, offset by 7.5° with respect to each other). This means that whenever a highly colinear event occurs, in particular leptonic pairs are created, the probability of one of the tracks hitting a dead or weak detector zone is highly correlated with the probability of the particle in the opposite hemisphere also hitting dead or weak areas in the detector. In the case of determining the lepton selection efficiency, this means that one will only be able to tag lepton pairs when one of the tracks are pointing to a zone in the detector with full sub-detector coverage, thus increasing the probability that the other track is in a correspondingly "good" area of the detector. The ε_i^{ij} and ε_j^{ij} factors should of course give the lepton selection routine efficiencies in the entire area determined by the cut on polar angle, and thus the described procedure gives too high an efficiency for the lepton selection routines.

The lepton selection efficiency for i leptons in the ij analysis (in general terms) is therefore corrected with a factor, C_i^{ij} (the same applies of course to the j lepton selection efficiency, with a corresponding factor C_j^{ij}). This factor is determined from large statistics samples of Monte Carlo simulated $Z^0 \to l_i\overline{l_i}$ (electron, muon and tau pair) events, and is motivated by the equation

$$\varepsilon_i^{ij} = \varepsilon_{i,tag}^{ij} \cdot \frac{\varepsilon_i^{ij}}{\varepsilon_{i,tag}^{ij}} = \varepsilon_{i,tag}^{ij} \cdot C_i^{ij} \tag{5.3}$$

Seeing that the only factor which can be determined from data, is the $\varepsilon_{i,tag}^{ij}$ factor, since one needs to tag i leptons in the data, the factor C_i^{ij} must be calculated from Monte Carlo simulations, where one can be certain as to what particles is present in the event without actually tagging them by using the detector. Thus the final form of equation 5.3 becomes

$$\varepsilon_i^{ij} = \varepsilon_{i,tag}^{ij,data} \cdot C_i^{ij} \qquad \text{where} \qquad C_i^{ij} \overset{\text{def}}{=} \frac{\varepsilon_i^{ij,MC}}{\varepsilon_{i,tag}^{ij,MC}} \tag{5.4}$$

and the superscripts *data* and *MC* refer to whether the efficiency is determined from data or Monte Carlo simulations.

This definition of the C_i^{ij} factor has the additional advantage that the factors determined from Monte Carlo simulations (the C_i^{ij} factor) only appear as fractions of two efficiencies, and not as absolute efficiencies. Thus one would expect the errors resulting from using Monte Carlo simulations instead of real data to be minimized.

- The both-hemisphere/correlation factor, ε_{both}^{ij}

This factor is, as already mentioned, a product of a pure efficiency (the both-hemisphere part) and a correction factor (the correlation factor). The both-hemisphere part is simply the efficiency of the cuts on global variables, that is variables not associated to a specific track in one of the hemispheres; this efficiency must be determined from low statistics signal Monte Carlo simulations, since the distributions of global variables in the lepton flavour number violating decays of the Z^0 in many cases are different from the distributions of the lepton flavour number conserving decays (electron, muon an tau pairs).

The correlation part is the factor which accounts for small correlating effects between the two identified i and j leptons in the two hemispheres, and is defined in the general ij analysis as

$$C_{corr}^{ij} = \frac{\varepsilon_{ij}^{ij}}{\varepsilon_i^{ij} \cdot \varepsilon_j^{ij}}$$

that is the efficiency of the analysis after the preselection cuts, but before the both-hemisphere cuts, divided by the product of the two lepton selection efficiencies. These correlation factors are for all three analyses rather small, typically less than 5% away from the value of 1, which is the value that indicates no correlation between the hemispheres. The total efficiency was then defined as the product of these 4 factors:

$$\varepsilon_{tot}^{ij} = \varepsilon_{pre}^{ij} \cdot \varepsilon_j^{ij} \cdot \varepsilon_i^{ij} \cdot \varepsilon_{both}^{ij}$$

Now follows the descriptions of the different cuts for the three analyses, with a number of corresponding figures. A few introductory comments about these different plots in the following three sections is needed. First, the plots illustrating a certain cut show distributions for candidates accepted by the analysis in question before the cut on the distribution shown is made. Thus the different distributions for specific background channels may vary considerably from what one would expect from the distribution in an unbiased sample of the same background; this may be particularly the case for the low statistics backgrounds, such as the muon and electron pair backgrounds. Secondly, all plots are normalized to 1, in order to see more easily the efficiency of the cuts applied. In doing so, the information of the relative sizes between the different different distributions is no longer appearent. The total number of events accepted by the three analyses, in the Monte Carlo case normalized to the data sample (treated in section 6.3), for each background channel is listed in table 7.2.

5.4 The $Z^0 \to \mu\tau$ analysis

5.4.1 The cuts for identifying muons

The cuts applied to select muons (the muon selection routine) were all, with the exception of the first cut, performed on the leading charged track in the hemisphere, and were:

- One charged track in the hemisphere

This cut is aimed at reducing some of the hadronic background, both from purely hadronic events (which should already be highly suppressed from the leptonic selection cuts) and from hadronic decays of one of the taus in a $Z^0 \to \tau^+\tau^-$ event. See figure 5.9.

- Normalized momentum between 0.3 and 1.3

The cut on normalized momentum was introduced to define the range of the likelihood method, as well as removing events with obvious reconstruction problems, or hard cosmics (the high edge).

- EHL in the range 0.01 mip<EHL<3.5 mip

This cut on the EHL (hadronic erergy per layer hit) is aimed at distinguishing muons from hadrons, where hadrons in general will have much larger energies deposited in the HCAL, and also tend to have this energy deposited in the layers first reached by a particle coming from the interaction point. Thus the EHL variable will in general be much larger for hadrons than for muons, see figure 5.10.

- More than 0.1 mip deposited in the last HCAL layer

- At least one MUB hit associated to the track

Given that muons have, at LEP energies, a better ability to traverse detector material than all other particles, they tend to a larger degree than other particles to have energy deposits in the last layer of the HCAL. Thus the first of these two cuts suppress in principle all backgrounds, but is particularly effective against electrons. The cut on MUB hit associated to the track makes use of the subdetector at LEP specifically designed for muon detection, the MUB. The cut is particularly effective against electrons, removing virtually *all* background from electrons, and a substantial part of the hadronic background as well (see figure 5.11).

As for electrons, these two cuts are extremely effective. When all other cuts in the analyses are applied except these two cuts, no electron candidates pass *any* of the two cuts. Thus the electron pais background is neglected for the $\mu\tau$ channel.

- The χ^2 of the track fit less than 5.

This cut was introduced in order to ensure good track reconstruction for particle to be recognized as a muon.

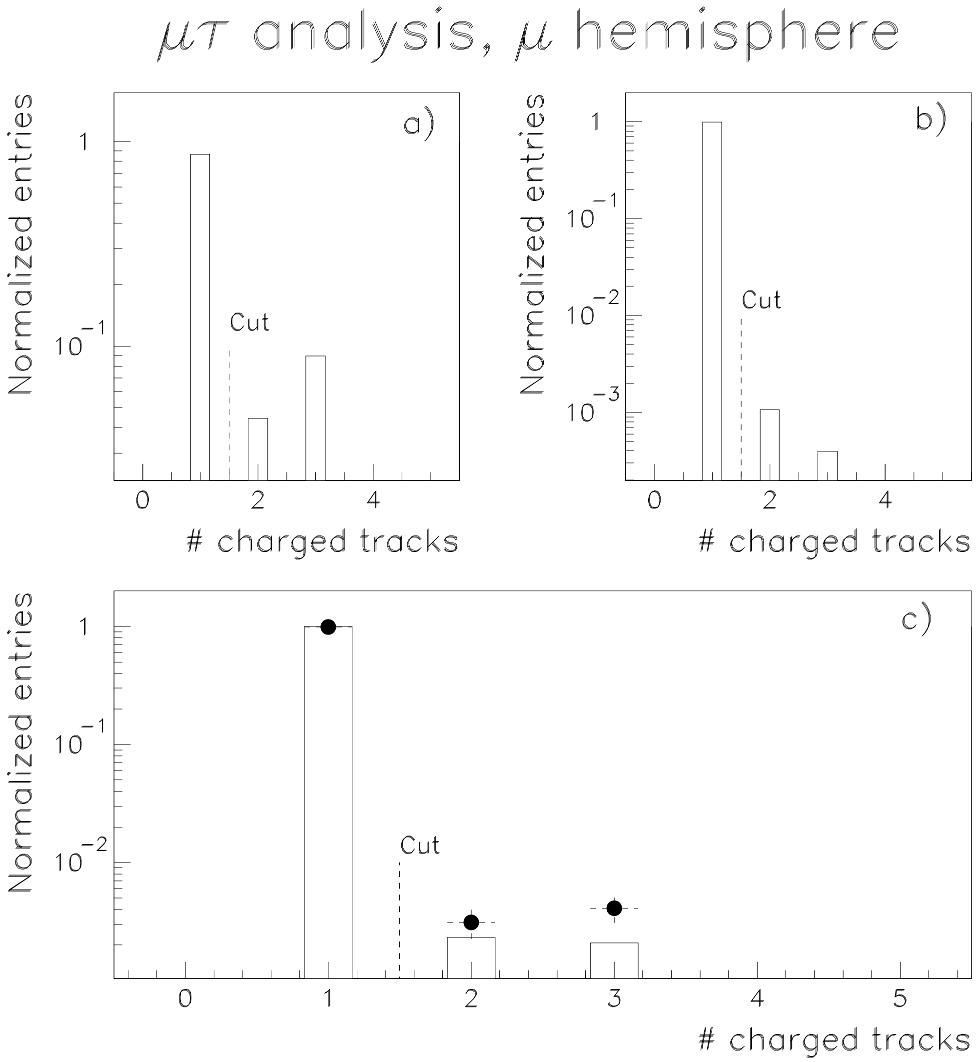

Figure 5.9: Plots showing the number of charged tracks in the muon hemisphere for $\mu\tau$ candidates. **a)** shows the distribution for hadronic decay products of a single tau in tau pair Monte Carlo events, **b)** shows the distribution for signal Monte Carlo, while **c)** shows the distribution for Monte Carlo total background candidate events in histogram, and data in black dots.

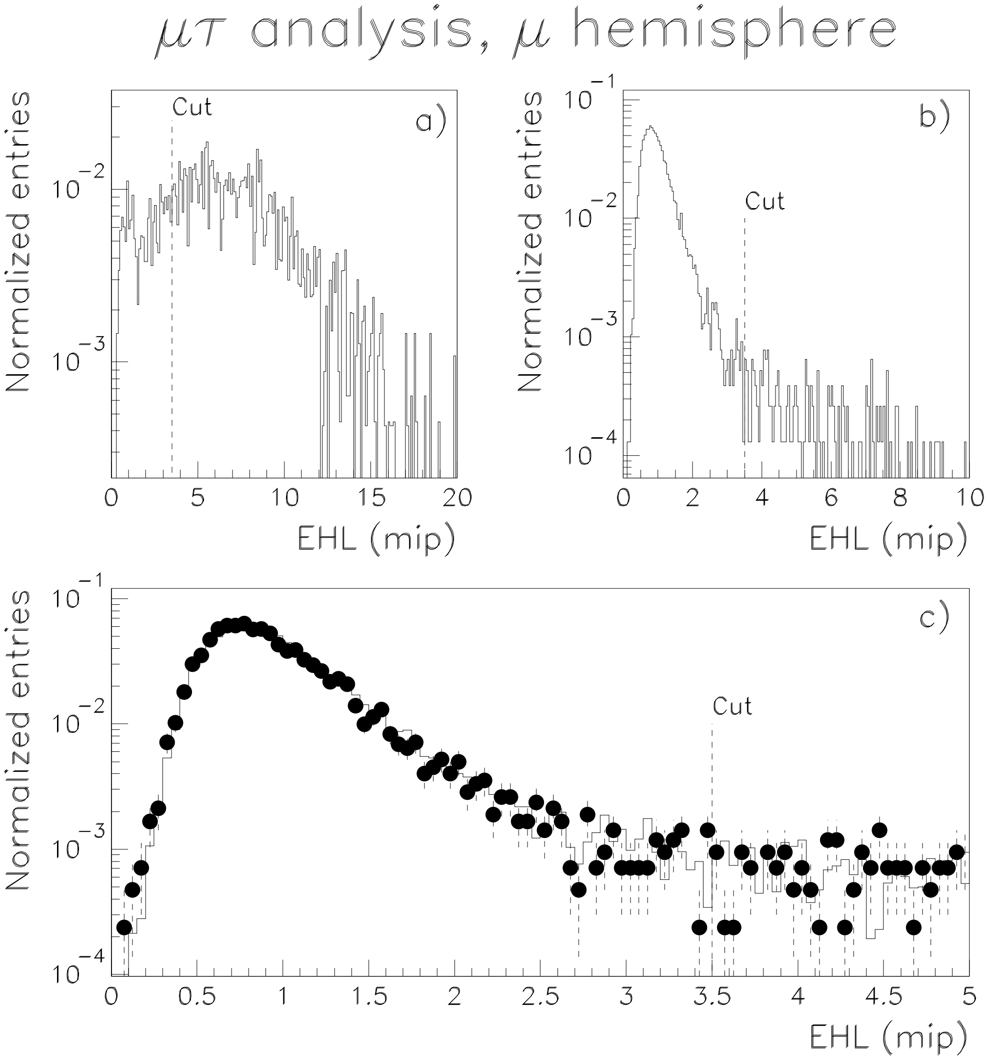

Figure 5.10: Plots showing the EHL (energy per HCAL layer hit) distribution for the leading charged track in the muon hemisphere in $\mu\tau$ candidate events. **a)** shows the distribution for hadronic decay products of a single tau in tau pair Monte Carlo events, **b)** shows the distribution for signal Monte Carlo, while **c)** shows the distribution for total Monte Carlo background in histogram, and data in black dots.

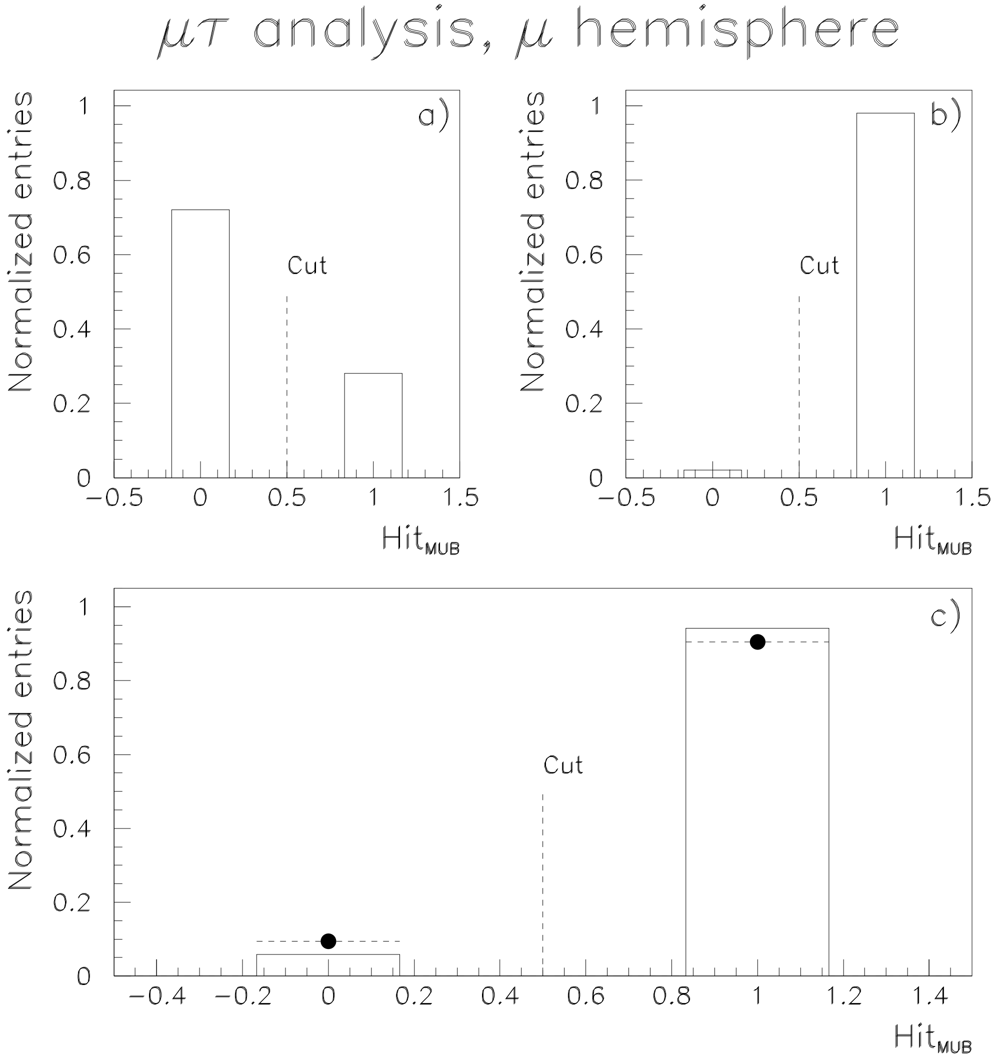

Figure 5.11: Plots showing the muchamber hits, where $\mathrm{Hit}_{MUB}=0$ denotes no MUB hit associated to the track, and $\mathrm{Hit}_{MUB}=1$ denotes at least one hit associated to the track, for the leading charged track in the muon hemisphere for candidates in the $\mu\tau$ analysis. **a)** shows the distribution for hadronic decay products of a single tau in tau pair Monte Carlo events, **b)** shows the distribution for signal Monte Carlo, while **c)** shows the distribution for total Monte Carlo background candidate events in histogram and data in black dots.

5.4.2 The cuts for identifying taus

These cuts aimed at selecting particles coming from a tau decay, with strong vetoes against muons, and were:

- A combined HCAL/HPC cut to suppress muons. This cut was divided into two parts:
  - If the leading charged track deposited energy in layers 2–4 of the HCAL, it was required to have hadronic energy response outside the mip peak, that is EHL<0.4 mip or EHL>2.0 mip.
  - If there was no hadronic energy in layers 2–4 for the leading charged track, and the track was in the mip peak (defined equally to the case with energy in layers 2–4), this could result from an electron leaking energy through to the HCAL. Thus, the track was required to be compatible with an electron, i.e. to have electromagnetic energy over momentum (E_{em}/p) in the expected electron range, $0.5 < E_{em}/p < 1.5$.

The cut thus aims at removing muons, while maintaining high efficiency for electrons, and also keeping hadronic events outside of the mip HCAL peak.

- Zero energy deposited in the last layer of the HCAL for the leading charged track.
- The leading charged track was required not to have hits in the MUB.

These two last cuts were aimed at removing muon pair background; See figures 5.12 and 5.13 for the signal efficiency and effectiveness against muon pairs for the first of these two cuts.

- Monentum larger than 2.5 GeV.
- The OD was required to have hits close to the track.

These two cuts were both performed on the leading charged track in the hemisphere, and ensured that the track was sufficiently detectable by the analysis. The first cut removes tracks that would not have the required energy to penetrate the HCAL all the way out to the MUB, thus automatically passing the requirement to have no MUB hit for the track (see figure 5.14). The cut on the OD assures good momentum resolution for the trach (see figure 5.1).

- Leading charged track $> 1.2^\circ$ (in θ) away from the crack at 90°.
- Leading charged track $> 0.5^\circ$ (in ϕ) away from the HCAL sector borders.

These two cuts are geometrical cuts which remove areas where the MUB coverage is weak or missing. The cut on θ relates to the area where there is a crack in DELPHI, at $z = 0$, whereas the cut on ϕ is intended to screen out the areas between the 24 HCAL modules in the ϕ direction. The reason for this is that there in these areas only are MUB coverage from the peripheral muon chambers; see the description of the MUB in subsection 3.4.5. Plots are shown in figure 5.15.

- All charged tracks for multiprong hemispheres were required to have hit in the VD.

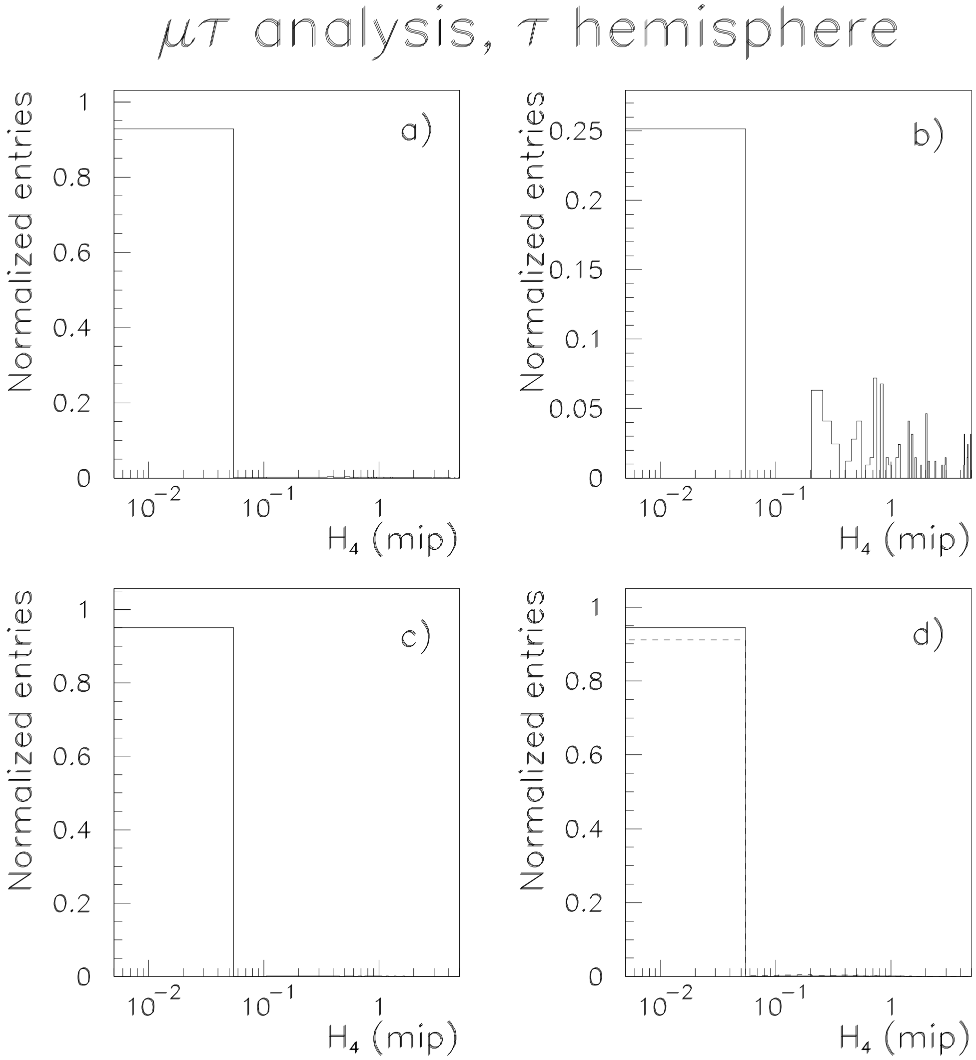

Figure 5.12: Plots showing the energy in the fourth layer of the HCAL for leading charged track in the tau hemisphere of $\mu\tau$ candidate events. The cut removes all but the first column of the histograms, thus yielding its value as the efficiency of the cut. **a)** shows the distribution for hadronic decay products of a single tau in tau pair Monte Carlo events, **b)** shows the distribution for muon pair Monte Carlo, **c)** shows the distribution for signal Monte Carlo, while **d)** shows the distribution for total Monte Carlo background candidate events in solid histogram and data in dashed histogram.

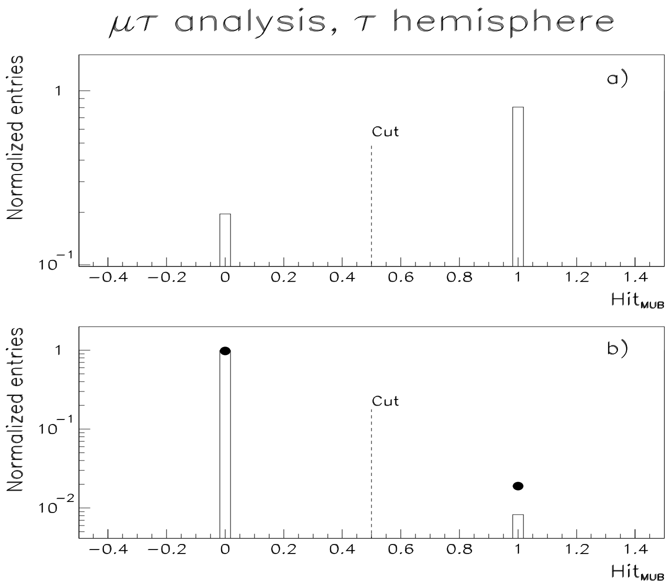

Figure 5.13: Plots showing MUB hit for the leading charged track in the tau hemisphere of $\mu\tau$ candidate events (The Hit_{MUB} variable as in figure 5.11). **a)** shows the distribution for the remaining muon pair background (Monte Carlo), while **b)** shows the background from tau pair Monte Carlo (similar to the signal) in histogram and data in black dots.

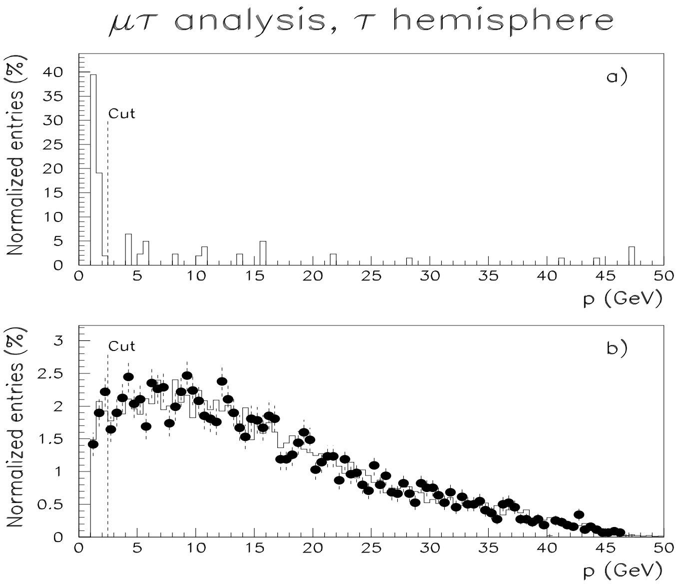

Figure 5.14: Plots showing the momentum distribution for the leading charged track in the tau hemisphere. **a)** shows the distribution for the remaining Monte Carlo muon pair background, while **b)** shows the background from tau pair Monte Carlo (similar to the signal) in histogram and data in black dots.

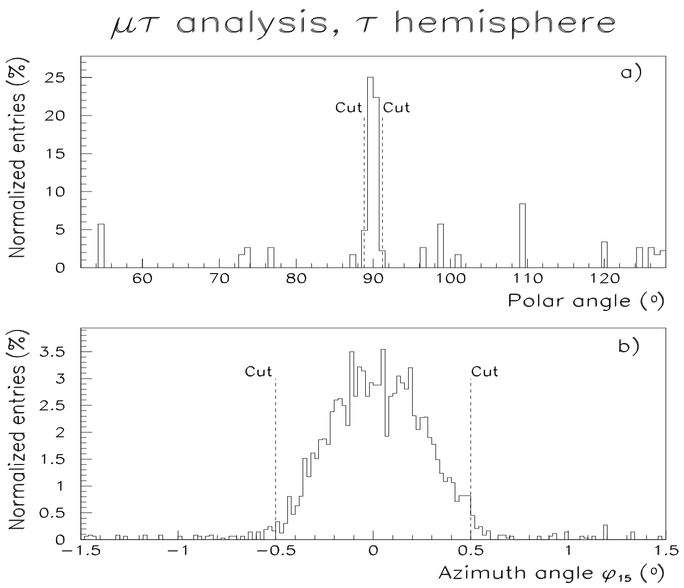

Figure 5.15: Plots showing the angular distribution for the leading charged track for Monte Carlo muon pair candidates in the $\mu\tau$ analysis. **a)** shows the θ distribution in the active area of the analysis (52°–128°), while **b)** shows the ϕ distribution, folded int one 15° sector (modulo 15°), where the HCAL sector borders are located at $\phi_{15} = 0$.

This cut was introduced to suppress muons radiating a hard photon (with a possible electron conversion, leading to a leading track that could easily pass the muon veto cuts in this hemisphere), by requiring that all charged tracks should be consistent with being created at the interaction point.

- If the leading charged track in the hemisphere deposited no HCAL energy, then electromagnetic energy in a 30° cone around the track was required to be > 0.5 GeV.

Noting that the muon is minimum ionizing, one would expect muons to be the particles depositing the least amount of energy in the calorimeters relative to their actual energy. Thus a good muon veto would be that the particle should deposit at least some energy in either the HCAL or the HPC. Since the HPC is situated inside the HCAL, it is natural to allow for zero hadronic energy (if the particle is stopped before it reaches the HCAL). See figures 5.16 and 5.17.

5.4.3 The cuts common to both hemispheres

The cuts on global variables in both hemispheres were:

- Different-sign leading charged tracks in the two hemispheres.

In simple topologies, one would expect to easily recognize the charge conservation inherent in a Z^0 decay in the leading charged particles in each hemisphere. Thus like-sign leading charged tracks would indicate anomalies, and should therefore be avoided; see figure 5.18.

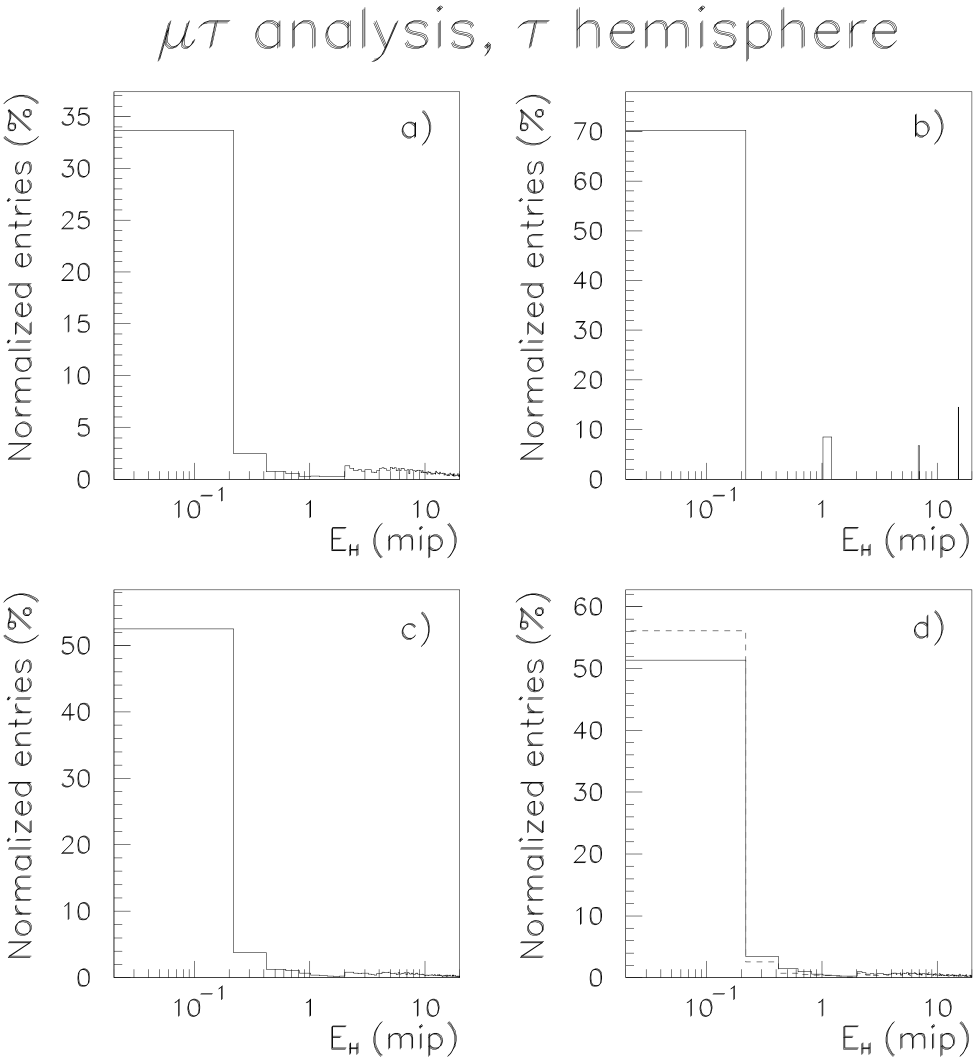

Figure 5.16: Plots showing the total hadronic energy deposit in the HCAL for the leading charged track in the tau hemisphere for the $\mu\tau$ analysis. Only the first column from E_H=0 to E_H=0.5 is affected by the cut, which sends those tracks with zero HCAL energy deposited on to the next cut, which recuires more than 0.5 GeV electromagnetic energy. **a)** shows the distribution for tau pair Monte Carlo where the tau in the tau hemisphere has decayed hadronically (i.e. events which should be recognized as candidates), **b)** shows the distribution for Monte Carlo muon pairs, **c)** shows the signal distribution (Monte Carlo), and **d)** shows the total Monte Carlo background in solid histogram and data as dotted histogram.

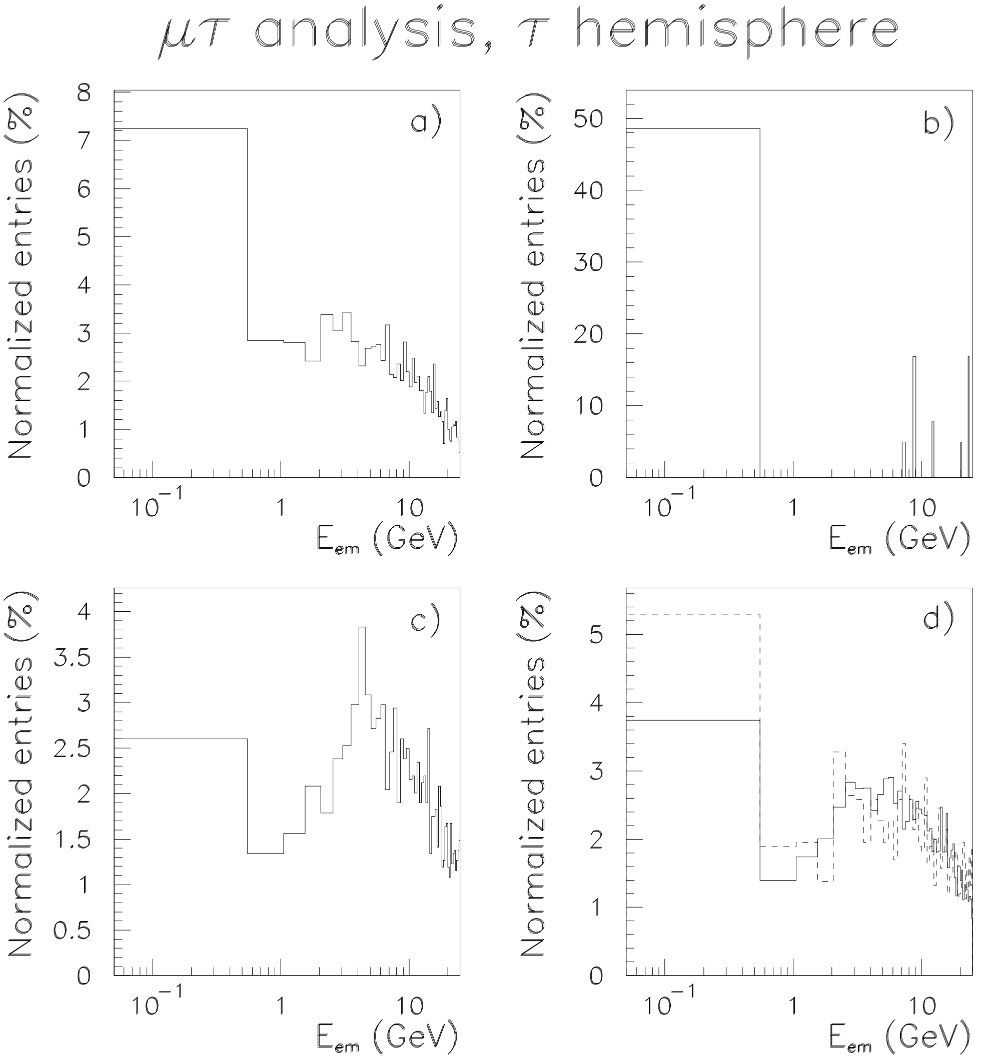

Figure 5.17: Plots showing the electromagnetic energy deposited in the HPC for leading charged tracks in the tau hemisphere for $\mu\tau$ candidate events with no hadronic energy deposit. Only the first column from E_{em}=0 to E_{em}=0.5 is removed by the cut, thus yielding the value of the first column as the fraction removed by the cut. **a)** shows the distribution for tau pair Monte Carlo where the tau in the tau hemisphere has decayed hadronically (i.e. events which should be recognized as candidates), **b)** shows the distribution for Monte Carlo muon pairs, **c)** shows the signal distribution (Monte Carlo), and **d)** shows the total Monte Carlo background in solid histogram and data as dotted histogram.

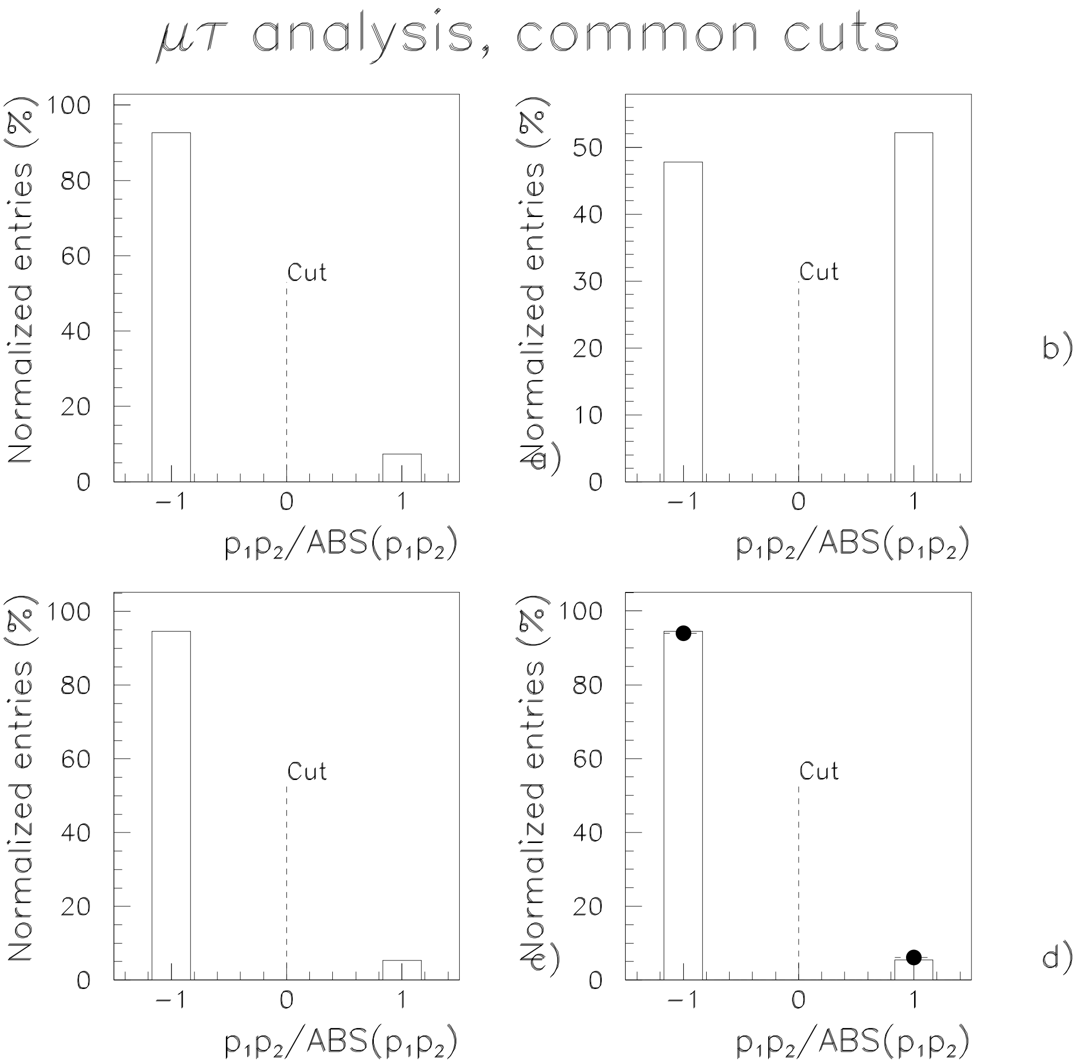

Figure 5.18: Plots illustrating the different-sign leading charged track cut in the $\mu\tau$ analysis; p_i denotes the charged momentum of the leading charged track in hemisphere i. **a)** shows the distribution for tau pair Monte Carlo where the tau in the tau hemisphere has decayed hadronically, **b)** shows the distribution for Monte Carlo muon pairs, **c)** shows the Monte Carlo signal distribution, and **d)** shows the total Monte Carlo background in solid histogram and data as dotted histogram.

- Acolinearity above 0.12°.
- Radial momentum $p_{rad}(\sqrt{p_1^2 + p_2^2})$ less than 62 GeV.

These two cuts are aimed at reducing the background from muon pairs, as these events generally are more high energetic (larger radial momentum) and display to a larger degree to be back-to-back events (lower acolinearity angle) than the $\mu\tau$ candidate events. Distributions for candidates are shown in figures 5.19 and 5.20.

5.5 The $Z^0 \to e\tau$ analysis

5.5.1 The cuts for identifying electrons

These cuts were performed on the leading charged track in the hemisphere, and were the following:

- Normalized electromagnetic energy between 0.3 and 1.3.

This cut defines the range for the likelihood method to be used. It also cuts away most of the background from muon pairs and also quite a lot of the the tau pair background where the tau decays hadronically. Distributions for candidates are shown in figure 5.21

- The electromagnetic energy divided by momentum (E_{em}/p) between 0.6 and 1.5.

This range of the variable defines the electron range with good efficiency. The cut removes much of the background from muons, and some of the background from hadronic tau decays; see figure 5.22.

- No hits in the MUB.
- Zero energy in hadron calorimeter layers 2–4.

Since electrons do not penetrate detector material very well, due to their low mass, one would not expect them to reach beyond the HPC. Thus these two cuts are designed to accept electrons but, at least to a larger degree, reject other, more penetrating particles, while at the same time allowing for some leakage into the first HCAL layer. These cuts are perticularly effective against muons; see figure 5.23.

After these initial cuts were performed, several cuts on the longitudinal pattern of the energy deposition and on $\mathrm{d}E/\mathrm{d}x$ in the HPC were imposed. This was done in order to suppress hadronic background from taus decaying hadronically, resulting mostly in pions in the HPC.

- Maximum fraction of the HPC energy in one layer < 0.35.
- The layer in the HPC with the most energy deposited was required not to be layers 8 or 9.
- If the number of wires hit in the TPC > 30, then the $\mathrm{d}E/\mathrm{d}x$ pull for pion hypothesis was required to be $P_{pi} > -1$.
- If the number of wires hit in the TPC > 30, then the $\mathrm{d}E/\mathrm{d}x$ pull for electron hypothesis was required to be $P_{el} > -2$.

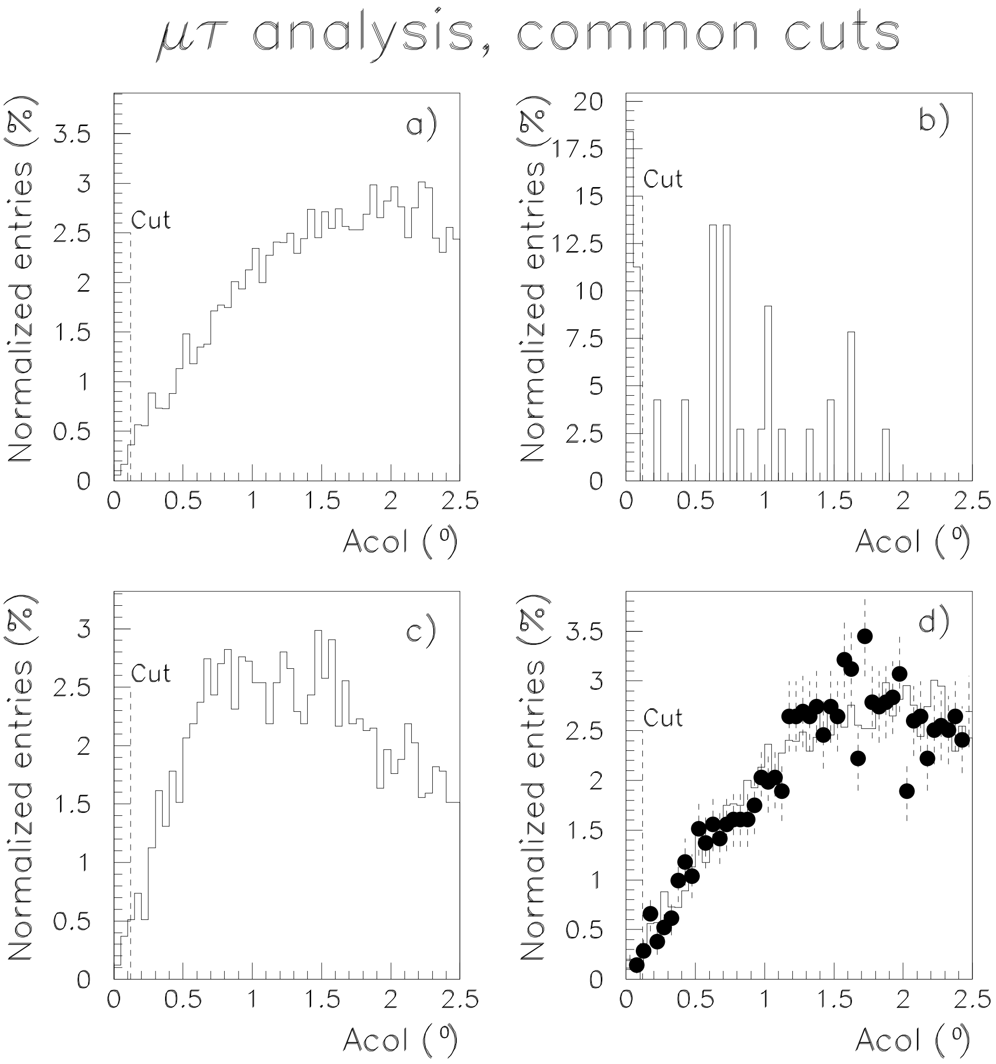

Figure 5.19: Acolinearity of candidate events in the $\mu\tau$ analysis. **a)** shows the distribution for tau pair Monte Carlo, **b)** shows the distribution for Monte Carlo generated muon pairs, **c)** shows the Monte Carlo signal distribution, and **d)** shows the total Monte Carlo background in histogram and data as points.

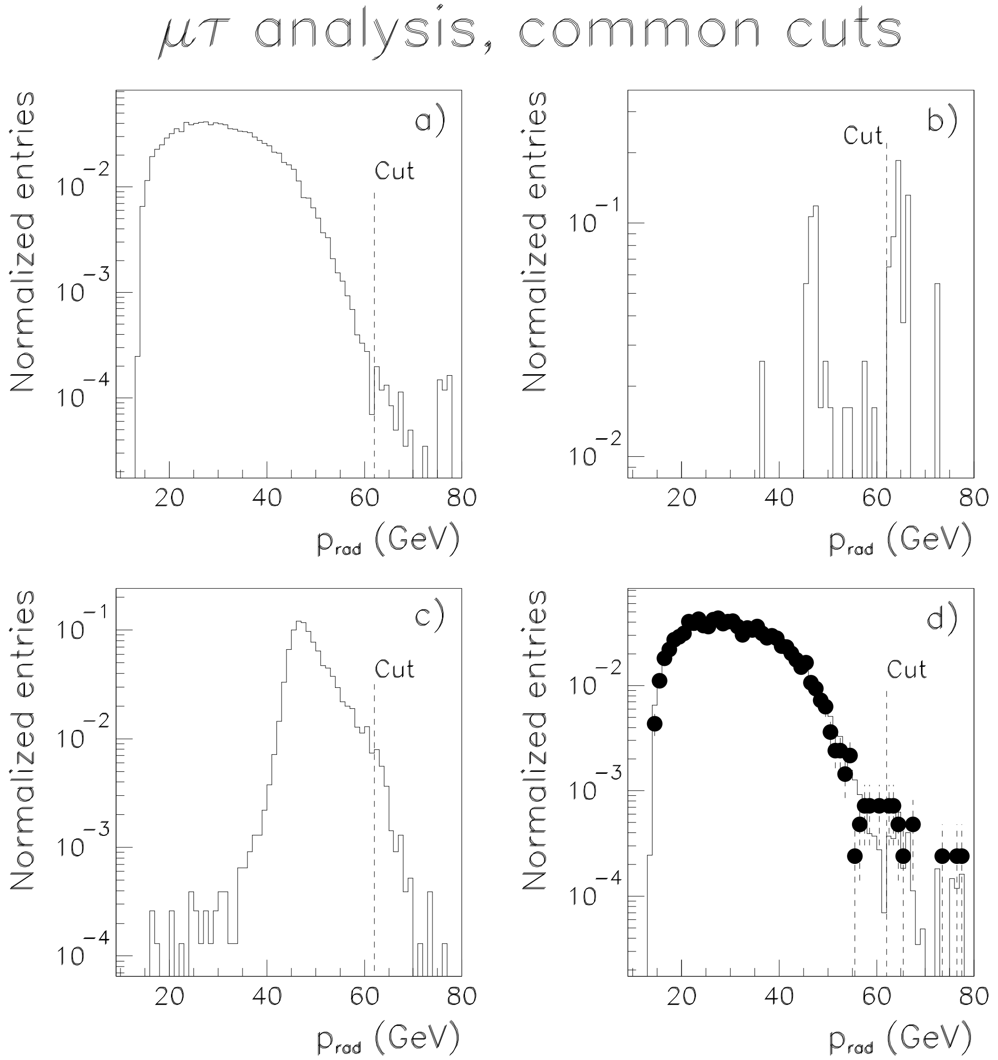

Figure 5.20: Radial momentum $p_{rad} = \sqrt{p_1 + p_2}$, where p_i denotes the momentum of the leading charged track in hemisphere i, of candidate events in the $\mu\tau$ analysis. **a)** shows the distribution for tau pair Monte Carlo, **b)** shows the distribution for Monte Carlo generated muon pairs, **c)** shows the Monte Carlo signal distribution, and **d)** shows the total Monte Carlo background in histogram and data as points.

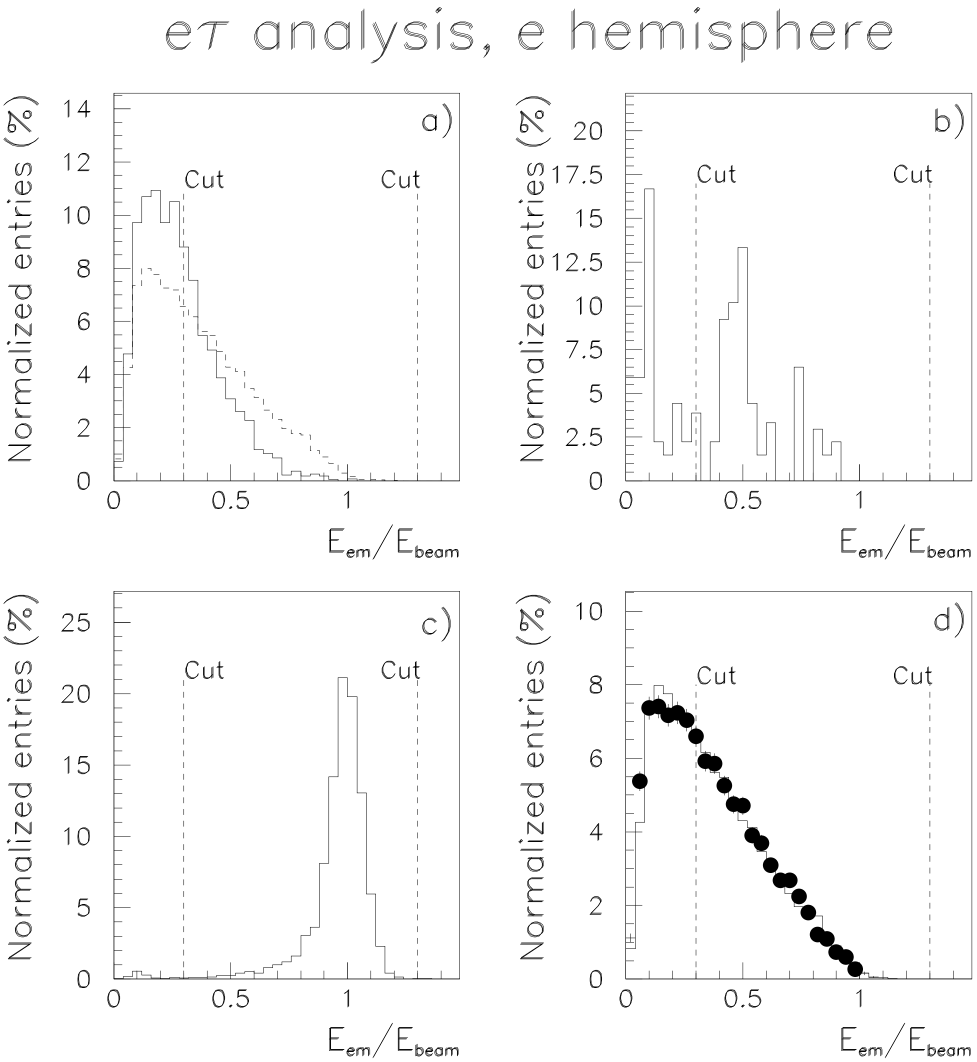

Figure 5.21: Electromagnetic energy for the leading charged track in the electron hemisphere of $e\tau$ candidate events. **a)** shows the distribution for Monte Carlo tau pairs, total distribution (in the solid histogram), and in the case where the tau in the electron arm decays hadronically (misidentified as an electron, dotted histogram). These two histograms are individually scaled, so the figure does *not* display the ratio between these two decay modes. **b)** shows the distribution for Monte Carlo generated muon pairs, **c)** shows the Monte Carlo signal distribution, and **d)** shows the total Monte Carlo background in histogram and data as points.

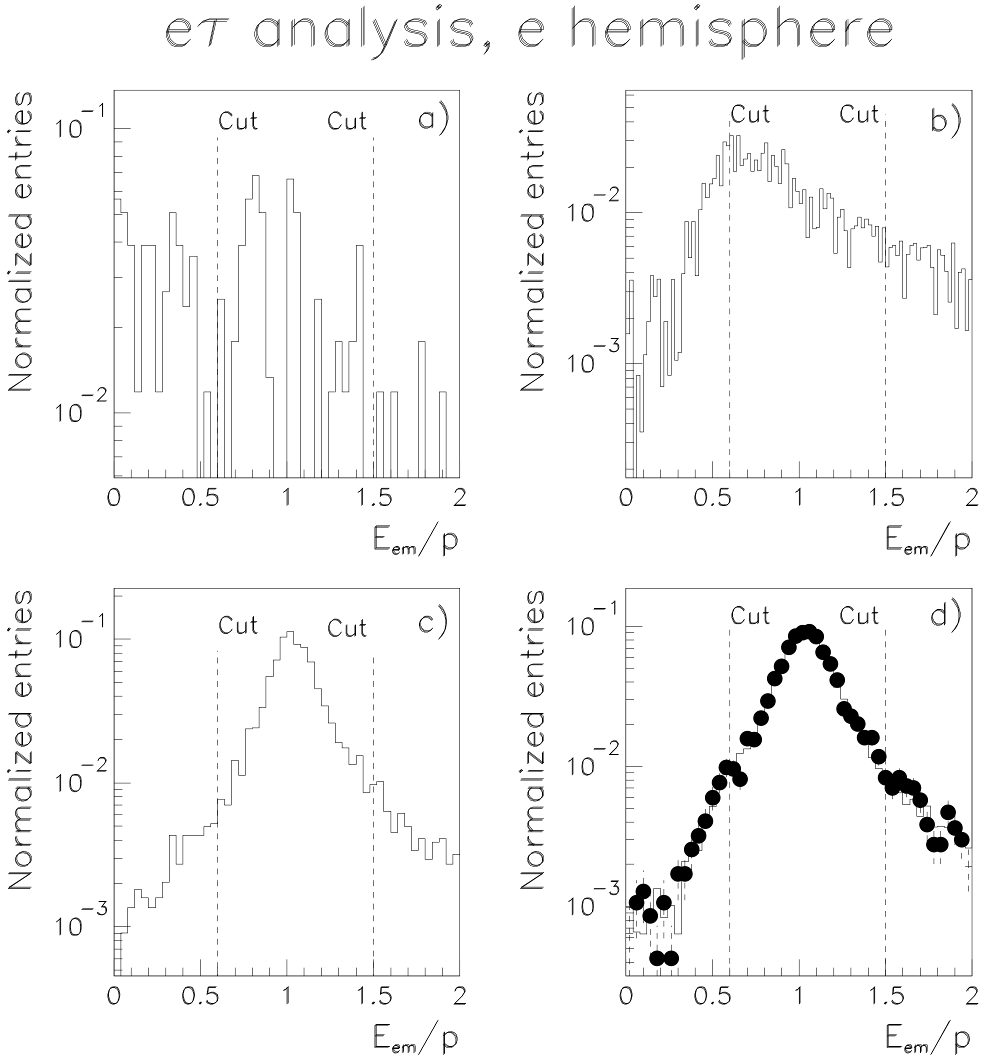

Figure 5.22: Electromagnetic energy over momentum for the leading charged track in the electron hemisphere of $e\tau$ candidate events. **a)** shows the distribution for Monte Carlo generated muon pairs, **b)** shows the distribution for Monte Carlo tau pairs where the tau in the electron arm decays hadronically (misidentified as an electron). **c)** shows the Monte Carlo signal distribution, and **d)** shows the total Monte Carlo background in histogram and data in points.

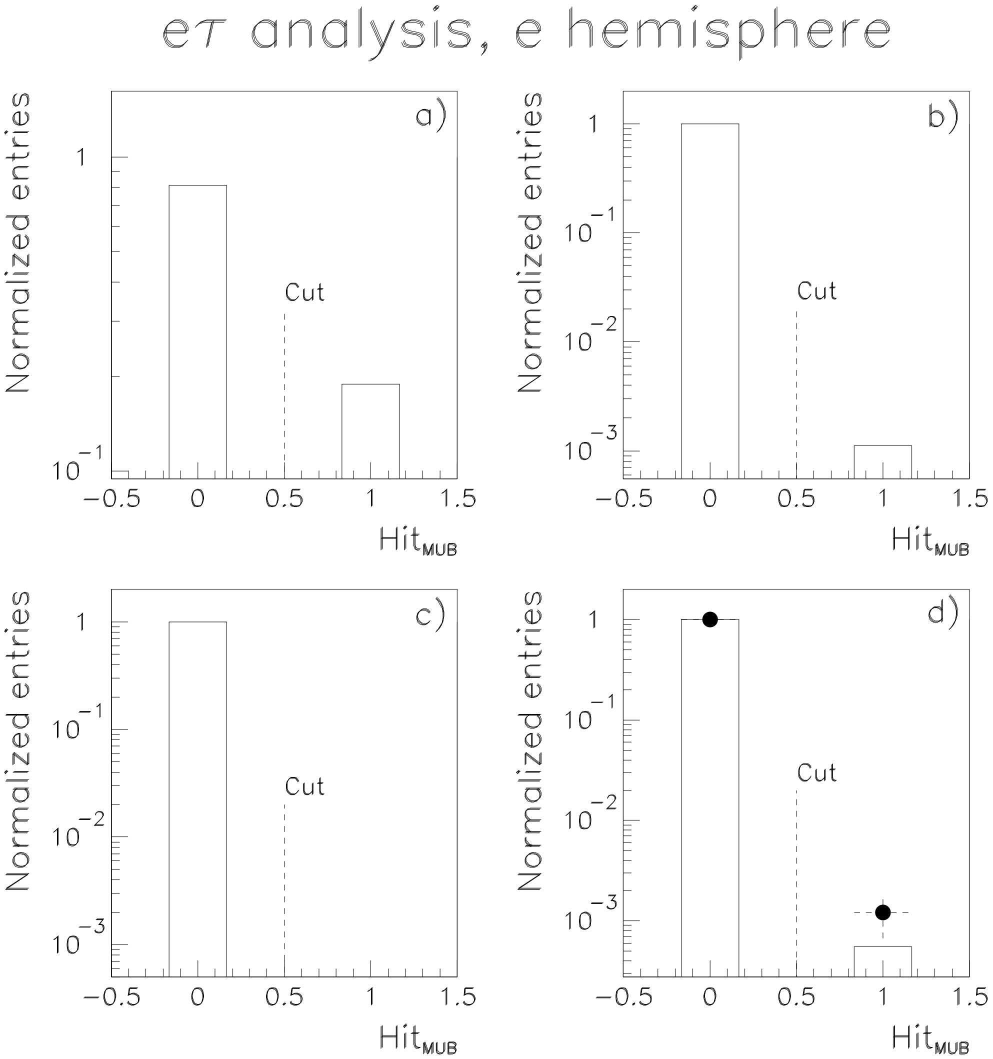

Figure 5.23: Muon chamber hits associated to the leading charged track in the electron hemisphere for $e\tau$ candidates. **a)** shows the distribution for Monte Carlo tau pairs where the tau in the electron arm decays hadronically (misidentified as an electron), **b)** shows the distribution for Monte Carlo generated muon pairs, **c)** shows the Monte Carlo signal distribution, and **d)** shows the total Monte Carlo background in histogram and data as points.

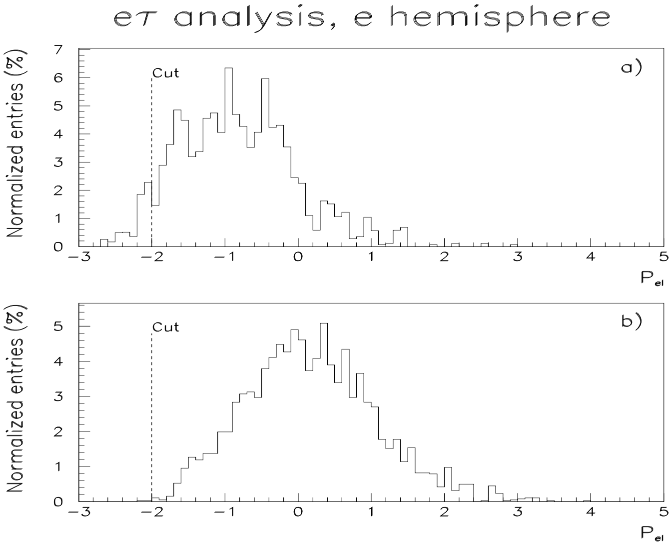

Figure 5.24: TPC dE/dx pull for electron hypothesis for the leading charged track in the electron hemisphere for $e\tau$ candidate events when the number of wires hit in the TPC is more 30. **a)** shows the distribution for Monte Carlo tau pairs where the tau in the electron arm decays hadronically (misidentified as an electron), and **b)** shows the distribution for the Monte Carlo generated signal.

For these last two cuts the pull value is defined as the measured value minus the expected value of the dE/dx (different for electron and pion hypothesis) divided by the error on the dE/dx measurement. These two cuts are highly correlated, and the distributions are therefore only shown for the electron hypothesis cut, in figure 5.24.

- The absolute value of the variable Δz (the difference between the z position of the extrapolated track and the z position of the HPC shower) < 1.5.

See figures 5.25, 5.26, and 5.27 for these distributions.

5.5.2 The cuts for identifying taus

The cuts applied to select taus, with strong vetoes against electrons, were all performed on the leading charged track in the hemisphere, and were:

- Track at least 3° away from the HPC crack at θ=90°.
- Track at least 1° (in ϕ) away from HPC sector borders.

These geometrical cuts were introduced to ensure good HPC coverage over the active detector area. This was done in order to ensure a good detection ability for electromagnetic energy, which is crucial in the electron veto. See figure 5.28.

- If the HCAL energy in layers 2–4 was greater than 2.5 mip, the event was now accepted as a tau. If not, the following cuts were applied:

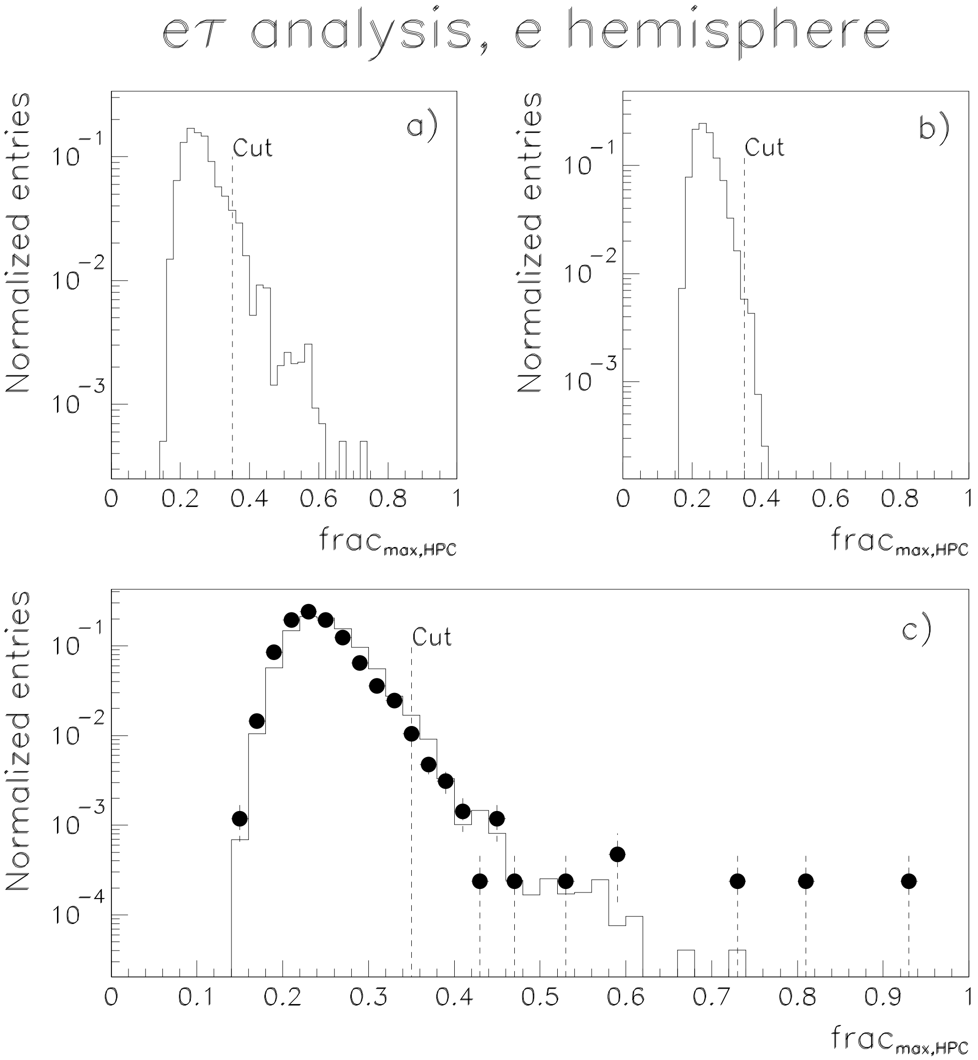

Figure 5.25: The energy of the layer with the largest energy deposit in the HPC divided by the total energy in the HPC for the leading charged track in the electron hemisphere for $e\tau$ candidate events. **a)** shows the distribution for Monte Carlo tau pairs where the tau in the electron arm decays hadronically (misidentified as an electron), **b)** shows the distribution for the Monte Carlo generated $e\tau$ signal, and **c)** shows the total Monte Carlo background in histogram and data as points.

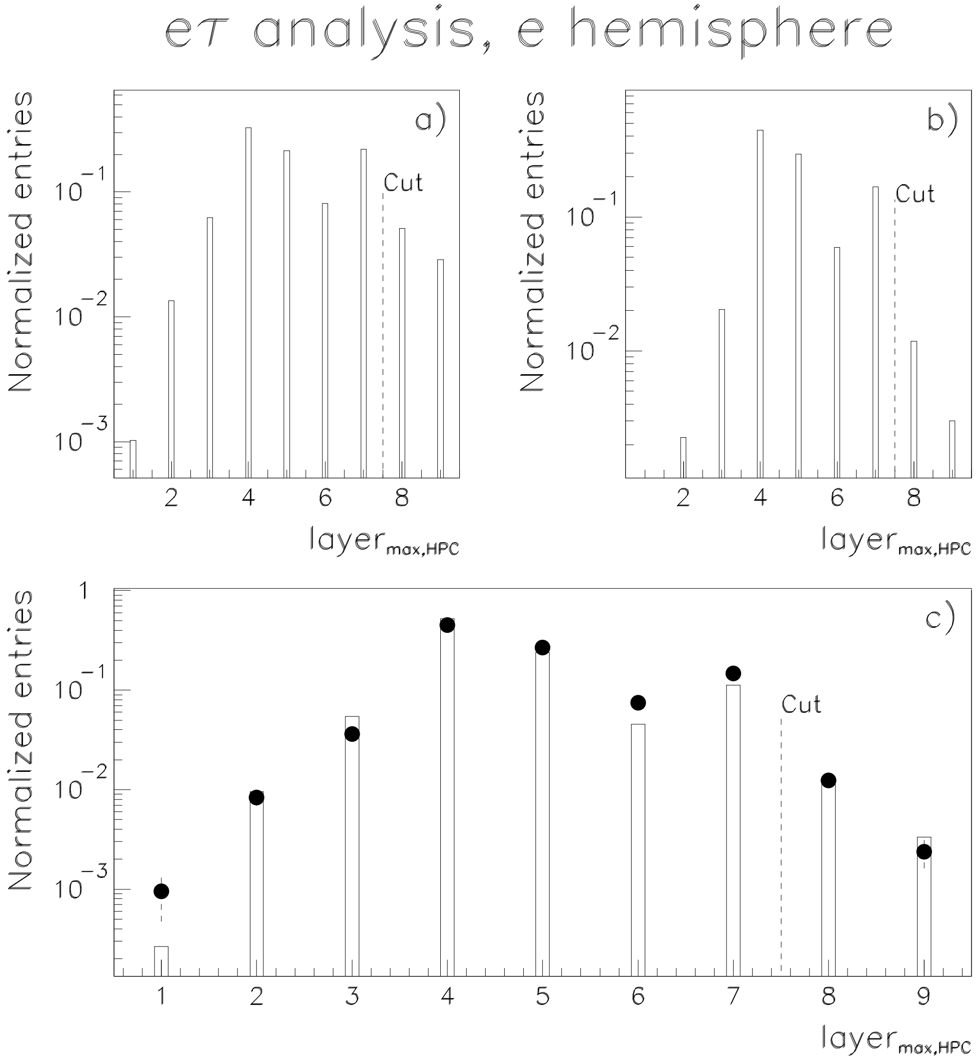

Figure 5.26: The layer with the largest energy deposit in the HPC for the leading charged track in the electron hemisphere for $e\tau$ candidat events. **a)** shows the distribution for Monte Carlo tau pairs where the tau in the electron arm decays hadronically (misidentified as an electron), **b)** shows the distribution for the Monte Carlo generated $e\tau$ signal, and **c)** shows the total Monte Carlo background in histogram and data as points.

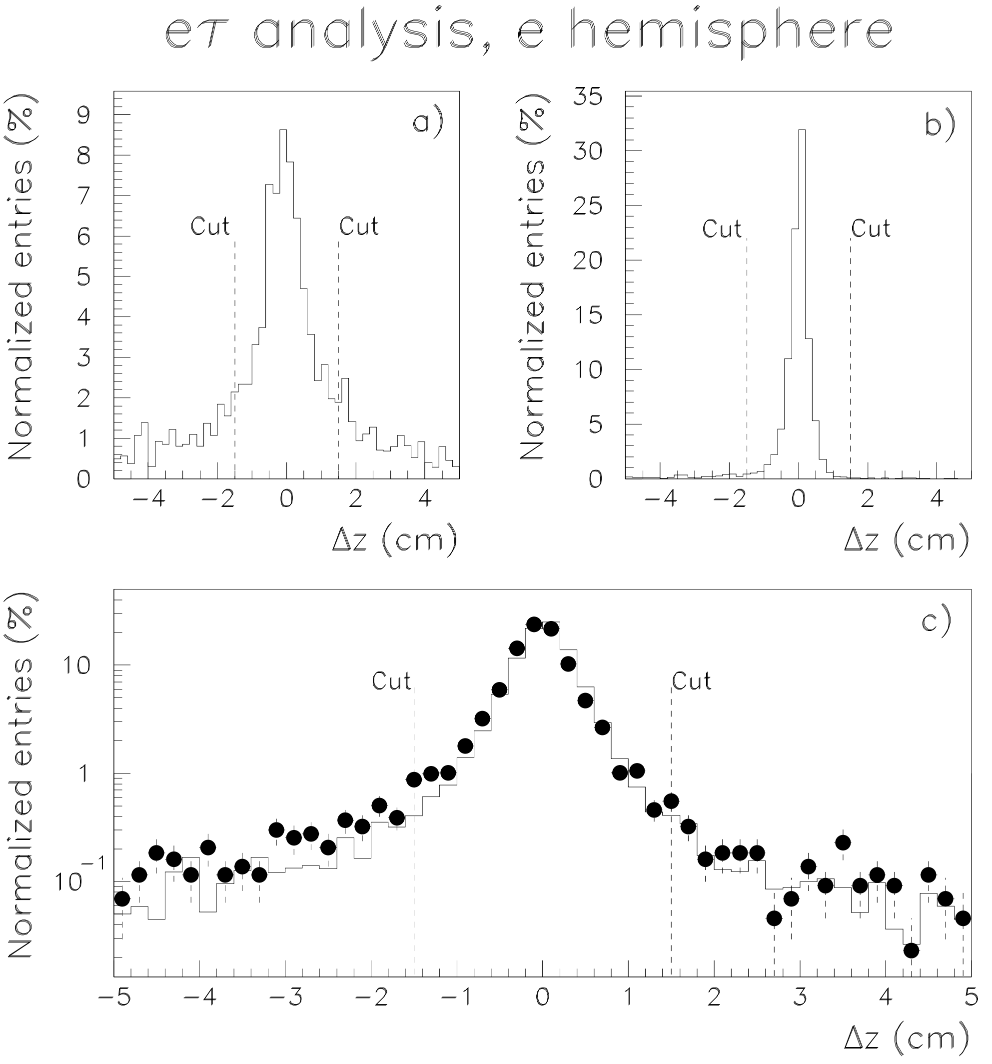

Figure 5.27: The variable Δz (the z value of the extrapolated track minus the z value of the shower in the HPC) for the leading charged track in the electron hemisphere for $e\tau$ candidate events. **a)** shows the distribution for Monte Carlo tau pairs where the tau in the electron arm decays hadronically (misidentified as an electron), **b)** shows the distribution for the Monte Carlo generated $e\tau$ signal, and **c)** shows the total Monte Carlo background in histogram and data as points.

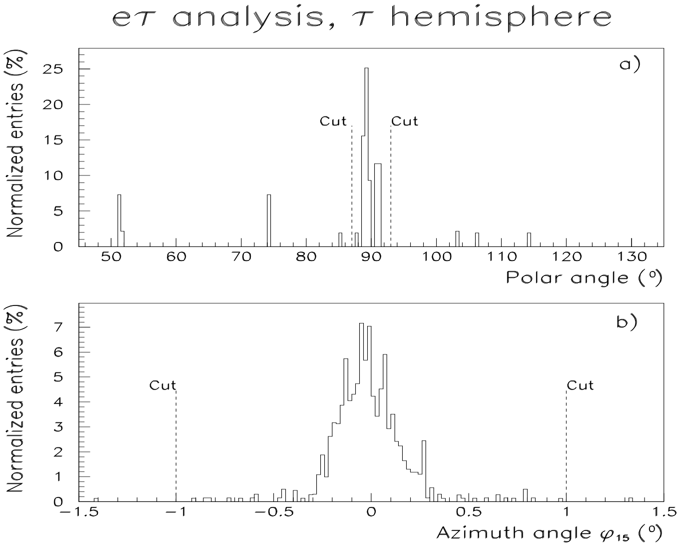

Figure 5.28: Plots showing the angular distribution for the leading charged track for Monte Carlo electron pair candidates in the $e\tau$ analysis. **a)** shows the θ distribution for the active area of the analysis (45°–135°), while **b)** shows the ϕ distribution, folded int one 15° sector (modulo 15°), where the HPC sector borders are located at $\phi_{15} = 0$ (15° offset with comparison to the HCAL sector borders).

- E_{em}/p required to be incompatible with electron response, < 0.45.
- The track was required not to be pointing towards an HPC module flagged as dead.

This last cut required the flagging of weak or dead HPC modules, which is important, since an HPC module not working properly, will make it easier for an electron to pass the electron veto cuts. Which modules that were flagged as dead, changed from year to year, as the HPC is checked and monitored constantly. The procedure for checking the HPC modules was the following: An electron was found in one hemisphere (by the electron selecion routine), and electromagnetic energy in the opposite hemisphere of this electron was required to be less than 1 MeV. In addition, the acolinearity of the event was required to be below 0.3°. When fulfilling these conditions, the HPC module of the track opposite the electron was recorded, thus making dead/weak modules stand out as peaks. The results can be seen in figure 5.29. With this procedure the modules flagged as dead were: 78, 89, and 114 for 1991, 89 for 1992, 78, 113, and 137 for 1993, and 78 for 1994.

- If the momentum of the track was in the range $0.2 < p(\mathrm{GeV/c}) < 8.0$ and the number of TPC dE/dx wires hit > 30, the dE/dx response was required to be inconsistent with the expected electron response (see figure 5.30. Outside this momentum range, the candidate was rejected if the energy in HCAL layers 2–4 was zero and the number of MUB hits associated to the track was zero.

5.5.3 The cuts common to both hemispheres

The cuts on global variables in both hemispheres were:

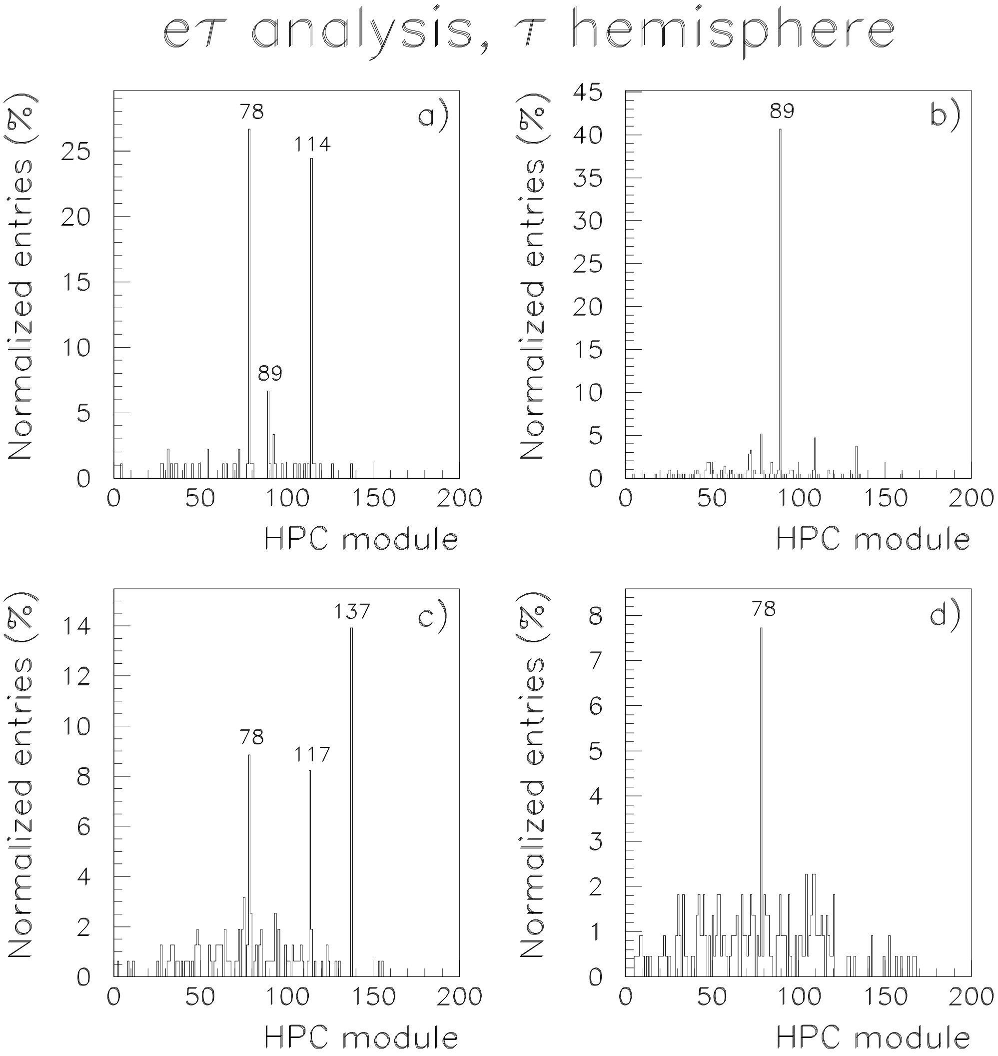

Figure 5.29: Plots showing the number of registered events with a high energy lepton in one hemisphere, low acolinearity and little or no HPC energy in the opposite hemisphere, as a function of the HPC module number of the track-extrapolation for the track with low electromagnetic energy. **a)** shows the 1991 sample, **b)** shows the 1992 sample, **c)** shows the 1993 sample, and **d)** shows the 1994 sample.

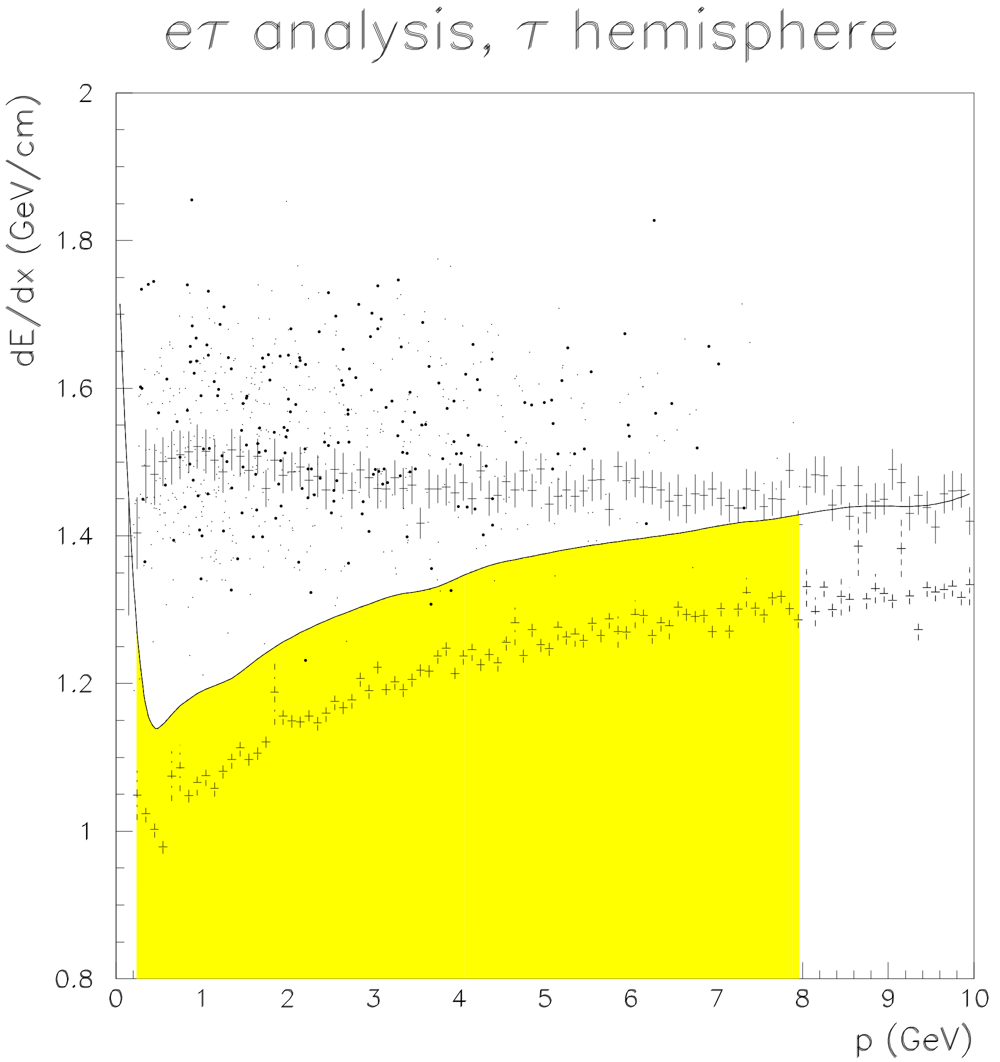

Figure 5.30: dE/dx versus momentum for the leading charged track in the tau hemisphere in the $e\tau$ analysis. The upper band of "crosses" show the expected response for electrons, whereas the lower show the expected response from non-electrons. The solid line shows the cut, where particles lying inside the shaded area are rejected. The lower band of "crosses" show the expected response for non-electrons. The points denote the leading charged track in candidate events from Monte Carlo background channels, where the smaller points denote accepted candidates before the cut from tau pairs where both taus have decayed to electrons, whereas the larger points show the candidates before the cut from electron pair Monte Carlo.

- Acolinearity above 0.3°.
- Radial electromagnetic energy $E_{rad} = (\sqrt{(E^1_{em})^2 + (E^2_{em})^2})$ less than 59 GeV.

These two cuts are both aimed at removing the electron pair background, which in general have higher energy (larger radial electromagnetic energy) and a larger degree of being back-to-back events (smaller acolinearity) than both the $e\tau$ signal and the tau pair background. The distributions are shown in figures 5.31 and 5.32.

5.6 The $Z^0 \to e\mu$ analysis

5.6.1 The cuts for identifying electrons

The cuts applied to select high momentum electrons were all performed on the leading charged track in the hemisphere (with the exception of the first cut), and were:

- One charged track in the hemisphere.
- Normalized electromagnetic energy between 0.3 and 1.3.
- Hadronic energy for the first layer of the HCAL less than 2.5 mip.

This cut allows for leakage through the HPC into the HCAL from electrons.

- Zero energy deposited in all other HCAL layers.
- No MUB hits associated to the track.
- Normalized momentum was required to be < 1.3.

These cuts contain essentially much of the same as the first 4 cuts in the electron selection routine in the $e\tau$ analysis. The difference is that there is no cut on E_{em}/p here (increasing the efficiency), but there is a rather loose cut on energy in the first layer of the HCAL introduced (loses a bit of efficiency), in addition to a cut on number of charged tracks in the hemisphere (also not a drastic cut on the efficiency), and an upper cut on momentum, in order to avoid badly reconstructed tracks. See figures 5.33, 5.34, and 5.35 for these new cuts.

5.6.2 The cuts for identifying muons

The cuts applied to select muons were all cuts on the leading charged particle in the hemisphere, and were as follows:

- One charged track in hemisphere.
- At least one MUB hit associated to the track.

Once more the cut requirement of at least one MUB hit associated to the track removes all electron pair Monte Carlo background, so this is neglected in the $e\mu$ analysis just as it was in the $\mu\tau$ analysis.

- Normalized momentum was required to be between 0.3 and 1.3.
- HCAL response in the expected muon range, that is 0.03 mip<EHL<3.9 mip.

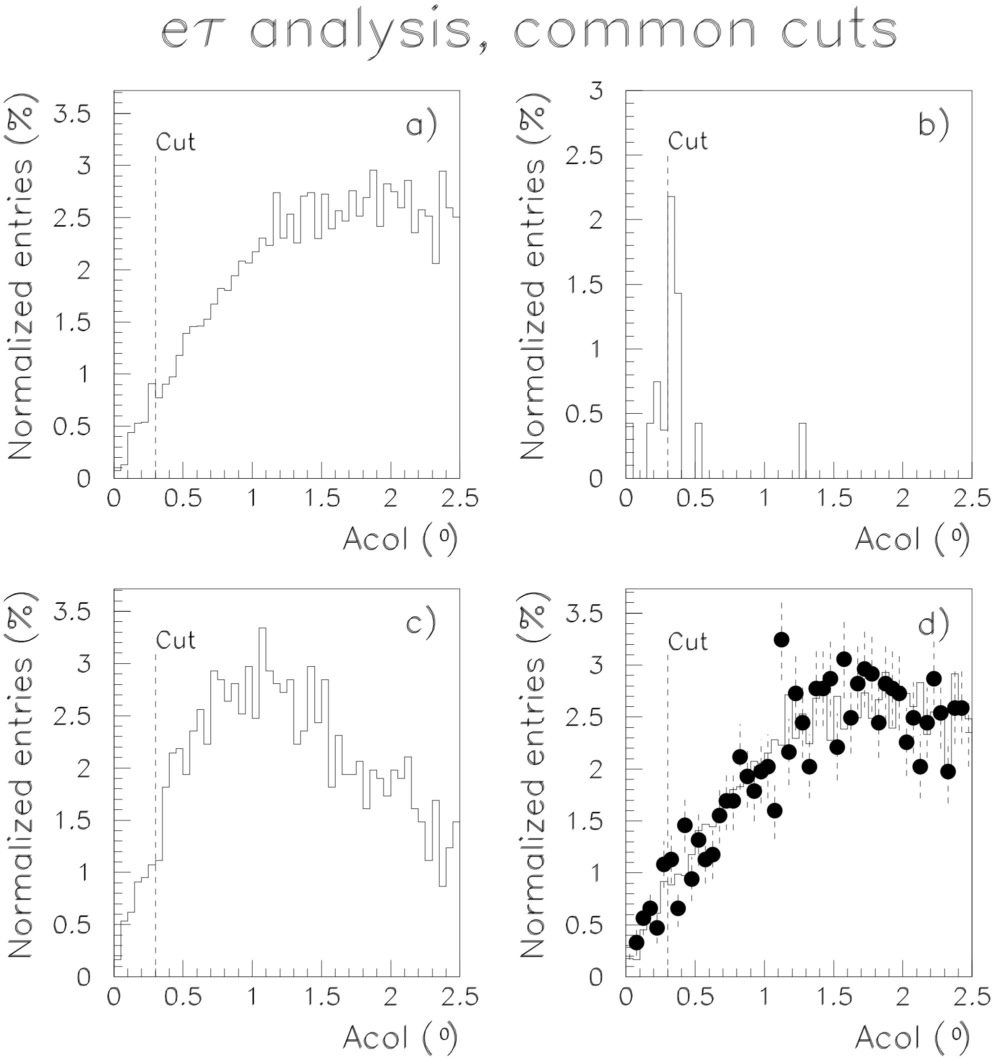

Figure 5.31: Acolinearity of the $e\tau$ candidate events. **a)** shows the distribution for Monte Carlo tau pairs **b)** shows the distribution for Monte Carlo generated electron pairs, **c)** shows the Monte Carlo signal distribution, and **d)** shows the total Monte Carlo background in histogram and data as points.

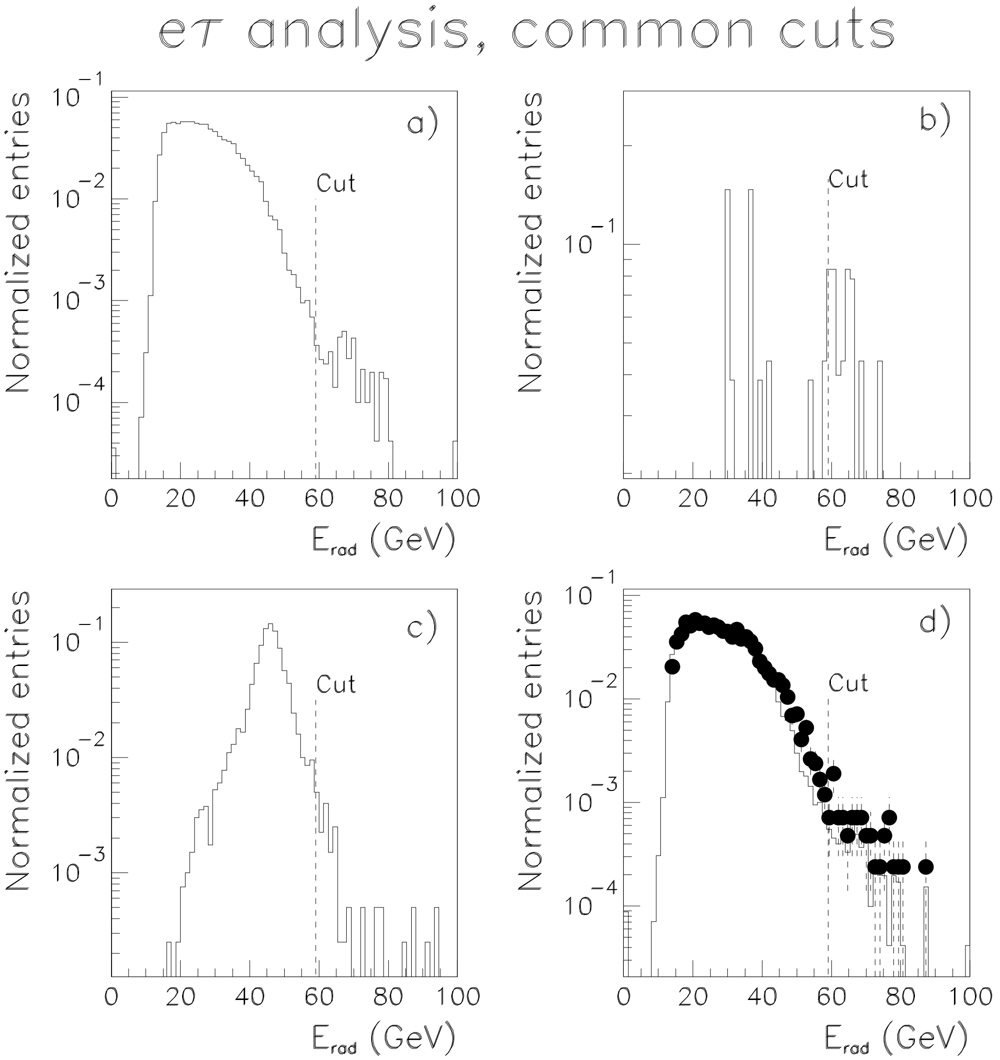

Figure 5.32: Radial electromagnetic energy for the $e\tau$ candidate events. **a)** shows the distribution for Monte Carlo tau pairs **b)** shows the distribution for Monte Carlo generated electron pairs, **c)** shows the Monte Carlo signal distribution, and **d)** shows the total Monte Carlo background in histogram and data as points.

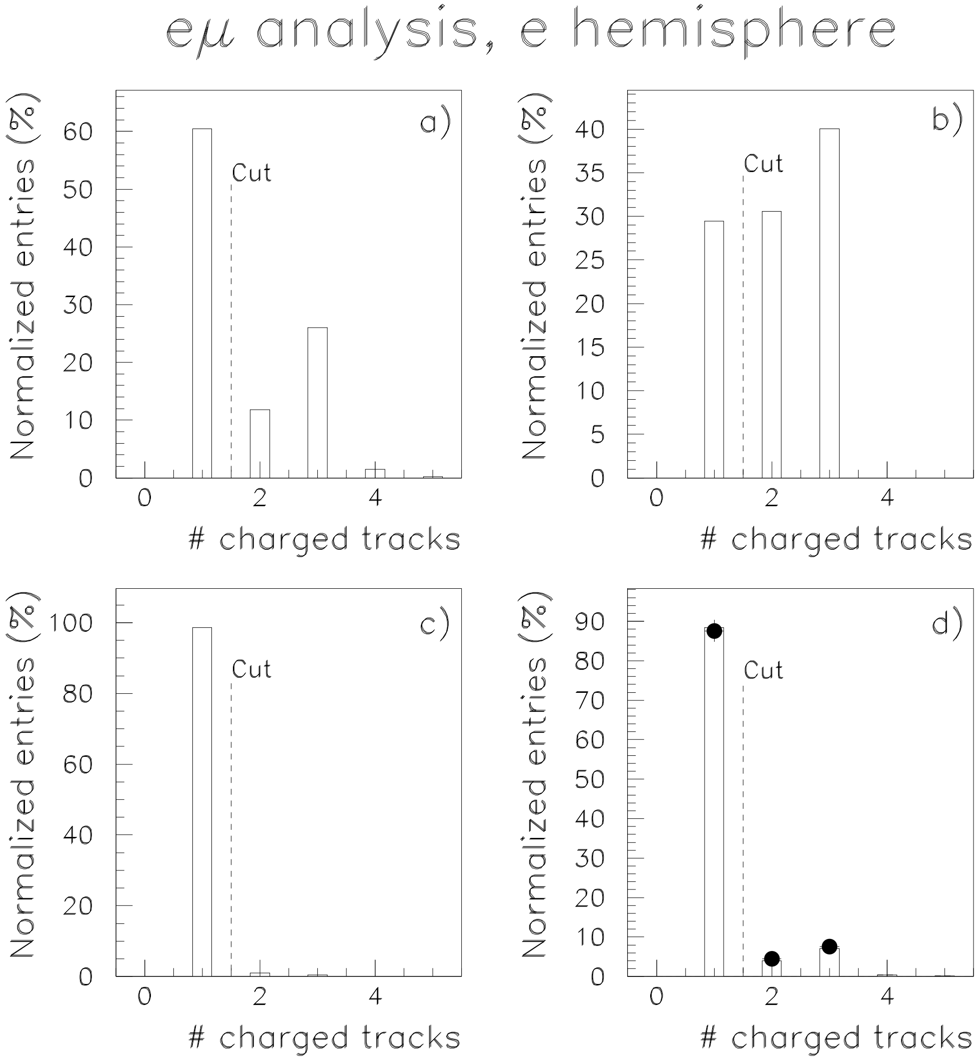

Figure 5.33: Number of charged tracks in the electron hemisphere in $e\mu$ candidate events (without the both-hemisphere cut on electron E_{em}/E_{beam} and muon p/E_{beam}). **a)** shows the distribution for Monte Carlo tau pairs, with the tau in the electron hemisphere decaying hadronically (misidentified as an electron if passing the cut), **b)** shows the distribution for Monte Carlo generated muon pairs, **c)** shows the Monte Carlo signal distribution, and **d)** shows the total Monte Carlo background in histogram and data as points.

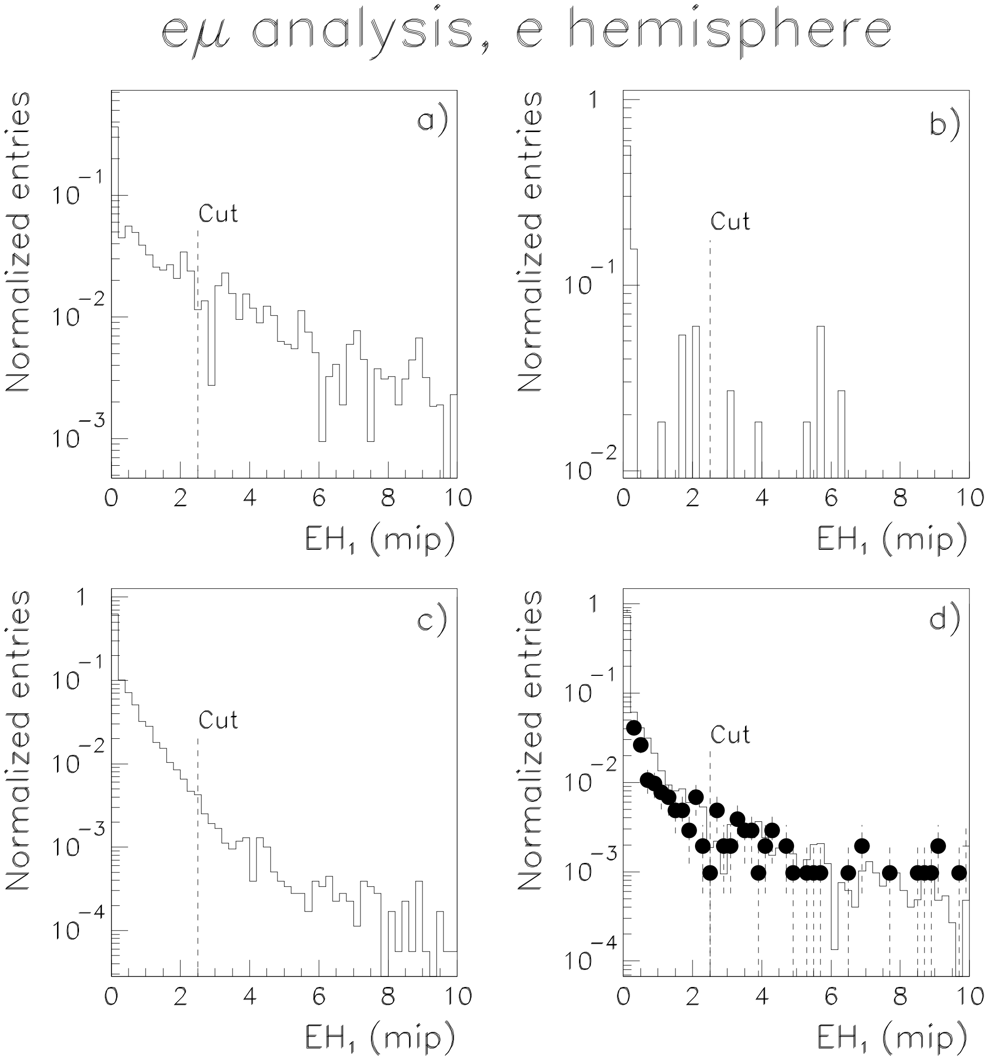

Figure 5.34: Energy deposited in the first HCAL layer for the leading charged track in the electron hemisphere in $e\mu$ candidate events (without the combined cut on muon p/E_{beam} and electron E_{em}/E_{beam}). **a)** shows the distribution for Monte Carlo tau pairs, with the tau in the electron hemisphere decaying hadronically (misidentified as an electron if passing the cut), **b)** shows the distribution for Monte Carlo generated muon pairs, **c)** shows the Monte Carlo signal distribution, and **d)** shows the total Monte Carlo background in histogram and data as points.

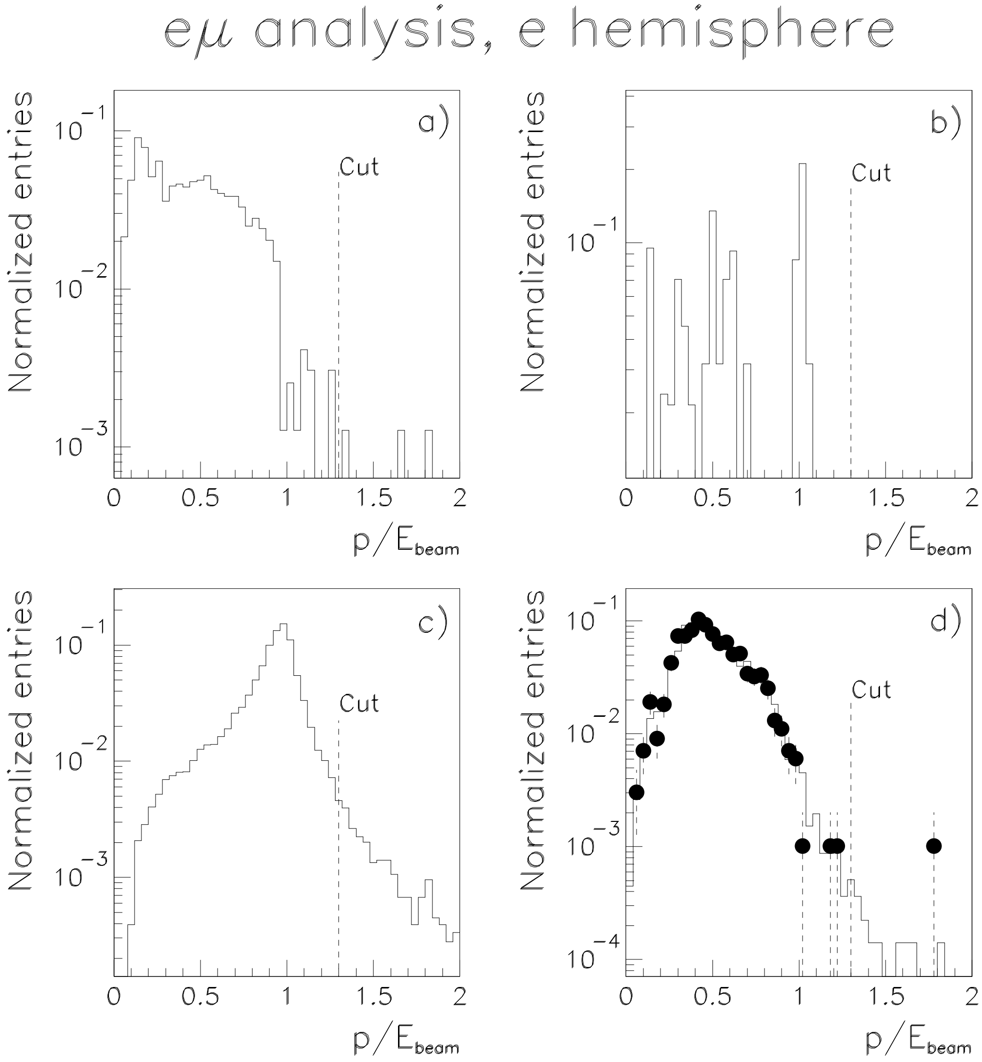

Figure 5.35: Normalized momentum for the leading charged track in the electron hemisphere in $e\mu$ candidate events (without the combined cut on muon p/E_{beam} and electron E_{em}/E_{beam}). **a)** shows the distribution for Monte Carlo tau pairs, with the tau in the electron hemisphere decaying hadronically (misidentified as an electron if passing the cut), **b)** shows the distribution for Monte Carlo generated muon pairs, **c)** shows the Monte Carlo signal distribution, and **d)** shows the total Monte Carlo background in histogram and data as points.

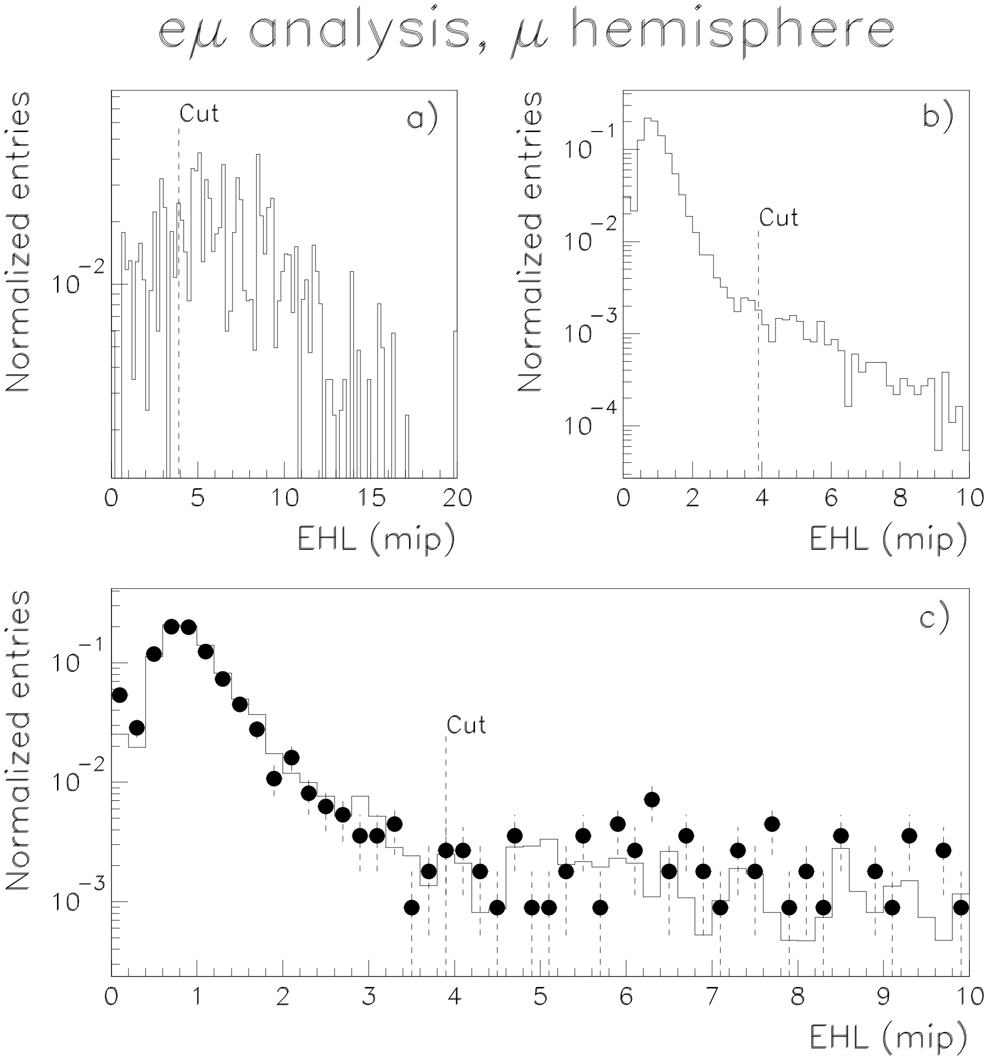

Figure 5.36: Energy per HCAL layer (EHL) for the leading charged track in the muon hemisphere in $e\mu$ candidate events (without the combined cut on muon p/E_{beam} and electron E_{em}/E_{beam}). The lower edge of the cut at 0.03 mip is not shown explicitly. **a)** shows the distribution for Monte Carlo tau pairs, with the tau in the electron hemisphere decaying hadronically (misidentified as a muon if passing the cut), **b)** shows the Monte Carlo signal distribution, and **c)** shows the total Monte Carlo background in histogram and data as points.

This last EHL cut has a higher efficiency than the corresponding cut in the muon selection routine in the $\mu\tau$ analysis, due to the less severe background problems in this channel. See figure 5.36.

- Normalized electromagnetic energy less than 0.8.

The last cut on normalized electromagnetic energy is a cut only to "clean up" events that for some reason or another have behaved in a strange or unexpected way; As such, the cut is placed far out in the tail of the signal distribution, and almost no efficiency is lost, see figure 5.37.

5.6.3 The cuts common to both hemispheres

The cuts common to the two hemispheres are in the $e\mu$ channel limited to a single cut, but this is an essential cut on the topology of the event which clearly distincts the signal region from the background. The cut combines the two hemispheres and is a cut on the electromagnetic energy of the electron and the momentum of the muon:

- The electromagnetic energy of the electron and the momentum of the muon were both required to be at most 2 σ (resolution) down from the peak value of 1, that is: Normalized electromagnetic energy of the electron was required to be above 0,88, and normalized momentum of the muon was required to be above 0.92.

This cut removes all the remaining data events (see figure 7.6) while keeping a rather high efficiency for the signal, making a counting method of Poisson statistics a good method of determining a 95% CL upper limit.

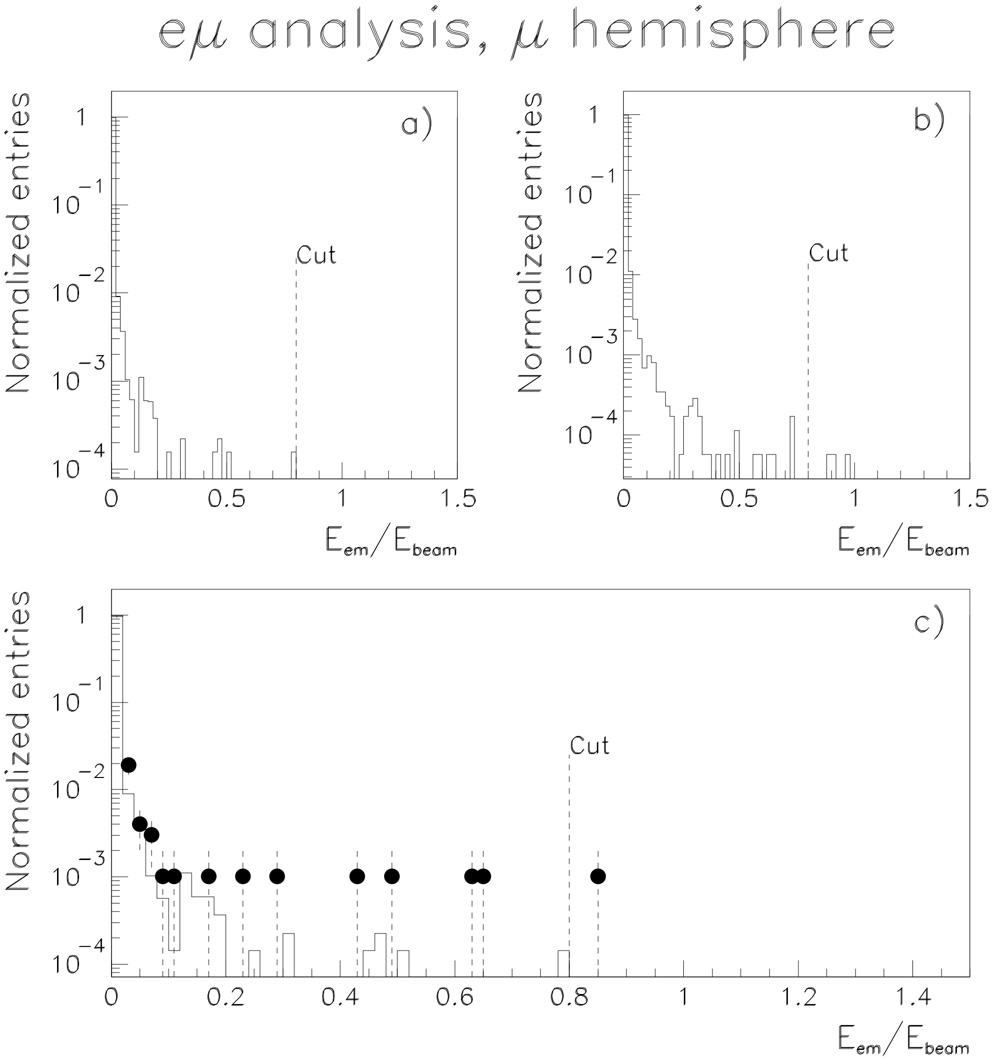

Figure 5.37: Normalized electromagnetic energy for the leading charged track in the muon hemisphere in $e\mu$ candidate events (without the combined cut on muon p/E_{beam} and electron E_{em}/E_{beam}). **a)** shows the distribution for Monte Carlo tau pairs, with the tau in the electron hemisphere decaying hadronically (misidentified as a muon if passing the cut), **b)** shows the Monte Carlo signal distribution, and **c)** shows the total Monte Carlo background in histogram and data as points.

Chapter 6

Determination of 95% CL. upper limits on $Br(Z^0 \rightarrow l_i l_j, i \neq j)$

6.1 Statistical method

Since no signal was found by any of the searches, the next step in the analyses was to determine a 95% CL limit on the branching ratio of the three LFV decays. Since there in both the $\mu\tau$ and $e\tau$ analyses is an irreducible background present, an unbinned likelihood method was used for these two cases. The likelihood function was defined as a product over all data events accepted by the analysis

$$L = \prod_{i=1}^{N_{data}} \left((1 - f_s)P_b(x_i) + f_s P_s(x_i)\right) \tag{6.1}$$

(All variables in the equation should have ij, or more accurately $i\tau$, $i \neq \tau$ superscripts, to distinguish between the $\mu\tau$ and $e\tau$ analyses, but this would make the equation very hard to read, and so the difference is only implied.) The number x_i denotes the muon momentum (electron energy) normalized to the beam energy, f_s the signal fraction in the data, $P_b(x)$ the normalized probability density for the background as determined from Monte Carlo, and $P_s(x)$ the normalized probability density for the signal as determined from Monte Carlo. The background fraction was parametrized in terms of the signal as $f_s = \frac{B \cdot \xi}{N_{data}}$ where B is the signal branching fraction and N_{data} the number of accepted candidates in data. The accurate determination of the functions $P_b(x)$ and $P_s(x)$ will be treated in sections 6.3. The 95% upper limits were derived utilizing the fact that twice the log likelihood ratio statistic is approximately χ_1^2 [37], yielding a 95% CL upper limit at the point where the log likelihood has fallen down an amount $(1.96)^2/2$ with respect to the maximum value.

In the $e\mu$ case, the signal is, as earlier explained, much more clearly distinguished from the background than what is the case for the two other analyses. Thus the analysis could be performed in such a way that very few background events passed the cuts, while still maintaining a high signal detection efficiency. Therefore, a simple counting method and corresponding Poisson statistics method, according to the number of accepted candidates in data and the expected background from Monte Carlo simulations, was used.

6.2 Uncertainties in the sensitivity factor ξ^{ij}

The uncertainties in the sensitivity factor, ξ^{ij}, come from many different sources. When looking at the definition of ξ^{ij}, equation 5.2, one sees that it is composed of two factors, independently determined; the signal efficiency and the total number of Z^0. The relative uncertainty in ξ^{ij} is then found as a sum of squares between the relative uncertainty of the efficiency and the relative uncertainty of the total number of Z^0.

6.2.1 Errors on the total number of Z^0, $N^{ij}_{Z^0}$

The relative uncertainty of the total number of Z^0 was computed as a sum of squares between relative uncertainties of the factors used in determining the number. These are, as can bee seen from equation 5.1, the luminosity, $\mathcal{L}^{ij,i_y}$, the hadronic cross section, $\sigma_h^{i_y}$, and the hadronic branching ratio, B_h. The errors on these are all systematic, with the exception of the luminosity, which, in addition to a systematic contribution, also contains an error of statistical origin. Thus it is favourable to divide the errors in two main classes: systematic errors and statistical errors.

Statistical errors on $N^{ij}_{Z^0}$

The statistical errors on $N^{ij}_{Z^0}$ contain contribution from one source: the number of Bhabhas recorded by the luminosity monitor. This contributes as the square root of the recorded number of Bhabha events, from simple statistics. This statistical error was largest for the 91 run, due to the small statistics which in addition was spread out over 7 scan points, and had a relative contribution of typically 0.8%, whereas it was negligibly small for the other years (typically less than 0.1%).

Systematic errors on $N^{ij}_{Z^0}$

The relative systematic errors on the three components of the total number of Z^0 were as following:

- Relative error on the luminosity $\mathcal{L}^{ij,i_y}$: 0.5%
- Relative error on the hadronic cross section $\sigma_h^{i_y}$, estimated from ZFITTER: 0.2%
- Relative error on the hadronic branching ratio, B_h, found from Review of Particle Properties: 0.215%

6.2.2 Errors on the efficiency, ε^{ij}_{tot}

The errors of the efficiency is the larger of the two main parts of the error on ξ^{ij}, both in terms of the numerical value and in number of different contributors. Once more it is feasible to divide the contribution into two parts: one statistical and one systematic.

Statistical errors on ε^{ij}_{tot}

These errors originate from the errors on the four factors determining the efficiency, described in section 5.3.6. For the pure efficiencies, ε^{ij}_{pre} and ε^{ij}_{both} and also the pure efficiency parts of the i lepton selection routine as tagged by data (the efficiency $\varepsilon^{ij}_{i,tag}$), these errors are, for a general efficiency ε giving a binomial distribution (the event is either accepted, with a probabilily p, or rejected, with a probability $(1-p)$):

$$\sigma_{n^{acc}} = \sqrt{np(1-p)} \tag{6.2}$$

where the n trials all have the probability p of passing the cuts, and n^{acc} events are actually accepted. If p is approximated by the efficiency, $\varepsilon = n^{acc}/n$, and n is treated as a constant, one gets from equation 6.2:

$$\sigma_{n^{acc}} = \sqrt{n^{acc}(1-\varepsilon)} \qquad \Rightarrow \qquad \sigma_{\varepsilon} = \frac{\sigma_{n^{acc}}}{n} = \sqrt{\frac{\varepsilon(1-\varepsilon)}{n}}$$

Thus the error on the efficiency goes as one over the square root of the number of events input to the rotine, which is directly proportional to the number of events in the sample. This in turn means that the statistical uncertainty will be largest for the smallest event samples, which are the signal Monte Carlo generated samples. The efficiencies where the signal Monte Carlo is used directly, are the preselection efficiency, ε^{ij}_{pre}, and the efficiency of the cuts on both hemispheres, ε^{ij}_{both}.

The statistical errors on the lepton selection correction factors, C^{ij}_{i}, and the correlation factor, C^{ij}_{corr}, (see section 5.3.6), is a little more complicated, due to the fact that the distributions no longer are merely binomial, but rather multinomial. The uncertainty of these two factors are treated more thoroughly in sections A.1 and A.2.

The four factors in the signal efficiency are listed in table 7.1, where the values of the factors are the average values taken over the 4 years 91–94, weighted by the total number of Z^0 for that year.

Systematic errors on ε^{ij}_{tot}

These errors are, as is mostly the case with systematic errors, quite difficult to estimate. The ones included in this paper are listed below.

Smearing of Monte Carlo variables: This error was estimated by simply turning the smearing routine off, and then observe the difference between the "correct" efficiency and the one obtained in the unsmeared case. The error was conservatively set at the difference between these two values, based on the assumption that the error cannot be larger than the effect itself, giving relative errors of 1.3% in the $\mu\tau$ analysis, 1.4% in the $e\tau$ analysis, and 2.6% in the $e\mu$ analysis, due to the larger sensitivity of this analysis because of the combined cut on muon momentum/electron electromagnetic energy.

Background in the tagged lepton samples: The lepton pair tagging routines, described in section 5.3.6, will contain small backgrounds from other physics channels than the ones they intend to tag on. This background was estimated to be negligible for the muon pair and electron pair selection routines, seeing that less than 10 events from other Monte Carlo generated samples passed the cuts. The situation for the tau pair tagging routine was a little different, as there here were non-negligible contributions from other Monte Carlo samples. Assuming that the error from these contributions cannot be larger than the actual backgrounds themselves, the systematic contribution was taken as the efficiency of the tau tagging routine on muon (and electron) pair Monte Carlo events divided by the efficiency of the tau tagging routine on tau pair Monte Carlo events. This procedure gave relative errors of approximately 0.4% for the muon pair background, and 0.9% for the electron pair background in the tau pair tagged event samples.

All these different contributions to the total error on the sensitivity factor ξ^{ij} were added as a sum of squares between all the different contributions, giving the total uncertainty on ξ^{ij} as listed in the last column of table 7.1. This value corresponds roughly to a 3% relative error (2.8% in $\mu\tau$, 2.9% in $e\tau$, and 3.1% in $e\mu$). The errors were then accounted for by subtracting one sigma (i.e. roughly 3%) from the sensitivity factor ξ^{ij}. This is a conservative way of accounting for the uncertainty in the sensitivity [38].

6.3 Treatment and parametrization of the background and signal distributions

The background was, as mentioned in section 4.2, estimated by using Monte Carlo generated samples of events. By using the fundamental relation for the luminosity,

$$N = \sigma \cdot \mathcal{L} \tag{6.3}$$

one finds the relation

$$\mathcal{L} = \frac{N}{\sigma}$$

where N denotes the number of reactions, σ the total cross section for the process, and $\mathcal{L}$ the corresponding luminosity. If one assumes equation 6.3 for the Monte Carlo generated samples of lepton pairs, one obtains:

$$N^{gen}_{kk,MC} = \sigma_{kk} \cdot \mathcal{L}_{kk,MC} \qquad \Rightarrow \qquad \mathcal{L}_{kk,MC} = \frac{N^{gen}_{kk,MC}}{\sigma_{kk}} \tag{6.4}$$

where the subscript kk denotes electron pair, muon pair or tau pair (ee, $\mu\mu$ or $\tau\tau$). This equation is of course only valid at one specific energy point, as the cross sections σ_{kk} are highly energy dependent.

The cross sections σ_{kk} should now denote the cross sections for producing lepton pairs in the reaction $e^+e^- \to l_k\overline{l_k}$ *corresponding to the generated sample*, not necessarilly involving a real Z^0. This becomes important for the generated samples of Bhabha events for two reasons, which are intervened:

1. The production of e^+e^- pairs can occur not only by the normal s-channel diagram, but also through the t-channel diagram (see figure 6.1). At the Z^0 peak, the s-channel is the most important one for tracks in the typical barrel area ($|\theta - 90^\circ|$ is small), while the t-channel is the larger contributor to the cross section in the forward direction ($|\theta - 90^\circ|$ is large). In addition, the t-channel is relatively unaffected by a small relative change of the energy around the Z^0 peak (goes as $\sigma_t \propto 1/s$ where s is the energy), whereas the s-channel decreases dramatically when the energy falls below the Z^0 mass, making the Z^0 a virtual particle.

2. Because of the rapid increase of the cross section as one gets close to θ=0° or 180°, the official DELPHI generated Bhabha samples have been generated in specific polar angle sections. Since the analyses presented here only use the barrel part of DELPHI,

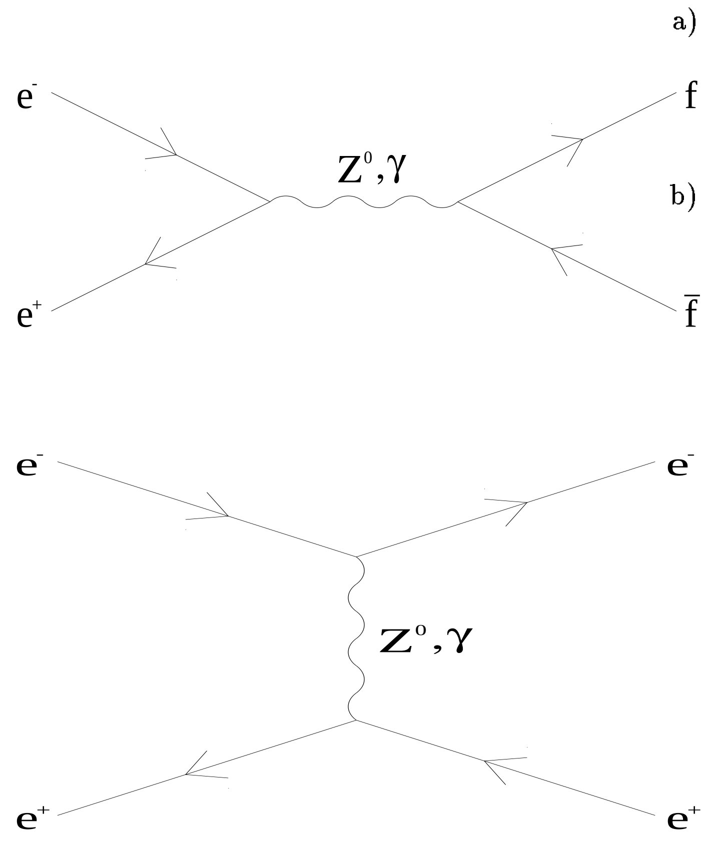

Figure 6.1: The two first order Feynman diagrams contributing to the process $Z^0 \rightarrow l_i\overline{l_i}$. Figure **a)** shows the s-channel annihilation of e^+ and e^- (which can propagate through both a photon or a (real or virtual) Z^0), which in general will create any pair of fermion anti-fermion, including all three charged lepton pairs. Figure **b)** shows the t-channel photon or Z^0 exchange, in which the initial state electron and positron does not annihilate, but "reappear" in the final state.

Bhabha samples generated in the barrel only will suffice. Thus the samples used were only generated in the polar angle range 37°–143°, changing the "effective" cross section of the generated samples.

Taking these two points into account, it is clear that the cross sections to be used in equation 6.4 will be approximately the same for muon pairs and tau pairs (neglecting the mass difference, as it is relatively insignificant at LEP energies), but will differ for electron pairs. Thus the cross sections listed in table 5.1 have a common cross section for muon pairs and tau pairs (σ_l), and a specific cross section for lepton pairs (σ_e).

If one takes the factor σ_{kk} as the leptonic cross section, that is the cross section of the process $Z^0 \rightarrow l_k\overline{l_k}$, with the differences for the $Z^0 \rightarrow e^+e^-$ as mentioned above, then the factor $\mathcal{L}_{kk,MC}$ of equation 6.4 may be viewed as the luminosity equivalence for the Monte Carlo sample of a number of $N_{kk,MC}^{gen}$ generated lepton pairs of type kk. Thus the factor $\mathcal{L}_{kk,MC}$, called the Monte Carlo luminosity, was calculated, with the procedure of equation 6.4, for all energy points for all years, using the corresponding normal luminosity for that energy point (see table 5.1). These Monte Carlo luminosities were then used, together with the normal luminosities, for normalization of the background Monte Carlo samples.

Now the number $N^{gen}_{kk,MC}$ in equation 6.4 refers to the total number of events of electron pairs, muon pairs or tau pairs. The corresponding number of such lepton pairs accepted by the general ij analysis is of course much smaller, and can be expressed in terms of an efficiency:

$$N^{ij,acc}_{kk,MC} = \varepsilon^{ij}_{kk} \cdot N^{gen}_{kk,MC} \tag{6.5}$$

The Monte Carlo luminosity should in principle, if the agreement between data and Monte Carlo is perfect, give the correct scaling factor for the different generated lepton pair samples. But since there are discrepancies between Monte Carlo generated events and real data, and presumably in such a way that the Monte Carlo is more "well behaved" than real data, since there will always be effects not accounted for in the simulation, one would suspect the efficiency ε^{ij}_{kk} of equation 6.5 to be slightly too high. This effect would correspond to giving a Monte Carlo luminosity that was too high, resulting in a too high predicted background. This is not as serious as it may look, since the likelihood method described in section 6.1 only uses the *normalized* probability densities for signal and background, making the absolute value of the totat estimated background a free parameter of the fit. Nevertheless, the scaling between different backgrounds will of course be sensitive to such effects, as the values of the ε^{ij}_{kk} may be further away from the actual value for some backgrounds than for others, and one would in any case like to have as good an agreement between Monte Carlo predictions and data as possible. Therefore, the values of the ε^{ij}_{kk} efficiencies were corrected, effectively by correcting the values of the Monte Carlo luminosities, $\mathcal{L}_{kk,MC}$, giving slightly different Monte Carlo luminosities for the different analysis, $\mathcal{L}^{ij}_{kk,MC}$.

Looking at the 4 factors determining the *signal* efficiency (section 5.3.6), the two most obvious places where such disagreements could occur, are the two lepton identification efficiencies, ε^{ij}_{i} and ε^{ij}_{j}. For the $\mu\tau$ and $e\tau$ analyses, generalized to the $i\tau$ analysis, where $i = e$ or μ, the Monte Carlo luminosity in the tau lepton samples, $\mathcal{L}_{\tau\tau,MC}$, was therefore multiplied with two factors, the first being the fraction of the efficiency of the i lepton routine on i lepton pairs tagged in data and the same efficiency on i lepton pairs tagged on the Monte Carlo i lepton pair sample, while the other factor was the same fraction for the τ lepton case, that is

$$\mathcal{L}^{i\tau}_{\tau\tau,MC} = \mathcal{L}_{\tau\tau,MC} \cdot \frac{\varepsilon^{i\tau}_{i,tag,Data}}{\varepsilon^{i\tau}_{i,tag,ii,MC}} \cdot \frac{\varepsilon^{i\tau}_{\tau,tag,Data}}{\varepsilon^{i\tau}_{\tau,tag,\tau\tau,MC}} \tag{6.6}$$

where the factor $\varepsilon^{i\tau}_{j,tag,Data}$ is the efficiency in the $i\tau$ analysis of the j lepton selection routine on tagged j lepton pairs ($j = i$ or τ), and the factor $\varepsilon^{i\tau}_{j,tag,jj,MC}$ is the same efficiency on Monte Carlo generated jj lepton pairs.

For the background from the other two channels, electron pairs and muon pairs, the corrections were applied only for the hemisphere which was actually present in the background; for example, for the $e\tau$ analysis, the Monte Carlo luminosity for the electron pair background, $\mathcal{L}_{ee,MC}$, was corrected only with the fraction corresponding to the efficiency of the electron selection routine, while the Monte Carlo luminosity for the muon pair background, $\mathcal{L}_{\mu\mu,MC}$, was not corrected at all. This was done mainly because of the low statistics in these cases (electrons passing the non-electron cuts in the tau part of the $e\tau$ analysis, or muon pairs beeing tagged as tau pairs or accepted by the electron selection routine), making it impossible to obtain reliable values for these efficiencies. Thus the general form of equation 6.6 for the $i\tau$, $i = e, \mu$ analysis can be written in compact form as:

$$\mathcal{L}^{i\tau}_{kk,MC} = \mathcal{L}_{kk,MC} \cdot \prod_{j=i,\tau} \left(1 + \left(\frac{\delta_{kj}+\delta_{k\tau}}{1+\delta_{j\tau}}\right)\left(\frac{\varepsilon^{i\tau}_{j,tag,Data}}{\varepsilon^{i\tau}_{j,tag,jj,MC}} - 1\right)\right) \tag{6.7}$$

where the δ_{ij} denote the normal delta function, which is equal to 1 if $i = j$, else 0 (the two $\delta_{k\tau}$ and $\delta_{j\tau}$ factors are introduced in order to maintain the two factors for the kk=$\tau\tau$ case).

For the $e\mu$ case, the Monte Carlo luminosity corrections were applied in exactly the same way for electron and muon pair backgrounds as described for the $\mu\tau$ and $e\tau$ analysis, that is

$$\mathcal{L}^{e\mu}_{kk,MC} = \mathcal{L}_{kk,MC} \cdot \frac{\varepsilon^{e\mu}_{k,tag,Data}}{\varepsilon^{e\mu}_{k,tag,kk,MC}} \tag{6.8}$$

for the $k = e$ or μ cases, but a different method had to be applied to the tau pair background. This is due to the fact that the $e\mu$ analysis searches for two high energy leptons, and therefore one should, if following the scheme laid out for the $\mu\tau$ and $e\tau$ cases, tag the particles with which to perform the corrections as such. This is a workable scheme for the electron and muon pair background, but fails for the tau pair background. Therefore, the corrections in this case was performed by first tagging the events as tau pairs, and then to use the electron and muon selection routines on this tagged tau pair sample to correct for the differences between data and Monte Carlo tau pairs, that is:

$$\mathcal{L}^{e\mu}_{\tau\tau,MC} = \mathcal{L}_{\tau\tau,MC} \cdot \frac{\varepsilon^{e\mu}_{e,tag,\tau\tau,Data}}{\varepsilon^{e\mu}_{e,tag,\tau\tau,MC}} \cdot \frac{\varepsilon^{e\mu}_{\mu,tag,\tau\tau,Data}}{\varepsilon^{e\mu}_{\mu,tag,\tau\tau,MC}} \tag{6.9}$$

where the factor $\varepsilon^{e\mu}_{i,tag,\tau\tau,Data}$ denotes the efficiency of the i lepton selection routine ($i = e$ or μ) on tagged *tau* pairs in data in the $e\mu$ analysis, and correspondingly on the Monte Carlo generated tau pair sample for the MC subscript.

The normalization of the background was now done by calculating the Monte Carlo luminosity by the use of the appropriate one of equations 6.7, 6.8 or 6.9 for each energy point, dividing the normal data luminosity of that energy point with the value obtained for the Monte Carlo luminosity, and summing over all energy points in a year sample, that is:

$$C^{ij,y}_{kk} = \sum_{i_y=1}^{n_y} \frac{\mathcal{L}^{ij,i_y}}{\mathcal{L}^{ij,y}_{kk,MC}} \tag{6.10}$$

where the number y refers to the year, and i_y refers to the different energy points in year y (n_y being the number of energy points for year y). These factors $C^{ij,y}_{kk}$ were then used to scale the number of accepted events in the background channels, as

$$N^{ij,scaled,y}_{kk,MC} = N^{ij,acc,y}_{kk,MC} \cdot C^{ij,y}_{kk} \tag{6.11}$$

(see equation 6.5 for the definition of the $N^{ij,acc,y}_{kk,MC}$ factor). The total predicted background from Monte Carlo was then found by summing over all years and all backgrounds,

$$N^{ij,scaled}_{kk,MC} = \sum_{y=91}^{94} N^{ij,scaled,y}_{kk,MC} \qquad \text{and} \qquad N^{ij,scaled}_{MC} = \sum_{k=e,\mu,\tau} N^{ij,scaled}_{kk,MC} \tag{6.12}$$

The backgrounds from each channel, the $N^{ij,scaled}_{kk,MC}$ numbers, are found i table 7.2, where the results for the 95% CL upper limits on the branching ratios also are quoted (see chapter 7).

For the different background and signal spectra in the likelihood methods, the $P_b(x)$ and $P_s(x)$ probability densities, several different distributions were used. For the signal distribution of the normalized muon momentum (electron electromagnetic energy), in the $\mu\tau$ ($e\tau$) analysis, $P_s(x)$, the momentum (electromagnetic energy) spectrum was taken to be that from muon (electron) pairs, which should have the same distribution, that is that of a high energy muon (electron). This spectrum was constructed as the sum of two gaussians, where the first was centered at the value 1 with a relatively small spread, to describe the peak, while the second had a larger spread, which accounted for the behaviour in the tails. The background from muon (electron) pairs also used this spectrum in the background estimate. The background from tau pairs were in both cases parametrized by a mixture of two functions. Below normalized momentum/electromagnetic energy of 1, the spectrum consisted of a polynomial of degree 5 for the $\mu\tau$ analysis and 4 for the $e\tau$ analysis. Above 1 the parametrization used was a function of the type

$$f(x) = \frac{C_1}{x^n} - C_2$$

where the constants C_1 and C_2 accounted for making the function continuous at the point $x = 1$, and for making the function drop to zero at a designated point x_0, whereas the value of n determines how steeply the function drops from the value $C_1 - C_2$ at $x = 1$. For the one remaining background, the muon pair background in the $e\tau$ analysis, it was not obvious which distribution to use, since these events obviously do not follow the distribution from the electron pairs, nor that of the tau pairs, and the statistics was too low to make a fit of a function, as was done in the tau pair case. Working from the assumption that the background events from muon pairs were caused mainly by hard photon final state radiation from one of the muons, the spectrum was assumed to be inversely propotional to the energy, since this is the theoretical prediction for the photon energy.

After all these distributions had been parametrized, the total background parametrization was constructed by adding the different background contributions, weighted by the Monte Carlo luminosity scaled number of accepted events, the numbers $N^{ij,scaled}_{kk,MC}$ from equation 6.12.

Chapter 7

Results and conclusion

The analyses described in chapter 5 resulted in efficiencies (for 4π solid angle) on the signal as listed in table 7.1, where also the corresponding effective number of Z^0 is quoted. The total number of candidates in data and from luminosity-scaled Monte Carlo samples are shown in table 7.2, where also the 95% CL limit is quoted. The stability of the likelihood method versus the lower accepted $p/E_{beam}(E_{em}/E_{beam})$ value for the $\mu\tau(e\tau)$ analysis is demonstrated in figure 7.1.

7.1 The $\mu\tau$ analysis

The p/E_{beam} spectra for the muon in $\mu\tau$ candidate events are shown in figure 7.2 for Monte Carlo signal and background, and real data. The corresponding log likelihood distribution is shown in figure 7.3, where the branching fraction upper limit is marked on the x-axis. This limit was determined to $B^{95\%}_{Z^0\to\mu\tau} = 0.85 \times 10^{-5}$.

7.2 The $e\tau$ analysis

The E_{em}/E_{beam} spectra for the electron in $e\tau$ candidate events are shown in figure 7.4 for Monte Carlo signal and background, and real data. The corresponding log likelihood distribution is shown in figure 7.5, where the branching fraction upper limit is marked on the x-axis. This limit was determined to $B^{95\%}_{Z^0\to e\tau} = 1.7 \times 10^{-5}$.

7.3 The $e\mu$ analysis

The twodimensional distibution of E_{em}/E_{beam} for the electron versus p/E_{beam} for the muon in $e\mu$ candidate events before the upper cut on these two variables is shown in figure 7.6, for Monte Carlo signal and data. As can be seen, no data events lie within the defined signal area, corresponding to a 95% CL upper limit of 3.0 events. This gives an upper limit on the branching ration which is: $B^{95\%}_{Z^0\to e\mu} = 0.25 \times 10^{-5}$.

7.4 Conclusion

A search for lepton flavour violating Z^0 decays has been performed with the DELPHI detector at LEP with data from the years 1991–1994. No signal was found in any channel,

Ch.	ε_{pre} (%)	ε_e (%)	ε_μ (%)	ε_τ (%)	ε_{both} (%)	ε_{tot} (%)	ξ (10^5)
$\mu\tau$	47.1±0.4	—	84.5±0.2	45.0±0.2	91.9±0.7	16.5±0.2	6.45±0.18
$e\tau$	54.5±0.5	69.1±0.2	—	44.9±0.5	98.3±0.9	16.6±0.3	6.30±0.18
$e\tau$	57.5±0.4	84.6±0.1	82.8±0.1	—	77.4±0.6	31.2±0.3	12.2±0.38

Table 7.1: The 4 efficiencies treated in section 5.3.6, together with the total efficiency. Here the factor ε_{pre} denotes the preselection efficiency, ε_e denotes the efficiency of the electron selection routine, ε_μ denotes the efficiency of the muon selection routine, ε_τ denotes the efficiency of the tau selection routine, and ε_{both} denotes the product of the efficiency of the cuts on global variables and the correlation correction factor. The ε_{tot} factor gives the total efficiency. The effective number of Z^0, as defined in section 5.3.5, is listed in the last column. Values for the different efficiencies are averages over the 4 years, weighted by the number of Z^0. Errors on the efficiencies are statistical only, whereas the error on ξ includes systematics.

Channel	Real data	Number of candidates from:			95% Cl Upper limit (10^{-5})
		e^+e^-	$\mu^+\mu^-$	$\tau^+\tau^-$	
$\mu\tau$	4137	—	5.2	4388	0.85
$e\tau$	4145	4.8	7.8	4226	1.7
$e\mu$	—	—	2.0	1.0	0.25

Table 7.2: The number of accepted candidates for the three analyses. The columns 3, 4, and 5, show the sizes of the Monte Carlo generated samples after luminosity-scaling as described in section 6.3.

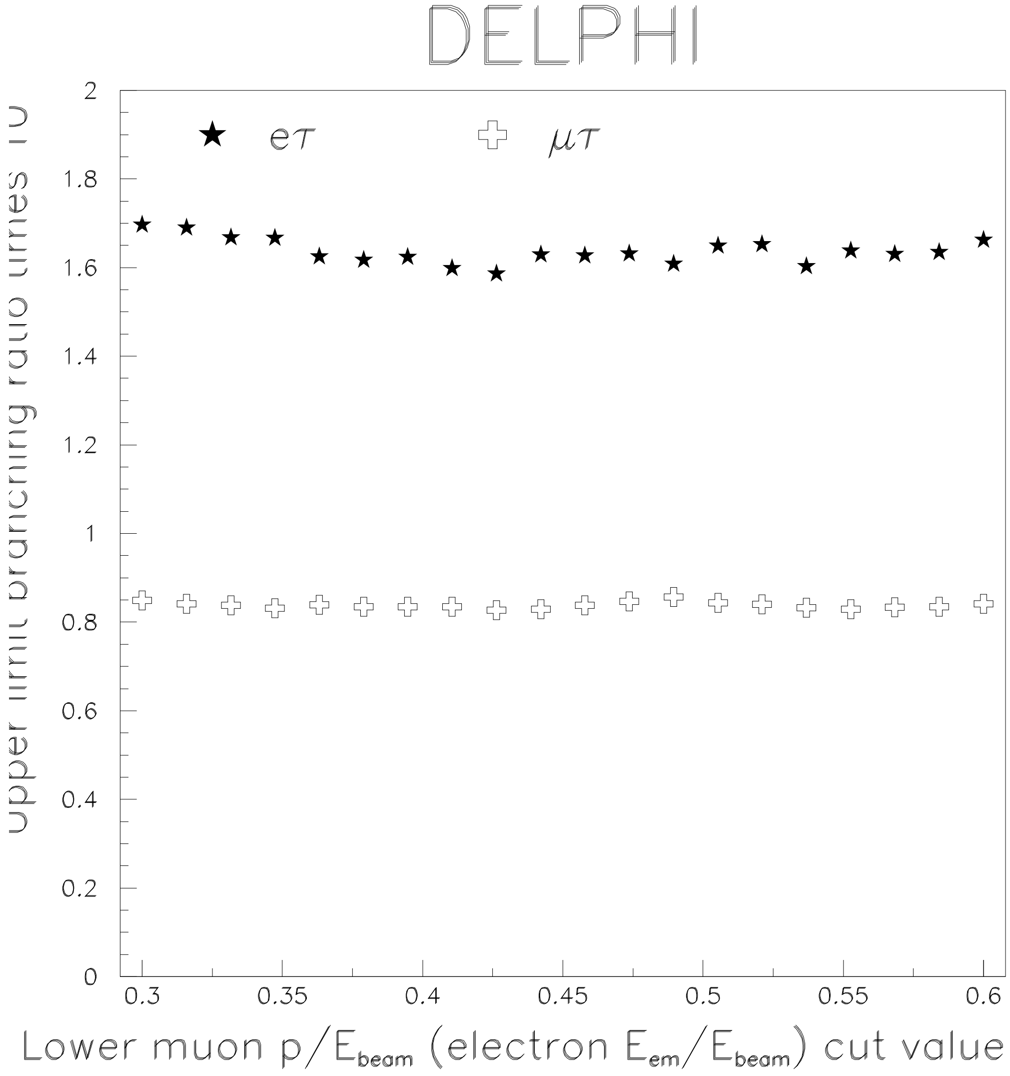

Figure 7.1: Signal branching fraction upper limit as a function of the lower muon p/E_{beam}(electron E_{em}/E_{beam}) cut value for the $\mu\tau$ and $e\tau$ analyses.

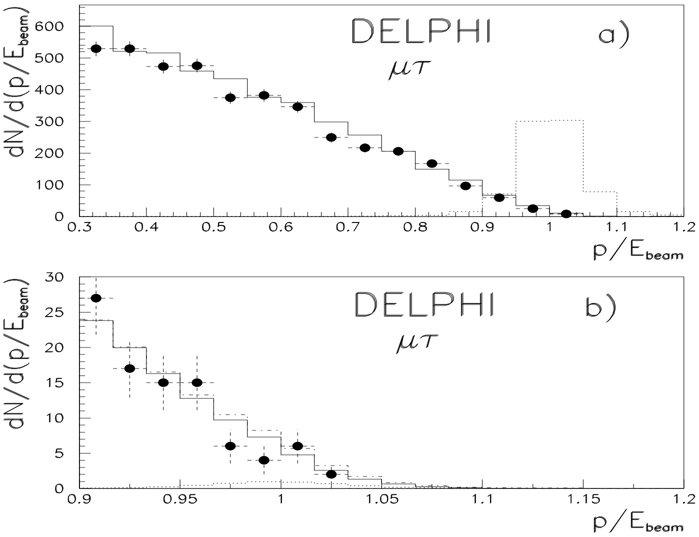

Figure 7.2: Normalized muon momentum spectra in $\mu\tau$ candidate events. **a):** Histogram: Luminosity scaled background (from Monte Carlo). Black dots: data. Dotted histogram: signal with arbitrary normalization. **b):** The signal region. Black dots: data. Solid histogram: background corresponding to the 95% upper limit signal fraction. Dotted histogram: Signal corresponding to the 95% upper limit. Dash-dotted histogram: Background plus signal.

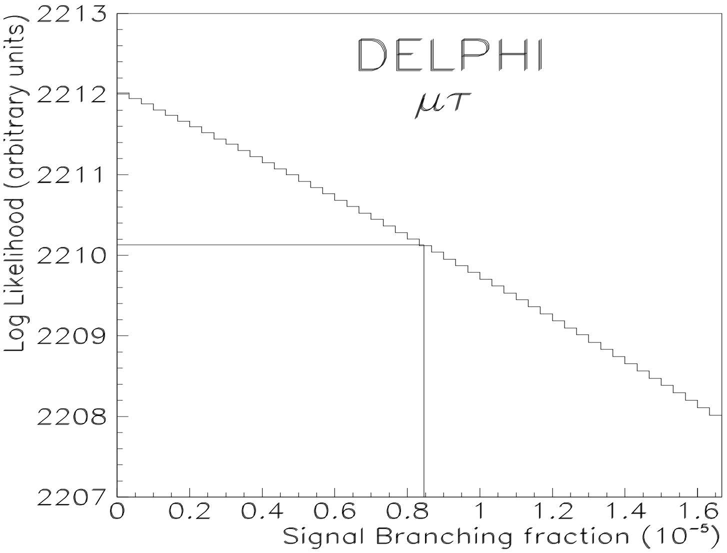

Figure 7.3: The log likelihood as a function of the $Z^0 \rightarrow \mu\tau$ branching fraction. The 95% upper limit is marked by a vertical line.

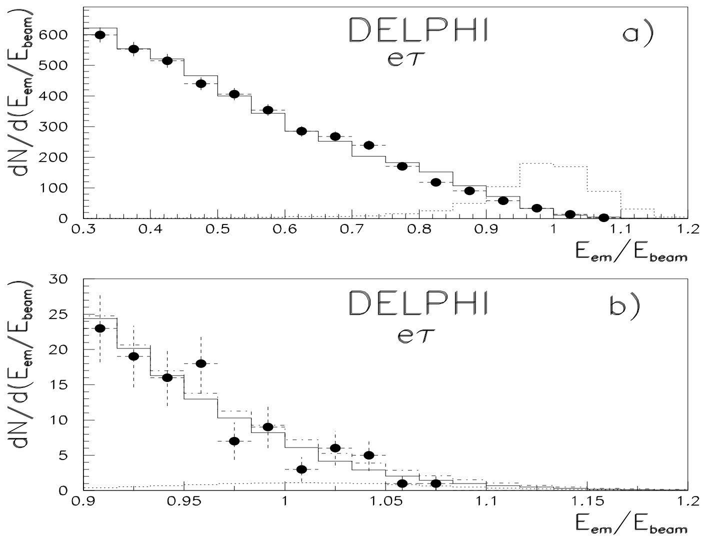

Figure 7.4: Normalized electron electromagnetic energy spectra in $e\tau$ candidate events. **a):** Histogram: Luminosity scaled background (from Monte Carlo). Black dots: data. Dotted histogram: signal with arbitrary normalization. **b):** The signal region. Black dots: data. Solid histogram: background corresponding to the 95% upper limit signal fraction. Dotted histogram: Signal corresponding to the 95% upper limit. Dash-dotted histogram: Background plus signal.

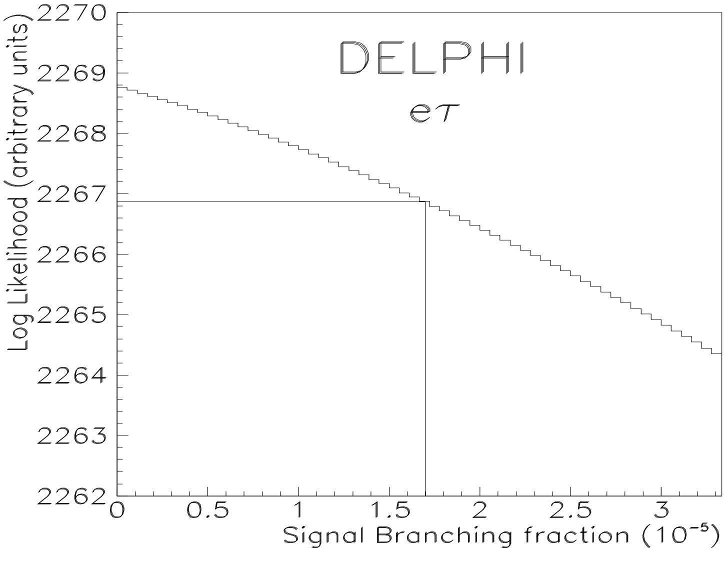

Figure 7.5: The log likelihood as a function of the $Z^0 \to e\tau$ branching fraction. The 95% upper limit is marked by a vertical line.

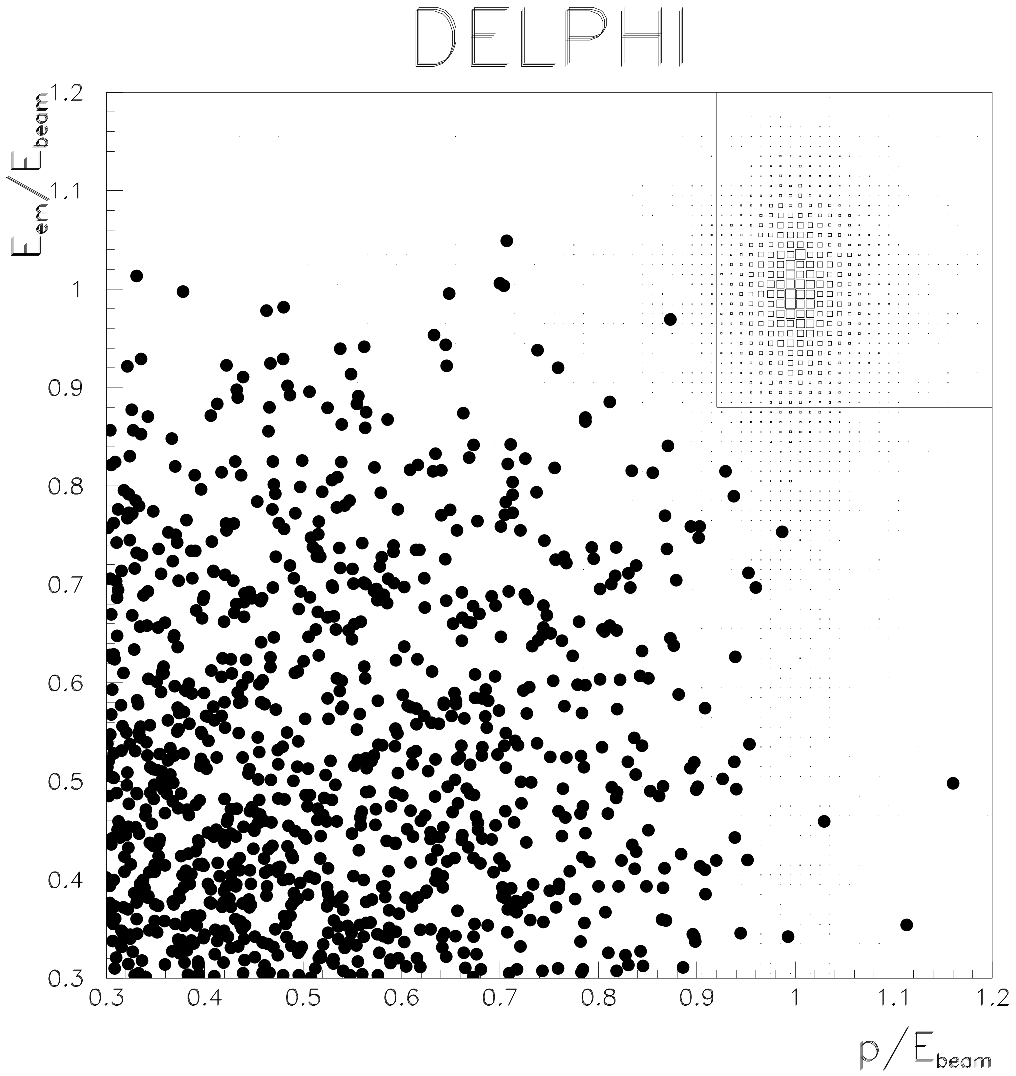

Figure 7.6: Normalized electromagnetic energy for the electron versus normalized momentum for the muon for $e\mu$ candidate events. Boxes are expected signal and black dots are data.

Group	Data from LEP runs used	$Br(Z^0 \to \mu\tau)$	$Br(Z^0 \to e\tau)$	$Br(Z^0 \to e\mu)$
DELPHI	1991–1994	0.85×10^{-5}	1.7×10^{-5}	0.25×10^{-5}
OPAL	1991–1994	1.7×10^{-5}	0.98×10^{-5}	0.17×10^{-5}
L3	1990-1992	1.9×10^{-5}	1.3×10^{-5}	0.6×10^{-5}
ALEPH	1989–1990	$10. \times 10^{-5}$	$12. \times 10^{-5}$	2.6×10^{-5}
DELPHI	1990–1991	13.5×10^{-5}	10.8×10^{-5}	3.2×10^{-5}

Table 7.3: The currently latest published limits from the 4 LEP experiments on the lepton flavour violating decays of the Z^0. The results obtained in this paper are listed in the first row, and have as of June 18, 1996 not yet been published.

and the 95% CL upper limit on the branching ratios are listed in table 7.3, together with the last published results from the other three LEP experiments [18, 20, 21]. The most recent published results from DELPHI proir to this work [19], is also listed in this table.

Appendix A

Multinomial statistics for C_i^{ij} and C_{corr}^{ij}

The statistical model of multinomial trials is based on 3 principles [22, pages 422–423]:

- The outcome of each trial belongs to one of k mutually exclusive categories or cells, labelled $1, 2, \ldots, k$.
- The probability that a trial will result in the ith cell is denoted by p_i, $i = 1, \ldots, k$, with $\sum_{i=1}^{k} p_i = 1$. These cell probabilities remain the same for all trials.
- The trials are independent.

and yields, among others, these two results:

$$Var(n_i) = np_i(1 - p_i) \quad i = 1, \ldots, k \tag{A.1}$$

$$Cov(n_i, n_j) = -np_ip_j \quad i = 1, \ldots, k \quad i \neq j \tag{A.2}$$

where the number n_i denotes the frequency of cell i.

We now have the well-known formula

$$Var\left(f\left(x_1, x_2, \ldots, x_n\right)\right) = \sum_{i=1}^{n}\sum_{j=1}^{n}\left(\frac{\partial f}{\partial x_i}\right)\left(\frac{\partial f}{\partial x_j}\right)Cov\left(x_i, x_j\right)$$

which, by utilizing the fact that $Cov(x_i, x_i) = Var(x_i)$, is equivalent to

$$Var\left(f\left(x_1, x_2, \ldots, x_n\right)\right) = \sum_{i=1}^{n}\left(\frac{\partial f}{\partial x_i}\right)^2 Var\left(x_i\right) + 2\sum_{i\neq j}^{n}\left(\frac{\partial f}{\partial x_i}\right)\left(\frac{\partial f}{\partial x_j}\right)Cov\left(x_i, x_j\right) \tag{A.3}$$

This relation will be used later to calculate $Var(C_i^{ij})$ and $Var(C_{corr}^{ij})$. In all the forthcoming equations, the letters i, j denote one of the three leptons e, μ, τ. Thus, the expression $C_{e\mu}^{e}$ means the efficiency correction factor for the electron identification routine in the $e\mu$ analysis, and so forth.

Class	i lepton selection routine	i lepton tag routine
A	+	+
B	−	+
C	+	−
D	−	−

Table A.1: The four categories for the C_i^{ij} studies. A "+" sign denotes that the track is accepted by the routine, while a "–" sign denotes that it is rejected by the routine.

A.1 The C_i^{ij} (C_j^{ij}) factor

The C_i^{ij} (C_j^{ij}) factor is defined as the total efficiency of the lepton selection routine on i (j) leptons divided by the efficiency of the lepton selection routine on the tagged i (j) leptons, that is

$$C_i^{ij}(C_j^{ij}) = \frac{\varepsilon_{i(j)}^{ij}}{\varepsilon_{i(j),tag}^{ij}} \tag{A.4}$$

both efficiencies being determined from Monte Carlo samples of i (j) leptons. In the following only look the C_i^{ij} factor will be treated, as the analogy with the C_j^{ij} factor is obvious.

After the preselection cuts, all tracks were subjected to both the i lepton selection routine (the ones used in the analyses) and to the i lepton tagging routine (the ones used to tag i lepton pairs in data). Thus a track can fall into one of four possible mutually exclusive categories; these are listed in table A.1. Recalling equation A.4, we get:

$$C_i^{ij} = \frac{\varepsilon_i^{ij}}{\varepsilon_{i,tag}^{ij}} = \frac{n_{sel,i}^{ij}/N_{tot,i}^{ij}}{n_{tagsel,i}^{ij}/n_{tag,i}^{ij}} = \frac{n_{sel,i}^{ij} \cdot n_{tag,i}^{ij}}{n_{tagsel,i}^{ij} \cdot N_{tot,i}^{ij}} \tag{A.5}$$

Here the four numbers denote the following:

$n_{sel,i}^{ij}$ = The number of tracks accepted by the i lepton selection routine
$N_{tot,i}^{ij}$ = The total number of tracks passing the preselection cuts
$n_{tagsel,i}^{ij}$ = The number of tracks accepted by both the i lepton tag routine and the i lepton selection routine
$n_{tag,i}^{ij}$ = The number of tracks accepted by the i lepton tag routine

By comparing with the classes in table A.1, these correspondencies can be deduced:

$$\begin{aligned} n_{sel,i}^{ij} &= n_A + n_C \\ N_{tot,i}^{ij} &= n_A + n_B + n_C + n_D \\ n_{tagsel,i}^{ij} &= n_A \\ n_{tag,i}^{ij} &= n_A + n_B \end{aligned}$$

We se that the number $N_{tot,i}^{ij}$ is equivalent to the sum of the frequencies of this multinomial scheme, which is therefore considered as a constant in the calculation. By doing this, the value of one of the four other variables is also fixed, and this variable is chosen to be n_D. There remains then three independent variables in our expression for C_i^{ij}; n_A, n_B and n_C.

Substituting the values of n_A, n_B and n_C into equation A.5 gives:

$$C_i^{ij} = \frac{(n_A + n_C) \cdot (n_A + n_B)}{n_A \cdot N_{tot,i}^{ij}} = \frac{1}{N_{tot,i}^{ij}} \left(n_A + n_B + n_C + \frac{n_B + n_C}{n_A} \right) \tag{A.6}$$

This expression then leads to the following relations:

$$\frac{\partial C_i^{ij}}{\partial n_A} = \frac{1}{N_{tot,i}^{ij}} \left(1 - \frac{n_B n_C}{{n_A}^2} \right) \qquad \frac{\partial C_i^{ij}}{\partial n_B} = \frac{1}{N_{tot,i}^{ij}} \left(1 + \frac{n_C}{n_A} \right) \qquad \frac{\partial C_i^{ij}}{\partial n_C} = \frac{1}{N_{tot,i}^{ij}} \left(1 + \frac{n_B}{n_A} \right)$$

Using equation A.3, with the values for $Var(n_i)$ and $Cov(n_i, n_j)\,(i = A, B, C)$, obtained with equations A.1 and A.2, gives:

$$\begin{aligned}
Var(C_i^{ij}) &= (N_{tot,i}^{ij})^{-2} \left[\left(1 - \frac{n_B n_C}{{n_A}^2} \right)^2 N_{tot,i}^{ij} p_A (1 - p_A) + \right. \\
&\quad \left(1 + \frac{n_C}{n_A} \right)^2 N_{tot,i}^{ij} p_B (1 - p_B) + \left(1 + \frac{n_B}{n_A} \right)^2 N_{tot,i}^{ij} p_C (1 - p_C) - \\
&\quad 2 \left\{ \left(1 - \frac{n_B n_C}{{n_A}^2} \right) \left(1 + \frac{n_C}{n_A} \right) N_{tot,i}^{ij} p_A p_B + \right. \\
&\quad \left. \left. \left(1 - \frac{n_B n_C}{{n_A}^2} \right) \left(1 + \frac{n_B}{n_A} \right) N_{tot,i}^{ij} p_A p_C + \left(1 + \frac{n_C}{n_A} \right) \left(1 + \frac{n_B}{n_A} \right) N_{tot,i}^{ij} p_B p_C \right\} \right] \\
&\stackrel{\text{def}}{=} (N_{tot,i}^{ij})^{-2} (A - 2B)
\end{aligned}$$

where the last definition of the factors A and B is done to simplify the expression. In order to obtain an estimator for $Var(C_i^{ij})$, we use the approximate relations

$$p_I \approx n_I / N_{tot,i}^{ij},\ I = A, B, C$$

This in turn gives the following relations:

$$\begin{aligned}
A &= N_{tot,i}^{ij} \left\{ (n_A + n_B + n_C) + 2 \left(\frac{n_B n_C}{n_A} \right) + \left(\frac{n_B n_C}{n_A} \right)^2 \left(\frac{1}{n_A} + \frac{1}{n_B} + \frac{1}{n_C} \right) \right\} - \\
&\quad \left\{ ({n_A}^2 + {n_B}^2 + {n_C}^2) + 2 \left(\frac{n_B n_C}{n_A} \right) (n_A + n_B + n_C) + 3 \left(\frac{n_B n_C}{n_A} \right)^2 \right\} \\
B &= 3 n_B n_C + n_A (n_B + n_C) - \left(\frac{n_B n_C}{n_A} \right)^2
\end{aligned}$$

If we now define the factor C by

$$C = \left(\frac{n_B n_C}{n_A} \right)$$

we get these expressions for A and B:

$$\begin{aligned}
A &= N_{tot,i}^{ij} \left\{ (n_A + n_B + n_C) + 2C + C^2 \left(\frac{1}{n_A} + \frac{1}{n_B} + \frac{1}{n_C} \right) \right\} - \\
&\quad \{ ({n_A}^2 + {n_B}^2 + {n_C}^2) + 2C(n_A + n_B + n_C) + 3C^2 \} \qquad \text{(A.7)} \\
B &= 3 n_B n_C + n_A (n_B + n_C) - C^2 \qquad \text{(A.8)}
\end{aligned}$$

Class	i lepton selection routine	j lepton selection routine
A	$+$	$+$
B	$-$	$+$
C	$+$	$-$
D	$-$	$-$

Table A.2: The four categories for the C^{ij}_{corr} studies. A "+" sign denotes that the track is accepted by the routine, while a "–" sign denotes that it is rejected by the routine.

where

$$Var(C_i^{ij}) = (N^{ij}_{tot,i})^{-2}(A - 2B)$$

This in turn gives the result

$$\sigma_{C_i^{ij}} = \sqrt{Var(C_i^{ij})} = \left(\frac{1}{N^{ij}_{tot,i}}\right)\sqrt{A - 2B} \tag{A.9}$$

A.2 The C^{ij}_{corr} factor

The C^{ij}_{corr}factor is defined as the combined efficiency of the i and j lepton selection routines divided by the produkt of the same two single efficiencies, that is

$$C^{ij}_{corr} = \frac{\varepsilon^{ij}_{ij}}{\varepsilon^{ij}_i \cdot \varepsilon^{ij}_j} \tag{A.10}$$

These efficiencies must be determined from the low statistics sigmal Monte Carlo samples.

After the preselection cuts, all tracks were subjected to both the i lepton selection routine and the j lepton selection routine. The true i (j) lepton was tagged with 100% efficiency in the signal Monte Carlo by the use of the Monte Carlo identificaton code number. Thus a track can fall into one of four possible mutually exclusive categories; these are listed in table A.2. Recalling equation A.10, we get:

$$C^{ij}_{corr} = \frac{\varepsilon^{ij}_{ij}}{\varepsilon^{ij}_i \cdot \varepsilon^{ij}_j} = \frac{n^{ij}_{bothhem}/n^{ij}_{presel}}{(n^{ij}_{acc,i}/n^{ij}_{true,i}) \cdot (n^{ij}_{acc,j}/n^{ij}_{true,j})} = \frac{n^{ij}_{bothhem} \cdot n^{ij}_{true,i} \cdot n^{ij}_{true,j}}{n^{ij}_{acc,i} \cdot n^{ij}_{acc,j} \cdot n^{ij}_{presel}} \tag{A.11}$$

Here the six numbers denote the following:

$n^{ij}_{bothhem}$ = The number of events passing both the i and j lepton selection routines
$N^{ij}_{tot,corr}$ = The total number of tracks passing the preselection cuts
$n^{ij}_{acc,i(j)}$ = The number of the true i (j) leptons accepted by the i (j) lepton selection routine
$n^{ij}_{true,i(j)}$ = The true number of i (j) leptons passing the preselection cuts

Since there in every signal event is one and only one lepton of types both i and j, it is clear that the number of events passing the preselection cuts is equal to the true number of both i and j leptons in our calculations. Thus $n^{ij}_{true,i} = n^{ij}_{true,j} = n^{ij}_{presel} \overset{\text{def}}{=} N^{ij}_{tot,corr}$, and substituting this into equation A.11 gives:

$$C^{ij}_{corr} = \frac{n^{ij}_{bothhem} \cdot N^{ij}_{tot,corr}}{n^{ij}_{acc,i} \cdot n^{ij}_{acc,j}} \tag{A.12}$$

By comparing with the classes in table A.2, these correspondencies can be deduced:

$$\begin{aligned} n^{ij}_{bothhem} &= n_A \\ N^{ij}_{tot,corr} &= n_A + n_B + n_C + n_D \\ n^{ij}_{acc,i} &= n_A + n_B \\ n^{ij}_{acc,j} &= n_A + n_C \end{aligned}$$

Substituting n_A, n_B and n_C into equation A.12 then gives:

$$C^{ij}_{corr} = \frac{n_A \cdot N^{ij}_{tot,corr}}{(n_A + n_B) \cdot (n_A + n_C)} \tag{A.13}$$

Once more, we regard the number $N^{ij}_{tot,corr}$ as a constant, thus fixing the value of n_D, and making n_A,n_B and n_C our three independent variables.

By comparing equations A.6 and A.13, one observes that, mathematically speaking, the expression for C^{ij}_{corr} is the inverse of the expression for C^{ij}_i (obviously with the values of n_A, n_B and n_C being different in the two cases). Thus we can write

$$C^{ij}_{corr} = X^{-1} \tag{A.14}$$

where

$$Var(X) = (N^{ij}_{tot,corr})^{-2}(A - 2B)$$

and A and B are defined from equations A.7 and A.8 (with the number $N^{ij}_{tot,corr}$ instead of $N^{ij}_{tot,i}$, and of course other values of n_A, n_B and n_C). Using equation A.14, we get:

$$Var(C^{ij}_{corr}) = \left(\frac{\partial C^{ij}_{corr}}{\partial X}\right)^2 Var(X) = \left(-\frac{1}{X^2}\right)^2 Var(X) = \left(\frac{1}{X^4}\right)(N^{ij}_{tot,corr})^{-2}(A - 2B)$$

which gives:

$$\sigma_{C^{ij}_{corr}} = \sqrt{Var(C^{ij}_{corr})} = \left(\frac{1}{X^2}\right)\left(\frac{1}{N^{ij}_{tot,corr}}\right)\sqrt{A - 2B} = \left(\frac{1}{(C^{ij}_{corr})^2 \cdot N^{ij}_{tot,corr}}\right)\sqrt{A - 2B} \tag{A.15}$$

Bibliography

[1] F. Halzen and A. Martin, *Quarks & Leptons*, John Wiley & Sons, Inc., ISBN 0–471–81187–4 (1984)

[2] G. Altarelli et al., *Z Physics at LEP 1, Volume 1: Standard Physics*, CERN Yellow report CERN 89–08, Volume 1 (21. Sept. 1989)

[3] M. J. S. Levine, Phys.Rev.**D36**(1987)1329

[4] A. Mendez and Ll. M. Mir, Phys.Rev.**D40**(1989)251

[5] T. K. Kuo and N. Nakagawa, Phys.Rev.**D32**(1985)306

[6] J. Bernabeu et al., Phys.Lett.**B187**(1987)303

[7] G. Eilam and T. G. Rizzo, Phys.Lett.**B188**(1987)91

[8] G. B. Gelmini and M. Roncadelli, Phys.Lett.**B99**(1981)411

[9] J. Bernabeu and A. Santamaria, Phys.Lett.**B197**(1987)418

[10] A. Ilakovac and A. Pilaftsis, Nucl.Phys.**B437**(1995)491

[11] M. Dittmar and J. W. F. Valle, *Flavour-changing Z decays (leptonic)*, in: CERN Yellow report CERN 91–02, 1991, p.98, ed. E. Blucher, J. Jowett, F. Merrit, G. Mikenberg, J. Panman, F. M. Renard and D. Treille.

[12] DELPHI trigger group, Nucl.Instr.Meth.**A362**(1995),361

[13] Valerie Chorowicz, *Description of the DELPHI sub-detectors*, World Wide Web, http: // delonline.cern.ch:8070 / delphi$specific / cp / monitor / presenter / help_files / help_detectors.html/

[14] The DELPHI Collaboration, *Proposal for the DELPHI Surround Muon Chambers* DELPHI 92–139 TRACK 71(21. Oct 1991)

[15] C. De Clercq, *A study of Muon Identification in DELPHI with the Surround Muon Chamers* DELPHI 92–148 PHYS 241, (12. Nov 1991), unpublished

[16] A. Maio et al., *STIC, The New DELPHI Luminosity Monitor* conributed to the Elba conference, 1993

[17] V. Obrastsov et al., *Status of the DELPHI Small angle TIle Calorimeter project* conributed to the Marseille conference, 1993

[18] ALEPH Collaboration, Phys.Rep.**216**(1992)253

[19] DELPHI Collaboration, Nucl.Instr.Meth.**A303**(1991)233.

[20] OPAL Collaboration, Zeit.Phys.**C67**(1995)555

[21] L3 Collaboration, Phys.Lett.**B316**(1993)427

[22] G. K. Bhattacharyya and R. A. Johnson, *Statistical Concepts and Methods*, John Wiley & Sons, Inc., ISBN 0–471–03532–7 (1977)

[23] F. A. Berends, W. Hollik and R. Kleiss, Nucl.Phys.**B304**(1988),712

[24] J. E. Campagne and R. Zitoun, Zeit.Phys.**C43**(1989),469

[25] S. Jadach, B. F. L. Ward and Z. Was, *The Monte Carlo program KORALZ, version 3.8, for the lepton or quark pair production at LEP/SLC energies*, CERN-TH 5994/91, February 1991 Comp.Phys.Commun.**66**(1991),276.

[26] D. Bardin et al., *ZFITTER, An Analytical Program for Fermion Pair Production in e^+e^- Annihilation*, CERN-TH 6443/92, 1992

[27] DELPHI Collaboration, *DELSIM: DELPHI Event Generation and Detector Simulation*, Reference Manual, DELPHI 89–68 PROG 143, 1 September 1989, unpublished.

[28] DELPHI Collaboration, *DELPHI DATA ANALYSIS PROGRAM (DELANA) USERS GUIDE*, DELPHI 89–44 PROG 137, 17 May 1989, unpublished.

[29] D. Bertrand and L. Pape, *TANAGRA TRACK ANALYSIS AND GRAPHICS PACKAGE* , user's guide, DELPHI 87–95 PROG 98, 28 June 1988, unpublished.

[30] T. Spassoff, *DELPHI LongDST Content, Version 1.03, Description*, DELPHI 96–IT PROG IT, 28 April 1 1996, unpublished.

[31] S. Lowell, D. Brown and D. L. Nordstrom, *Review of Particle Properties*, Phys.Rev.**D50**(1994),1173

[32] *DELPHI public area files:* RUNQUALI.SUMARY91, RUNQUALI.SUMARY92, RUNQUALI.SUMAR93C, RUNQUALI.SUMARY94

[33] *DELPHI public area files:* LUMINOSITY_91.RES, SATLUM92.24JAN94, SATLUM-93.15JUN95, STILUM94.27JUN95

[34] Kari Marvik, *Search for lepton flavour violation in τ-decays using the Delphi detector.* Cand. Scient Thesis in Experimental Particle Physics, University of Bergen, April 21, 1994

[35] Øystein Krogen, *A SEARCH FOR LEPTON FLAVOUR VIOLATION IN Z^0 DECAYS WITH THE DELPHI DETECTOR AT LEP* Cand. Scient Thesis in Experimental Particle Physics, University of Oslo, April 27, 1995

[36] H. De Boeck and G. Wilkinson, *MUFLAG: A Framework for Muon Identification* DELPHI 93–14 PHYS 263, April 1993, unpublished

[37] A. G. Frodesen, O. Skjeggestad, and H. Tøfte, *Probability and Statistics in Particle Physics*, Universitetsforlaget, 1979, pp.390

[38] R. D. Cousins and V. L. Highland, Nucl.Instr.Meth.**A320**(1992)331